

# Metamaterials, Metasurfaces, and Artificial Dielectrics: Theory and Applications to the Next-Generation Telecommunication Platforms

Lead Guest Editor: Davide Ramaccia

Guest Editors: Ariel Epstein, Mirko Barbuto, and Scott Rudolph





---

**Metamaterials, Metasurfaces, and  
Artificial Dielectrics: Theory and  
Applications to the Next-Generation  
Telecommunication Platforms**



International Journal of Antennas and Propagation

---

**Metamaterials, Metasurfaces, and  
Artificial Dielectrics: Theory and  
Applications to the Next-Generation  
Telecommunication Platforms**

Lead Guest Editor: Davide Ramaccia

Guest Editors: Ariel Epstein, Mirko Barbuto, and Scott Rudolph



---

Copyright © 2017 Hindawi. All rights reserved.

This is a special issue published in "International Journal of Antennas and Propagation." All articles are open access articles distributed under the Creative Commons Attribution License, which permits unrestricted use, distribution, and reproduction in any medium, provided the original work is properly cited.

## Editorial Board

Ana Alejos, Spain  
Mohammad Ali, USA  
Jaume Anguera, Spain  
Rodolfo Araneo, Italy  
Alexei Ashikhmin, USA  
Herve Aubert, France  
Paolo Baccarelli, Italy  
Xiulong Bao, Ireland  
Toni Björninen, Finland  
Stefania Bonafoni, Italy  
Paolo Burghignoli, Italy  
Shah Nawaz Burokur, France  
Giuseppe Castaldi, Italy  
Luca Catarinucci, Italy  
Felipe Catedra, Spain  
Marta Cavagnaro, Italy  
Shih Yuan Chen, Taiwan  
Yu Jian Cheng, China  
Renato Cicchetti, Italy  
Riccardo Colella, Italy  
Laura Corchia, Italy  
Lorenzo Crocco, Italy  
Claudio Curcio, Italy  
Francesco D'Agostino, Italy  
María Elena de Cos Gómez, Spain  
Tayeb A. Denidni, Canada

Giuseppe Di Massa, Italy  
Michele D'Urso, Italy  
Francisco Falcone, Spain  
Miguel Ferrando Bataller, Spain  
Flaminio Ferrara, Italy  
Vincenzo Galdi, Italy  
Claudio Gennarelli, Italy  
Farid Ghanem, Algeria  
Sotirios K. Goudos, Greece  
Rocco Guerriero, Italy  
Kerim Guney, Turkey  
Song Guo, Japan  
Tamer S. Ibrahim, USA  
M. R. Kamarudin, UK  
Slawomir Koziel, Iceland  
Luis Landesa, Spain  
Ding-Bing Lin, Taiwan  
Angelo Liseno, Italy  
Pierfrancesco Lombardo, Italy  
Lorenzo Luini, Italy  
Atsushi Mase, Japan  
Diego Masotti, Italy  
Ch. F. Mecklenbräuker, Austria  
A. T. Mobashsher, Australia  
Ananda S. Mohan, Australia  
J.-M. Molina-Garcia-Pardo, Spain

Giuseppina Monti, Italy  
Giorgio Montisci, Italy  
N. Nasimuddin, Singapore  
Mourad Nedil, Canada  
Symeon Nikolaou, Cyprus  
Giacomo Oliveri, Italy  
Ikmo Park, Republic of Korea  
Josep Parrón, Spain  
Matteo Pastorino, Italy  
Xianming Qing, Singapore  
Ahmad Safaai-Jazi, USA  
Safieddin Safavi-Naeini, Canada  
Magdalena Salazar-Palma, Spain  
Stefano Selleri, Italy  
Raffaele Solimene, Italy  
Gino Sorbello, Italy  
Seong-Youp Suh, USA  
Sheng Sun, Hong Kong  
Larbi Talbi, Canada  
Luciano Tarricone, Italy  
Parveen Wahid, USA  
Wen-Qin Wang, China  
Shiwen Yang, China  
Yuan Yao, China



# Contents

---

**Metamaterials, Metasurfaces, and Artificial Dielectrics: Theory and Applications to the Next-Generation Telecommunication Platforms**

Davide Ramaccia, Ariel Epstein, Mirko Barbuto, and Scott Rudolph

Volume 2017, Article ID 4312542, 2 pages

**Beam-Steering Performance of Flat Luneburg Lens at 60 GHz for Future Wireless Communications**

Robert Foster, Deepak Nagarkoti, Ju Gao, Benjamin Vial, Felix Nicholls,

Chris Spooner, Sajad Haq, and Yang Hao

Volume 2017, Article ID 7932434, 8 pages

**Metamaterials for Microwave Radomes and the Concept of a Metaradome: Review of the Literature**

E. Öziş, A. V. Osipov, and T. F. Eibert

Volume 2017, Article ID 1356108, 13 pages

**Carbon Fiber Reinforced Polymer with Shredded Fibers: Quasi-Isotropic Material Properties and Antenna Performance**

Gerald Artner, Philipp K. Gentner, Johann Nicolics, and Christoph F. Mecklenbräuker

Volume 2017, Article ID 6152651, 11 pages

**Topological Design of Planar Circularly Polarized Directional Antenna with Low Profile Using Particle Swarm Optimization**

Xiaonan Zhao, Junping Geng, Ronghong Jin, Yao Jin, Xiang Liu, and Wenyan Yin

Volume 2017, Article ID 4983724, 12 pages

**A Review of Sensing Strategies for Microwave Sensors Based on Metamaterial-Inspired Resonators: Dielectric Characterization, Displacement, and Angular Velocity Measurements for Health Diagnosis, Telecommunication, and Space Applications**

Lijuan Su, Javier Mata-Contreras, Paris Vélez, and Ferran Martín

Volume 2017, Article ID 5619728, 13 pages

**A Broadband Left-Handed Metamaterial Microstrip Antenna with Double-Fractal Layers**

Roman Kubacki, Salim Lamari, Mirosław Czyżewski, and Dariusz Laskowski

Volume 2017, Article ID 6145865, 6 pages

**CRLH Transmission Lines for Telecommunications: Fast and Effective Modeling**

Juanjuan Gao and Guizhen Lu

Volume 2017, Article ID 1592783, 5 pages

## Editorial

# Metamaterials, Metasurfaces, and Artificial Dielectrics: Theory and Applications to the Next-Generation Telecommunication Platforms

**Davide Ramaccia,<sup>1</sup> Ariel Epstein,<sup>2</sup> Mirko Barbuto,<sup>3</sup> and Scott Rudolph<sup>4</sup>**

<sup>1</sup>*Roma Tre University, Rome, Italy*

<sup>2</sup>*Technion-Israel Institute of Technology, Haifa, Israel*

<sup>3</sup>*"Niccolò Cusano" University, Rome, Italy*

<sup>4</sup>*US Naval Research Laboratory, Washington, DC, USA*

Correspondence should be addressed to Davide Ramaccia; [davide.ramaccia@uniroma3.it](mailto:davide.ramaccia@uniroma3.it)

Received 10 August 2017; Accepted 10 August 2017; Published 11 September 2017

Copyright © 2017 Davide Ramaccia et al. This is an open access article distributed under the Creative Commons Attribution License, which permits unrestricted use, distribution, and reproduction in any medium, provided the original work is properly cited.

In recent years, wireless telecommunication providers have faced a significant expansion in the number of services demanded by their customers, which requires radiators with increasingly exceptional performance in terms of bandwidth, radiation patterns, space occupancy, and multifunctionality. Simultaneously, metamaterials, metasurfaces, and artificial dielectrics have revolutionized electromagnetism, improving the performance of existing devices and enabling a huge number of new applications.

This special issue is intended to reflect current research and development trends and novel approaches in the application of artificial material, metamaterial, and metasurface for next-generation of telecommunication platforms. A particular emphasis has been paid to components, devices, and systems to be employed in mobile communication towers, satellite payloads, aircraft, radars, and ship masts. Wide-band electrically small metamaterial-inspired antennas, multiple-input and multiple-output antenna systems, multiantenna platforms with invisibility cloaks exhibiting low mutual coupling and reduced blockage between elements, and highly directive low-profile metasurface-based antennas are just some of the novel marvels enabled by this technology.

We are particularly glad to serve as guest editors for this special issue, which contains a representative collection of the current trends and novel applications of artificial material, metamaterial, and metasurface in telecommunication field.

The paper by R. Foster et al. is focused on the beam-steering capabilities of a simplified flat Luneburg lens operating at 60 GHz. The lens is designed by using transformation electromagnetics approach and, then, fabricated by using ceramic composites. The beam-steering capabilities of the lens are experimentally verified, demonstrating that it can azimuthally scan a region within  $\pm 30^\circ$  with gains of at least 18 dBi over a bandwidth from 57 to 66 GHz. The lens has been used in a wireless link for the transmission of a raw high definition video.

The paper by E. Öziş et al. presents a review of the literature on microwave radomes for antenna systems made of metamaterials and introduces the concept of "metaradomes." The paper discusses the possibilities that metamaterials open up in the improvement and/or correction of characteristics (gain, directivity, and bandwidth) of the enclosed antenna, as well as the possibility of adding new features, such as band-pass frequency behaviour, polarization transformations, and the ability to be switched on/off. Examples of applications of metamaterials in the design of microwave radomes available in the literature as well as potential applications, advantages, drawbacks, and still-open problems are described.

The paper by G. Artner et al. presents a carbon-fibre reinforced polymer (CFRP) laminate to be used as ground plane material for both a narrowband wire monopole antenna at 5.9 GHz and an ultrawideband conical monopole antenna for

1–10 GHz. CFRP are already used for lightweight construction of reflectors, mostly in large parabolic dishes or space applications, but they typically present a high anisotropy due to the alignment of shredded fibres. In this paper, the authors design and experimentally verify the possibility of decreasing the material anisotropy by randomly orienting the fibres, which compose the ground plane for both wire and conical monopoles.

The paper by X. Zhao et al. introduces a topological method for the design and optimization of low-profile circularly polarized (CP) directional antenna. The authors propose to insert two layers of artificial materials, generated by particle swarm optimization, between an equiangular spiral antenna and the ground, in order to achieve both directional radiation pattern and high gain. The optimized and manufactured antenna exhibits good impedance matching in the band 4–12 GHz, with a whole-band stable directional pattern in 4–11.5 GHz and antenna gain of 8 dBi.

L. Su et al. present a review paper on the sensing approaches for the implementation of microwave sensors based on transmission lines loaded with metamaterial-inspired resonators. The authors focus the attention on four sensing strategies: (i) resonance frequency variation, (ii) coupling modulation through symmetry disruption (causing variation of the notch depth), (iii) frequency splitting (also exploiting symmetry properties), and (iv) amplitude modulation of a harmonic signal. These sensors are useful in various scenarios, such as characterization of dielectric materials for communication circuits, medical diagnosis and treatment with microwave technologies, and sensors for space applications.

The paper by R. Kubacki et al. presents a microstrip patch antenna based on the left-handed metamaterial concept. By using a planar periodic geometry derived from fractal shapes, the antenna exhibits improved characteristics in terms of bandwidth, gain, and radiation characteristics. The proposed design could support an ultrawide bandwidth ranging from 4.1 to 19.4 GHz, demonstrating enhanced gain with an average value of 6 dBi over the entire frequency range, a peak of 10.9 dBi, and a radiation capability directed in the horizontal plane of the antenna.

The paper by J. Gao et al. presents a different parameter extraction approach based on zero immittances for composite right/left-handed (CRLH) structures. For lossless unit cell equivalent circuit model, L-C parameters of series and parallel branches are extracted from the series and parallel resonance frequencies, respectively. This approach, which can be applied to symmetric and unbalanced CRLH structures, provides an effective and straightforward way to design CRLH metamaterials for applications in telecommunication systems.

## Acknowledgments

We would like to acknowledge the many people that have made the publication of this special issue possible. First of all, sincere thanks go to the authors for having submitted the exciting results of their research to this special issue. We

are also very grateful to the reviewers who dedicated their time and expertise to increase the scientific quality of the submissions. Finally, the guest editors would sincerely like to thank all the readers interested in the papers published on this special issue. We hope you may find here new exciting ideas for your research activities.

*Davide Ramaccia  
Ariel Epstein  
Mirko Barbuto  
Scott Rudolph*

## Research Article

# Beam-Steering Performance of Flat Luneburg Lens at 60 GHz for Future Wireless Communications

Robert Foster,<sup>1</sup> Deepak Nagarkoti,<sup>1</sup> Ju Gao,<sup>1</sup> Benjamin Vial,<sup>1</sup> Felix Nicholls,<sup>2</sup>  
Chris Spooner,<sup>2</sup> Sajad Haq,<sup>2</sup> and Yang Hao<sup>1</sup>

<sup>1</sup>School of Electronic Engineering and Computer Science, Queen Mary University of London, London E1 4NS, UK

<sup>2</sup>QinetiQ, Cody Technology Park, Ively Road, Farnborough GU14 0LX, UK

Correspondence should be addressed to Yang Hao; y.hao@qmul.ac.uk

Received 17 February 2017; Accepted 27 June 2017; Published 2 August 2017

Academic Editor: Davide Ramaccia

Copyright © 2017 Robert Foster et al. This is an open access article distributed under the Creative Commons Attribution License, which permits unrestricted use, distribution, and reproduction in any medium, provided the original work is properly cited.

The beam-steering capabilities of a simplified flat Luneburg lens are reported at 60 GHz. The design of the lens is first described, using transformation electromagnetics, before discussion of the fabrication of the lens using casting of ceramic composites. The simulated beam-steering performance is shown, demonstrating that the lens, with only six layers and a highest permittivity of 12, achieves scan angles of  $\pm 30^\circ$  with gains of at least 18 dBi over a bandwidth from 57 to 66 GHz. To verify the simulations and further demonstrate the broadband nature of the lens, raw high definition video was transmitted over a wireless link at scan angles up to  $36^\circ$ .

## 1. Background and Motivations

The quest for ubiquitous wireless connectivity with ever-increasing data rates has been a feature of the last half century. With the advent of the Internet of Things (IoT) adding huge numbers of devices requiring bandwidth to an already-challenging push for even greater data rates to be supported on personal wireless terminals, considerable research effort is being invested into future wireless networks. High-data rate applications include the streaming of ultrahigh definition video and virtual and augmented reality (e.g., [1, 2]); the use of 60 GHz for these applications is now relatively well-established, with IEEE standards (e.g., 802.15.3c, 802.11ad [3]) well-suited for this aspect of 5G services and networks. Other aspects of 5G development are concerned with serving greater numbers of end-terminals and reducing latency, with some applications in the IoT relevant to this (even when data rate requirements are not severe).

A large number of technologies are being brought together to achieve the various aims for the next generation of wireless networks [4]. This includes the use of *small cells* (where the density of base stations is increased), *cooperative communications* (where interference is reduced via communication between nodes, to improve achievable data rates

and reliability), *carrier aggregation* (where bandwidth from disparate channels is combined to meet requirements), and *heterogeneous networks* (where multiple networks operating at different frequencies and with different modulations, etc., are used). One key technology is massive multi-input-multi-output (M-MIMO) systems, where the number of antennas is increased by at least an order of magnitude (e.g., [5–7]).

One key approach to realise the objectives of future wireless networks is to utilise previously unused parts of the electromagnetic spectrum at higher frequency bands, particularly the millimetre-wave (mm-wave) and terahertz (THz) bands. Currently, wireless networks predominantly use the spectrum between 0.1 and 10 GHz, as these have offered key benefits of long propagation ranges, ease of fabrication, and ease of power generation and signal modulation, amongst others. Conversely, the higher bands must overcome increased propagation losses, smaller feature sizes that increase fabrication challenges, and other problems; the demand for bandwidth is such that these challenges are now being addressed. Furthermore, the shift to mm-wave also involves a change to directive communications, rather than broadcasting, which introduces new challenges [8, 9]. Within future wireless networks, mm-wave frequencies around 28 GHz and 37 GHz have been proposed for use in cellular

networks in urban environments (e.g., [10–13]), with the 25–40 GHz band being considered by the Federal Communications Commission in the US [14], whilst mm-wave frequencies between 55 and 100 GHz have been proposed for indoor environments and short-range outdoor environments, including vehicle-to-vehicle links, as well as other applications that may also rely on 5G networks (e.g., [13, 15–17]).

Transformation electromagnetics (TrE) is a rapidly maturing technique that offers increased control of electromagnetic waves via control of the spatial variation in material properties [18, 19]. The requirements on material properties can be challenging [20, 21], but the use of (quasi) conformal TrE can simplify the required materials, albeit with some sacrifice in performance usually a consequence (e.g., [22–24]). One area that has garnered much attention is the use of TrE to change the shape of a (quasi) optical device (lens or reflector), whilst maintaining the electromagnetic performance by changing the spatial variation of the permittivity (and permeability, in some cases); one example of the power of TrE in this regard is the Luneburg lens [25]. The Luneburg lens (LL) is a spherical lens with a continuously varying refractive index, such that it has a relative permittivity of 2 at the centre and 1 at the outer surface (since the relative permeability is unity at the frequencies of interest) [26]. In practical implementation, the continuous variation is approximated with discrete shells of differing permittivities. The key desirable feature of the LL is that a point source placed on the surface produces a collimated beam on the other side of the lens. Practically, however, the LL requires a relatively bulky lens and the ability to steer the beam by moving the source around a curved surface. It has been shown that approximations using only two shells can still achieve the beaming behaviour of the LL [27], at the cost of reduced operating bandwidth (as determined by parameters including the main lobe gain and side lobe levels).

In this paper, we report on the beam-steering capabilities of a flat Luneburg lens operating at 60 GHz, designed using TrE. In the next section, we discuss the design of this lens, based on the same procedure described in [28]. The beam-steering capabilities are then discussed via simulation results. We proceed by describing the fabrication of the lens in Section 3, before discussing the use of the lens in a real-world scenario, demonstrating the real-time transmission of uncompressed high definition video over a 60 GHz link at different beam positions and examining the trade-offs resulting from the lens performance (Section 4). The final section offers some final thoughts on the implementation of systems using TrE antennas, together with our plans for future work.

## 2. Design of the Flat Luneburg Lens

The fundamentals of TrE have been expounded in many places (e.g., [18, 19, 22, 23]); their application to the design of this 60 GHz flat Luneburg Lens (FLL) closely follows that described in earlier work by the authors and colleagues for the design of a similar FLL operating between 7 and 14 GHz [28]. As such, we offer an abbreviated description of the main points here.

The permittivity distribution of the spherical LL is given by

$$\epsilon_{\text{LL}} = 2 - \left(\frac{r}{R}\right)^2, \quad (1)$$

where  $r = \sqrt{x^2 + y^2 + z^2} \in [0, R]$  is the radial position within the sphere,  $R$  is the outer radius of the sphere, and  $x$ ,  $y$ , and  $z$  are the spatial coordinates. (We assume that the relative permeability is isotropic and equal to unity.) Due to the symmetry of the sphere, it is simpler to deal with a 2D cross-section and subsequently convert to a 3D device, such as by rotating about the third axis (e.g., use  $r = \sqrt{y^2 + z^2}$  when applying the transformation and rotate about the  $x$ -axis after the transformation has been applied).

In this case, we apply a 2D transformation parameterized by a real-valued compression factor  $\delta$  and given by

$$\begin{aligned} z' &= \frac{\delta}{\sqrt{R^2 - y^2}} z, \\ y' &= y. \end{aligned} \quad (2)$$

This results in an anisotropic permittivity profile that must be approximated in discrete layers (the resultant permeability profile is also anisotropic, though this is approximated as unity). It can be seen that the compression applied along  $z$  leads to an expansion along  $y$  (see [28] for more details). In material terms, this means the permittivity increases (with respect to the sphere) along the  $y$  direction but decreases along the  $z$  direction. In this case, the lens is approximated by an isotropic permittivity equal to the  $y$ -component of the permittivity, due to the symmetry of the lens. The discretization process requires, in general, consideration of both electromagnetic performance and fabrication capability. As with the lens of [28], a six-layer structure was used with permittivities ranging between 2 and 12, and the layer dimensions (radius  $R_i$  and thickness  $h_i$ ) optimised. Due to the transformation process and diffraction effects, the focal point is no longer expected to be at the lens surface, but some distance from it outside the lens [28].

A sketch of the six-layer lens is shown in Figure 1, with the corresponding dimensions and permittivities given in Table 1. Figures 2 and 3 show the simulated beam scanning at 0 mm and 20 mm feed offset, respectively, at 60 GHz. A reduction in gain of less than 3 dB can be seen.

## 3. Fabrication of Flat Luneburg Lens

The lens was manufactured in two halves, which were bonded together once all layers had been completed. Each half of the first composite layer was cast onto a solid polymer base, which was made in a cylindrical mould. The second composite layer was cast on top of the first layer once it had cured and been machined. This was repeated until all composite layers had been created. The original base was then machined off so that the two halves could be bonded together and then a final machining process was undertaken to achieve

TABLE 1: Design Parameters for six-layer Luneburg lens (lengths in millimetres).

Layer	Radius $R$	Thickness $h$	$\epsilon$
1	7.80	1.66	12
2	13.30	3.32	10
3	17.43	4.40	8
4	19.13	5.50	6
5	22.28	6.20	4
6	23.85	6.90	2

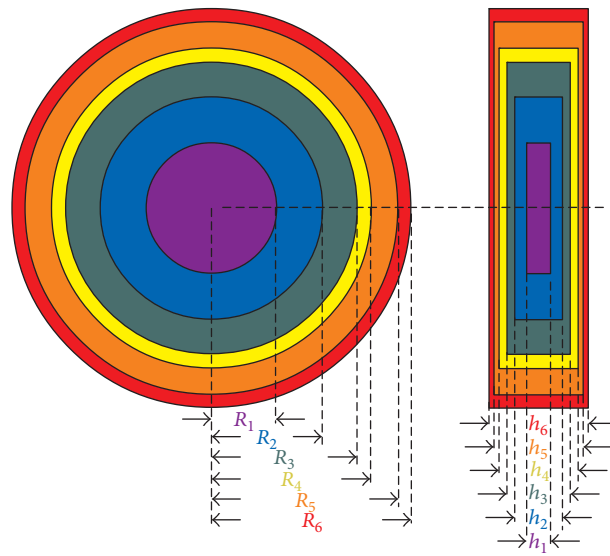


FIGURE 1: Transformed Luneburg lens structure showing the six layers.

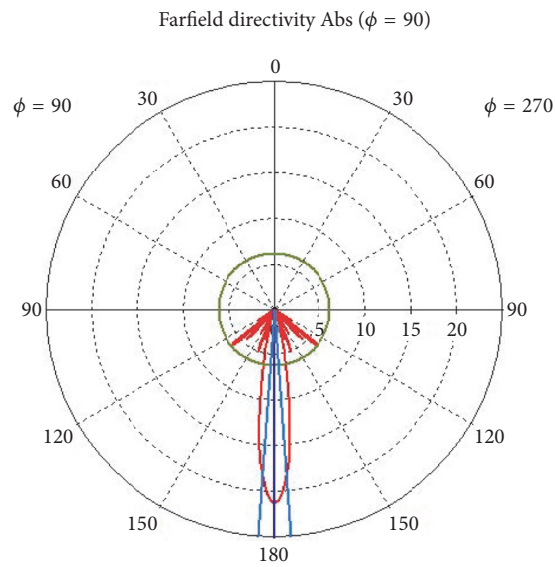


FIGURE 2: Simulated scanning behaviour of the six-layer lens at 60 GHz and no feed offset.

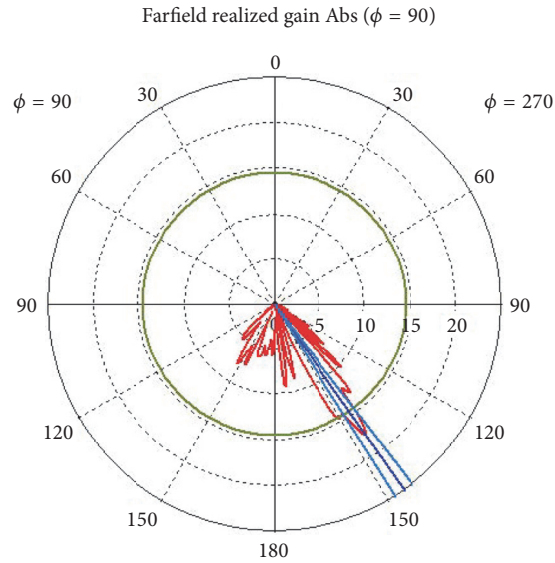
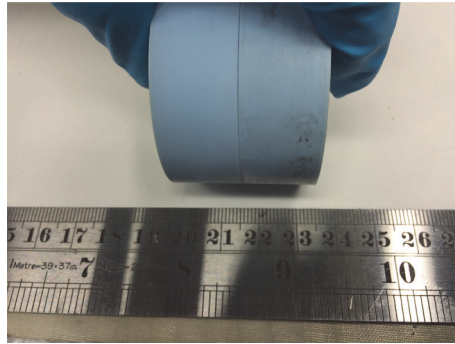
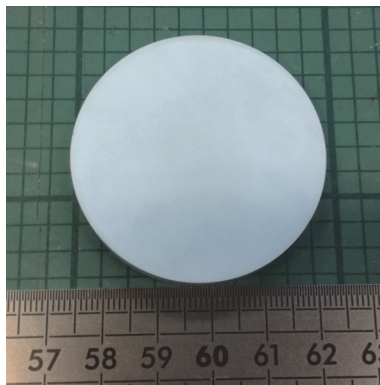


FIGURE 3: Simulated scanning behaviour of the six-layer lens at 60 GHz and 20 mm feed offset.



(a)



(b)



(c)

FIGURE 4: Lens fabrication at QinetiQ: (a) lens prior to final milling; (b) front view of lens after milling; (c) side view of lens after milling.

the final dimensions. Figure 4 shows photographs of the lens prior to and after machining of the final cylinder.

#### 4. System-Level Effects of Lens Performance

To place the beam-steering performance of the lens into context, and assess some system-level aspects, an experiment

was conducted, with the layout shown in Figure 5. This involved the wireless transmission of uncompressed high definition video over a direct path in the 60 GHz band. The experiment was based around the VubiQ<sup>®</sup> development system with additional baseband I/Q modules, available from Pasternack Enterprises, Inc. [29]. This kit includes video encoding and decoding boards and complete transmitter

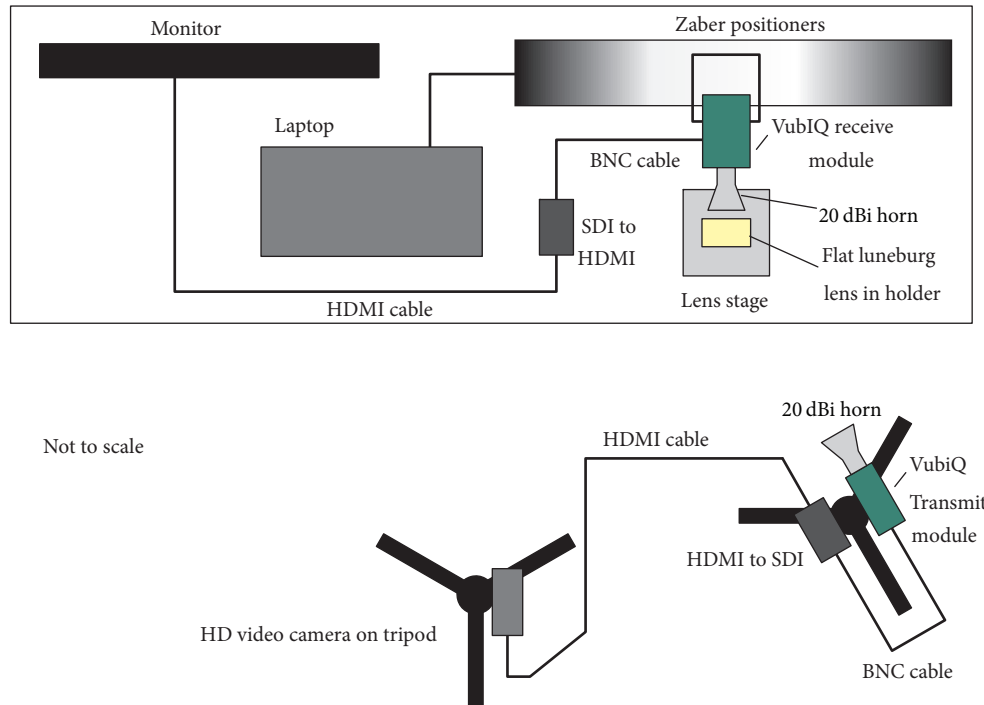


FIGURE 5: Sketch of the experimental arrangement for testing video transmission (plan view).

and receiver assemblies, with WR-15 radio frequency ports, covering 57–64.8 GHz with channel widths of 500 MHz and a modulation bandwidth of up to 1.8 GHz [29]. The output power of the transmitter was 12 dBm [30], whilst the noise figure for the receiver was 6 dB [31]. Two 20 dBi conical horns with WR-15 ports were used as the antennas [32]. The transmitter unit was mounted on a tripod, and the receiver unit was mounted on a Zaber dual-axis positioner system, with the lens positioned in front of the receive horn. In this set-up, the beam-steering was achieved by lateral movement on the  $x$ -axis. Figure 6 shows photographs of the video successfully transmitted at  $0^\circ$  and  $36^\circ$ , as well as no transmission at  $36^\circ$  when the lens is removed. The alignment of transmitter unit with the receiver was achieved manually. It is noted that the separation between transmitter and receiver was decreased (from 0.996 m to 0.427 m) when the beam angle increased from  $0^\circ$  to  $36^\circ$ , to maintain a successful connection. Video footage of these experiments is available.

## 5. Final Considerations and Future Work

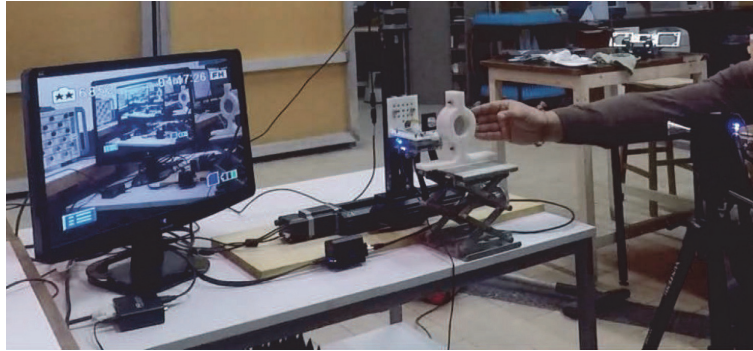
A thin ( $\approx 1.38\lambda$ ) flat Luneburg lens operating in the 60 GHz band has been described, with an emphasis on its beam-steering performance. Simple linear motion of the feed across the rear face of the lens has been shown to achieve beam-steering out to  $30^\circ$  and beyond, as seen via simulations and the transmission of high definition video over a 60 GHz link.

Horn antennas and multiple-axis motorized positioners are, of course, unsuitable for real-world applications in future wireless networks. Our continuing work in this area includes

the development of flat (PCB-based) integrated feeds, where the lens can be mounted directly on the reverse of the board. Flat feeds of various types, trading versatility, and cost are being developed, including switched-beam configurations, being lower in cost but less versatile, and small phased arrays, being cheaper than full phased arrays without a lens and potentially more versatile than the switched-beam feed. The continued development of chip antennas at 60 GHz (e.g., [33–42]) offers an alternative route to an integrated and compact feed. One advantage of a PCB-based feed is that the PCB substrate layer can be incorporated into the TrE lens design. Other advantages of the TrE lens approach include the ability to modify the lens geometry to meet any nonelectromagnetic constraint, simply by changing the material properties. This could include curving the outer face of the lens to be conformal to the container of the system, even using the permittivity of the container in the design, as with the feed PCB. Other lenses can be similarly modified via TrE, whilst the discretization process allows optimisation of the design to include other fabrication issues. The sequential casting approach utilised in this work is a well-established and relatively low-cost fabrication method that can readily accommodate different geometries. Furthermore, additive manufacturing techniques are continuing to mature and could offer an alternative route to fabrication, something that the authors will continue to investigate. Finally, we note that the TrE technique can be readily applied at other frequencies relevant to 5G and other future wireless communications technologies, making this work of wider relevance.



(a)



(b)



(c)

FIGURE 6: Photographs of the video transmission experiment: successful transmission with the lens at (a)  $0^\circ$  and (b)  $36^\circ$ ; (c) unsuccessful transmission without the lens at  $36^\circ$ .

### Conflicts of Interest

The authors declare that there are no conflicts of interest regarding the publication of this paper.

### Acknowledgments

This work was supported by the Engineering and Physical Sciences Research Council, UK (Grant no. EP/I034548/1). The assistance of Dr. Max Munoz, Antenna Laboratory Manager at QMUL, in the various experiments is noted and appreciated.

### References

- [1] A. P. G. Ariza, R. Muller, F. Wollenschlager et al., "60 GHz ultrawideband polarimetric MIMO sensing for wireless multi-gigabit and radar," *IEEE Transactions on Antennas and Propagation*, vol. 61, no. 4, pp. 1631–1641, 2013.
- [2] O. Abari, D. Bharadia, A. Duffield, and D. Katabi, "Cutting the cord in virtual reality," in *Proceedings of the 15th ACM Workshop on Hot Topics in Networks, HotNets 2016*, pp. 162–168, USA, November 2016.
- [3] "ISO/IEC/IEEE International Standard for Information technology–Telecommunications and information exchange between systems–Local and metropolitan area networks–Specific requirements–Part 11: Wireless LAN Medium Access Control (MAC) and Physical Layer (PHY) Specifications Amendment 3: Enhancements for Very High Throughput in the 60 GHz Band (adoption of IEEE Std 802.11ad-2012), ISO/IEC/IEEE 8802-11:2012/Amd.3:2014(E), pp. 1–634, 2014".
- [4] V. Jungnickel, K. Manolakis, W. Zirwas et al., "The role of small cells, coordinated multipoint, and massive MIMO in 5G," *IEEE Communications Magazine*, vol. 52, no. 5, pp. 44–51, 2014.

- [5] L. Lu, G. Y. Li, A. L. Swindlehurst, A. Ashikhmin, and R. Zhang, "An overview of massive MIMO: benefits and challenges," *IEEE Journal on Selected Topics in Signal Processing*, vol. 8, no. 5, pp. 742–758, 2014.
- [6] E. G. Larsson, O. Edfors, F. Tufvesson, and T. L. Marzetta, "Massive MIMO for next generation wireless systems," *IEEE Communications Magazine*, vol. 52, no. 2, pp. 186–195, 2014.
- [7] Y. Gao, R. Ma, Y. Wang, Q. Zhang, and C. Parini, "Stacked patch antenna with dual-polarization and low mutual coupling for massive MIMO," *IEEE Transactions on Antennas and Propagation*, vol. 64, no. 10, pp. 4544–4549, 2016.
- [8] S. Scott-Hayward and E. Garcia-Palacios, "Multimedia resource allocation in mmwave 5G networks," *IEEE Communications Magazine*, vol. 53, no. 1, pp. 240–247, 2015.
- [9] T. Nitsche, C. Cordeiro, A. B. Flores, E. W. Knightly, E. Perahia, and J. C. Widmer, "IEEE 802.11ad: Directional 60 GHz communication for multi-gigabit-per-second Wi-Fi," *IEEE Communications Magazine*, vol. 52, no. 12, pp. 132–141, 2014.
- [10] T. Rappaport, S. Sun, R. Mayzus et al., "Millimeter wave mobile communications for 5G cellular: it will work!," *IEEE Access*, vol. 1, pp. 335–349, 2013.
- [11] T. S. Rappaport, F. Gutierrez, E. Ben-Dor, J. N. Murdock, Y. Qiao, and J. I. Tamir, "Broadband millimeter-wave propagation measurements and models using adaptive-beam antennas for outdoor Urban cellular communications," *IEEE Transactions on Antennas and Propagation*, vol. 61, no. 4, pp. 1850–1859, 2013.
- [12] M. K. Samimi and T. S. Rappaport, "3-D Millimeter-Wave Statistical Channel Model for 5G Wireless System Design," *IEEE Transactions on Microwave Theory and Techniques*, vol. 64, no. 7, pp. 2207–2225, 2016.
- [13] A. I. Sulyman, A. Alwarafy, G. R. MacCartney, T. S. Rappaport, and A. Alsanie, "Directional radio propagation path loss models for millimeter-wave wireless networks in the 28-, 60-, and 73-GHz bands," *IEEE Transactions on Wireless Communications*, vol. 15, no. 10, pp. 6939–6947, 2016.
- [14] Notice of proposed rulemaking, Online, Federal Communications Commission, Oct. 23 2015, FCC-15-138 – including use of spectrum above 24 GHz for mobile radio services. Available: <https://www.fcc.gov/document/fcc-promotes-higher-frequency-spectrum-future-wireless-technology-0>.
- [15] J. Kim, S. Kwon, and G. Choi, "Performance of video streaming in infrastructure-to-vehicle telematic platforms with 60-GHz radiation and IEEE 802.11ad baseband," *IEEE Transactions on Vehicular Technology*, vol. 65, no. 12, pp. 10111–10115, 2016.
- [16] V. Va, J. Choi, and R. Heath, "The impact of beamwidth on temporal channel variation in vehicular channels and its implications," *IEEE Transactions on Vehicular Technology*, vol. 66, no. 6, pp. 5014–5029, 2016.
- [17] P. Kumari, N. González-Prelcic, and R. W. Heath, "Investigating the IEEE 802.11ad standard for millimeter wave automotive radar," in *Proceedings of the 82nd IEEE Vehicular Technology Conference, VTC Fall 2015*, USA, September 2015.
- [18] U. Leonhardt, "Optical conformal mapping," *American Association for the Advancement of Science. Science*, vol. 312, no. 5781, pp. 1777–1780, 2006.
- [19] J. B. Pendry, D. Schurig, and D. R. Smith, "Controlling electromagnetic fields," *American Association for the Advancement of Science. Science*, vol. 312, no. 5781, pp. 1780–1782, 2006.
- [20] R. Mittra and Y. Zhou, "A new look at transformation electromagnetics approach for designing electromagnetic devices such as flat lenses, reflectarrays and blankets for radar cross section reduction of real-world objects," *Philosophical Transactions of the Royal Society A: Mathematical, Physical and Engineering Sciences*, vol. 373, no. 2049, 2015.
- [21] P. S. Grant, F. Castles, Q. Lei et al., "Manufacture of electrical and magnetic graded and anisotropic materials for novel manipulations of microwaves," *Philosophical Transactions of the Royal Society A: Mathematical, Physical and Engineering Sciences*, vol. 373, no. 2049, Article ID 20140353, 2015.
- [22] O. Quevedo-Teruel, W. Tang, R. C. Mitchell-Thomas et al., "Transformation optics for antennas: why limit the bandwidth with metamaterials?" *Scientific Reports*, vol. 3, no. 1, article 1903, 2013.
- [23] M. Yin, X. Yong Tian, L. Ling Wu, and D. Chen Li, "All-dielectric three-dimensional broadband Eaton lens with large refractive index range," *Applied Physics Letters*, vol. 104, no. 9, Article ID 094101, 2014.
- [24] Z. H. Jiang, J. P. Turpin, K. Morgan, B. Lu, and D. H. Werner, "Spatial transformation-enabled electromagnetic devices: From radio frequencies to optical wavelengths," *Philosophical Transactions of the Royal Society A: Mathematical, Physical and Engineering Sciences*, vol. 373, no. 2049, Article ID 20140363, 2015.
- [25] R. K. Luneberg, *Mathematical Theory of Optics*, Brown University, Providence, RI, USA, 1944.
- [26] H. Schrank and J. Sanford, "A Luneberg-Lens Update," *IEEE Antennas and Propagation Magazine*, vol. 37, no. 1, pp. 76–79, 1995.
- [27] B. Fuchs, L. Le Coq, O. Lafond, S. Rondineau, and M. Himdi, "Design optimization of multishell Luneburg lenses," *IEEE Transactions on Antennas and Propagation*, vol. 55, no. 2, pp. 283–289, 2007.
- [28] C. Mateo-Segura, A. Dyke, H. Dyke, S. Haq, and Y. Hao, "Flat luneburg lens via transformation optics for directive antenna applications," *IEEE Transactions on Antennas and Propagation*, vol. 62, no. 4, pp. 1945–1953, 2014.
- [29] Pasternack Enterprises, Inc. Webpage for 60 GHz Development Kit. Last accessed 21 December 2016. Available: <https://www.pasternack.com/60-ghz-development-system-low-phase-noise-pem009-kit-p.aspx>.
- [30] Pasternack Enterprises, Inc. Webpage for 60 GHz Transmitter Module. Last accessed 21 December 2016. Available: <https://www.pasternack.com/60-ghz-transmitter-module-pem001-mim-p.aspx>.
- [31] Pasternack Enterprises, Inc. Webpage for 60 GHz Receiver Module. Last accessed 21 December 2016. Available: <https://www.pasternack.com/60-ghz-receiver-module-pem002-mim-p.aspx>.
- [32] Pasternack Enterprises, Inc. Webpage for 20 dBi Conical Horn with WR15 Input. Last accessed 21 December 2016. Available: <https://www.pasternack.com/horn-antenna-50-75-ghz-nominal-20-dbi-gain-wr-15-pe9881-20-p.aspx>.
- [33] A. Natarajan, S. K. Reynolds, M.-D. Tsai et al., "A fully-integrated 16-element phased-array receiver in SiGe BiCMOS for 60-GHz communications," *IEEE Journal of Solid-State Circuits*, vol. 46, no. 5, pp. 1059–1075, 2011.
- [34] S. Saadat, H. Mosallaei, and E. Afshari, "Radiation-efficient 60 GHz on-chip dipole antenna realised by reactive impedance metasurface," *IET Microwaves, Antennas and Propagation*, vol. 7, no. 2, pp. 98–104, 2013.
- [35] H.-H. Yeh, N. Hiramatsu, and K. L. Melde, "The design of broadband 60 GHz AMC antenna in multi-chip RF data

- transmission,” *IEEE Transactions on Antennas and Propagation*, vol. 61, no. 4, pp. 1623–1630, 2013.
- [36] M. Boers, B. Afshar, I. Vassiliou et al., “A 16TX/16RX 60 GHz 802.11ad chipset with single coaxial interface and polarization diversity,” *IEEE Journal of Solid-State Circuits*, vol. 49, no. 12, pp. 3031–3045, 2014.
- [37] M. Hanif, R. K. Pokharel, K. Yoshitomi, A. Barakat, and H. Elsadek, “A gain enhanced 60 GHz CMOS antenna-on-chip using off-chip  $\mu$  near zero metamaterial lens,” in *Proceedings of the 4th IEEE Asia-Pacific Conference on Antennas and Propagation, (APCAP '15)*, pp. 355–357, Kuta, Indonesia, July 2015.
- [38] M. Zamith, J. Magalh, P. Anacleto, and P. M. Mendes, “60 GHz on-chip antenna array with efficiency improvement using 3D microfabrication technology,” in *Proceedings of the 9th European Conference on Antennas and Propagation (EuCAP '15)*, pp. 1–4, May 2015.
- [39] M. O. Sallam, M. Serry, S. Sedky et al., “Micromachined on-chip dielectric resonator antenna operating at 60 GHz,” *Institute of Electrical and Electronics Engineers. Transactions on Antennas and Propagation*, vol. 63, no. 8, pp. 3410–3416, 2015.
- [40] H. Chu, Q. Lu, and Y.-X. Guo, “60-GHz broadband CMOS on-chip antenna with an artificial magnetic conductor,” in *Proceedings of the 2016 IEEE MTT-S International Microwave Workshop Series on Advanced Materials and Processes for RF and THz Applications, IMWS-AMP 2016*, Chengdu, China, July 2016.
- [41] H.-C. Wang, Y.-H. Chuang, W.-Y. Ruan, C.-C. Chou, and H.-R. Chuang, “60-GHz unbalanced-fed bandpass-filtering on-chip Yagi antenna in GIPD technology,” in *Proceedings of the 10th European Conference on Antennas and Propagation, EuCAP 2016*, Davos, Switzerland, April 2016.
- [42] A. S. A. El-Hameed, N. Mahmoud, A. Barakat, A. B. Abdel-Rahman, A. Allam, and R. K. Pokharel, “A 60-GHz on-chip tapered slot Vivaldi antenna with improved radiation characteristics,” in *Proceedings of the 10th European Conference on Antennas and Propagation, EuCAP 2016*, Davos, Switzerland, April 2016.

## Review Article

# Metamaterials for Microwave Radomes and the Concept of a Metaradome: Review of the Literature

E. Öziş,<sup>1</sup> A. V. Osipov,<sup>1</sup> and T. F. Eibert<sup>2</sup>

<sup>1</sup>German Aerospace Center (DLR), Microwaves and Radar Institute, Oberpfaffenhofen, Germany

<sup>2</sup>Chair of High-Frequency Engineering, Department of Electrical and Computer Engineering, Technical University of Munich, Munich, Germany

Correspondence should be addressed to E. Öziş; [ezgi.oezis@dlr.de](mailto:ezgi.oezis@dlr.de)

Received 20 January 2017; Revised 23 March 2017; Accepted 9 April 2017; Published 20 July 2017

Academic Editor: Scott Rudolph

Copyright © 2017 E. Öziş et al. This is an open access article distributed under the Creative Commons Attribution License, which permits unrestricted use, distribution, and reproduction in any medium, provided the original work is properly cited.

A radome is an integral part of almost every antenna system, protecting antennas and antenna electronics from hostile exterior conditions (humidity, heat, cold, etc.) and nearby personnel from rotating mechanical parts of antennas and streamlining antennas to reduce aerodynamic drag and to conceal antennas from public view. Metamaterials are artificial materials with a great potential for antenna design, and many studies explore applications of metamaterials to antennas but just a few to the design of radomes. This paper discusses the possibilities that metamaterials open up in the design of microwave radomes and introduces the concept of metaradomes. The use of metamaterials can improve or correct characteristics (gain, directivity, and bandwidth) of the enclosed antenna and add new features, like band-pass frequency behavior, polarization transformations, the ability to be switched on/off, and so forth. Examples of applications of metamaterials in the design of microwave radomes available in the literature as well as potential applications, advantages, drawbacks, and still open problems are described.

## 1. Introduction

Electromagnetic metamaterials are artificial compositions of resonant particles (metallic or dielectric) in a dielectric substrate, which are designed to control interaction of electromagnetic waves with the medium in a chosen wavelength region. The particles or inclusions are typically organized in a periodic array with the size of a unit-cell much smaller than the wavelength, so the incident wave interacts with the metamaterial as with an effectively homogeneous medium. Quasi two-dimensional metamaterial structures, involving just one layer of the unit-cells, are referred to as metasheets or metasurfaces. Metasheets are closely related to frequency selective surfaces (FSS), the difference being in the size of the unit-cells, which is comparable to the wavelength in FSS [1].

By properly choosing the shape and the size of the inclusions, the size of the unit-cells, and the substrate material, one can create metamaterials with effective electromagnetic parameters (permittivity, permeability, wave and surface impedance, etc.) that can be adjusted to almost any values,

including those not encountered in nature. Metamaterials have the advantage of being tunable and tailorable, with a wide range of realizable electromagnetic properties. Such materials can be used to build antenna radomes with improved transparency and even with new features such as the property of being tunable or switchable, thus resulting in a new class of devices: metamaterial radomes or “metaradomes” [2, 3].

“Metamaterial covers” [4] for small antennas, aiming at improvement of transmission and directivity of the covered antennas, can be seen as metaradomes as well. These covers can be polarization-dependent to change the polarization state of the antenna [5, 6]. Radomes involving FSS structures [1] are also linked to the concept of metaradome. Our focus in this paper is however on electrically large radomes in conjunction with metasheets [7, 8].

Metamaterials find applications not only in RF and microwave engineering but also in acoustics, nanotechnology, photonics, optics, and medical engineering. The literature about the design and applications of metamaterials is

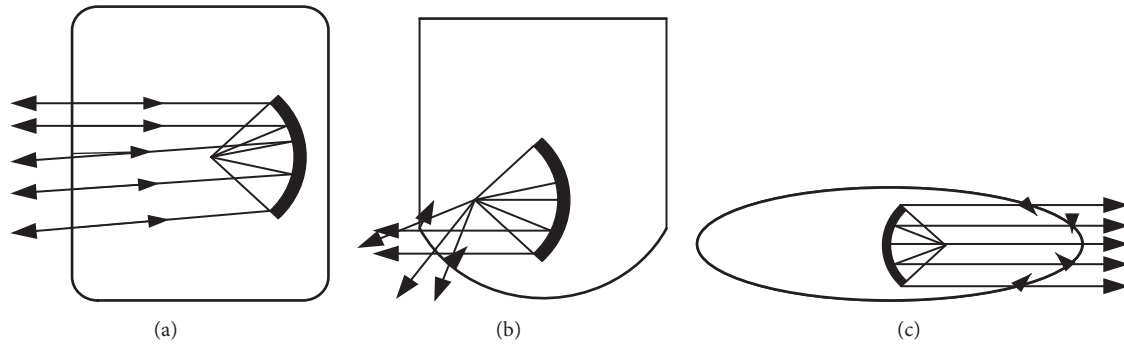


FIGURE 1: Different radome shapes: (a) cylindrical; (b) cylindrical-hemispherical; (c) spheroidal or ogival [16].

enormous, and we do not even attempt to review it. The reader is referred to the books [9–15]. The goal of this paper is rather to present a short overview of the basic features of metamaterials which can be relevant to applications in microwave radomes, give a collection of relevant references, and introduce the concept of the metaradome, a microwave radome with improved and extended functionality, made entirely from a metamaterial or involving a thin metamaterial sheet (metasheet).

The paper is organized as follows. Conventional microwave radomes are addressed in Section 2, basic features of electromagnetic metamaterials in Section 3, FSS in Section 4, metasheets in Section 5, tunable metamaterials in Section 6, and known examples of applications of metamaterials to microwave radomes in Section 7. The concept of the metaradome, advantages, and drawbacks of the use of metamaterials in radome applications are addressed in Section 8.

## 2. Microwave Radomes

The essential role of a radome is to form a protective cover between the antenna and the surroundings with minimal impact on the electrical performance of the antenna. An ideal radome should be fully transparent and lossless, that is, electrically invisible. Radomes should satisfy electrical, structural, and mechanical requirements. From the electromagnetic point of view, reflection, diffraction (at discontinuities in the radome, e.g., ribs), and absorption (in the radome material) should be accounted for when designing a radome [16–18].

The choice of the shape and material of the radome is typically determined by the application. Radomes are often curved structures made from ceramics and composites with high values of permittivity, which may result in a degraded performance of the antenna [19, 20]. Several differently shaped curved radomes are shown in Figure 1. In aerospace applications, the radome design must be compliant with aerodynamic requirements as well. The shape has a direct impact on the electrical characteristics of every radome.

The major parameters that characterize the radome performance are transmittance and boresight error. Transmittance is the ratio of the energy flows transported by the waves to and from the radome wall. It determines, for example, the operation range of a radar. Transmittance is a function

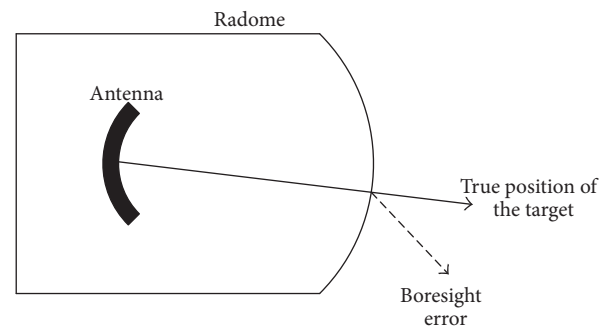


FIGURE 2: Boresight error in a radome: angular displacement from correct position [22].

of frequency, wall construction (thickness and material constants), incident angle, and polarization. The boresight error depends on more parameters: antenna position, the shape of the antenna aperture and the radome nose, frequency, polarization, and wall construction (sometimes with an integrated lens for phase compensation) [21]. The boresight error is caused by refraction of electromagnetic waves at the nonparallel interior and exterior sides of the radome wall with the result that a target is seen at an angularly changed, wrong position with respect to the antenna (Figure 2). This effect deforms the antenna beam [22].

Thus, radomes can negatively affect the antenna performance by distorting the amplitude and phase in the main beam, bringing more sidelobes, boresight errors, and a decreased bandwidth [17].

## 3. Metamaterials

There are various definitions of metamaterials in literature such as the following:

- (i) “Materials whose permeability and permittivity derive from their structure” [23, 24].
- (ii) “Structures composed of macroscopically scattering elements” [24, 25].
- (iii) “A new class of ordered nanocomposites that exhibit exceptional properties not readily observed in nature. These properties arise from qualitatively new

response functions that are not observed in the constituent materials and result from the inclusion of artificially fabricated, extrinsic, low dimensional inhomogeneities” [24, 26].

- (iv) “Macroscopic composites having a man-made, three-dimensional, periodic cellular architecture designed to produce an optimized combination, not available in nature, of two or more responses to a specific excitation. Each cell contains metamaterials. The metamaterial architecture is selected to strategically recombine local quasistatic responses or to combine or isolate specific nonlocal responses” [24, 27].
- (v) “Artificial periodic structures with lattice constants much smaller than the wavelength of the incident radiation” [28].

So, a metamaterial is usually a periodic array of resonators (inclusions), placed in a substrate, with the size of the unit-cells much smaller than the wavelength of the incident radiation. On the scale of the wavelength, the structure appears to be almost homogeneous with effective values of material constants: permittivity  $\epsilon$  and permeability  $\mu$ . By adjusting the parameters of the periodic structure (shape and size of the inclusions and period of the array) the effective material constants can be tailored to desired values, including those not encountered in natural materials. The use of resonant particles as the inclusions results in a frequency-dependent response (dispersion) of every metamaterial.

Most of natural materials have positive permittivity and permeability, and therefore they are referred to as “double-positive” (DPS) media. Since the wave vector  $\mathbf{k}$  and the power flow vector  $\mathbf{S}$ , given by the cross product of the electric field  $\mathbf{E}$  with the complex conjugate magnetic field  $\mathbf{H}$  ( $\mathbf{S} = (1/2)\mathbf{E} \times \mathbf{H}^*$ ), are always codirected, such media are also referred to as “right-handed” media [14, 15].

Some materials have either a negative permittivity or a negative permeability. This results in a purely imaginary value of the wavenumber  $k = \omega\sqrt{\epsilon\mu}$ , which implies strong attenuation of waves and makes such media unsuitable for the transmission of waves. When both  $\epsilon$  and  $\mu$  are negative, the wavenumber  $k$  is negative but real valued and propagation of waves is again possible. The vectors  $\mathbf{k}$  and  $\mathbf{E} \times \mathbf{H}^*$  are oppositely directed in this case, but  $\mathbf{E}$ ,  $\mathbf{H}$ , and  $\mathbf{S}$  still form a right-handed system. Such media, called “double-negative” (DNG) or “left-handed” media, do not exist in nature, but they can be created artificially [10, 14]. The diagram in Figure 3 illustrates this classification.

A great variety of resonators can be used as inclusions in designing metamaterials. Some of them, shown in Figures 4 and 5, are split-ring resonators (SRR), stepped impedance resonators (SIR), ring resonators, open complementary split-ring resonators (OCSRR), broadside coupled split-ring resonators (BC-SRR), nonbianisotropic split-ring resonators (NB-SRR), double slit split resonators (DSSRR), omega particles, and chiral particles [29–33]. Omega and chiral particles (Figure 5) couple electric and magnetic fields, which may result in bianisotropic metamaterials.

Depending on the choice of inclusions, one can create isotropic, anisotropic, chiral, and bianisotropic materials. The

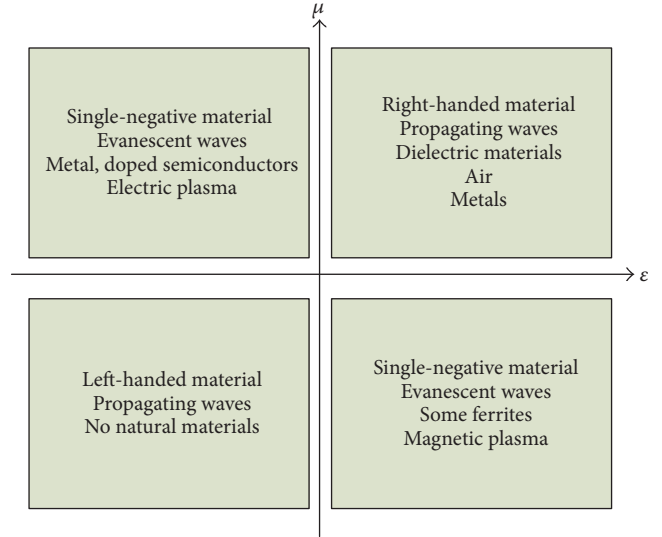


FIGURE 3: Classification of media according to permittivity and permeability [15, 94, 95].

effective permittivity and permeability may approach any desired values, for example, be negative or close to zero [13, 34, 35].

#### 4. Frequency Selective Surfaces

Radomes require thin layers rather than bulk materials. Efficient design concepts that rely on the surface effects rather than on volumetric effects have been first developed and realized for radio waves as frequency selective surfaces (FSS) [36].

FSS are built from many small patterned metal elements, which are of resonant size, that is, comparable to or slightly smaller than the wavelength [1]. Typical geometries of the elements are dipoles, Jerusalem crosses, and square and circular loops [37]. These elements are printed on a dielectric substrate and are similar to printed circuit boards (PCB). For changing the frequency characteristics, FSS can be mounted on a biased ferrite substrate or PIN diodes can be connected to the elements so that the structure can be made tunable or switchable [37]. Such FSS devices as transmitarrays [38] and reflectarrays [36] have become widely recognized tools in modern radio-antenna engineering. A consequence of the resonant size of the elements is however the presence of side lobes in the reflected and transmitted fields, which is a characteristic feature of FSS.

#### 5. Metasurfaces and Metasheets

Quasi two-dimensional metamaterials that consist of thin layers of inclusions with the thickness much smaller than the wavelength are called metasurfaces, metasheets, or metafilms, depending on whether the layer is penetrable or not. An example of a penetrable structure is shown in Figure 6. In contrast to FSS, the size of resonators and unit-cells in metasurfaces and metasheets is much smaller than the wavelength, which eliminates the grating lobes in the reflected and transmitted fields.

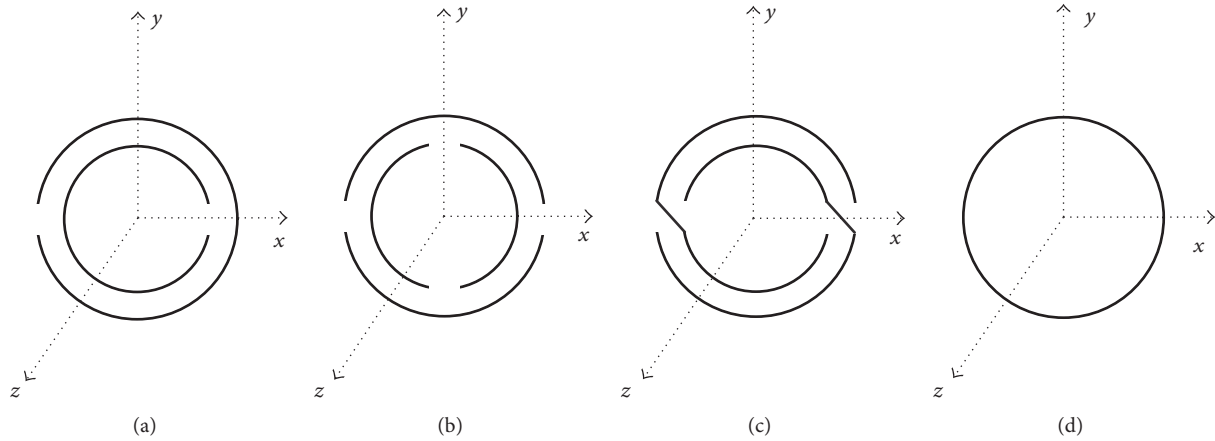


FIGURE 4: Examples of resonators used in the design of metamaterials: (a) conventional SRR; (b) double slit split-ring resonator (DS-SRR); (c) nonbianisotropic split-ring resonator (NB-SRR) [29]; (d) solid ring.

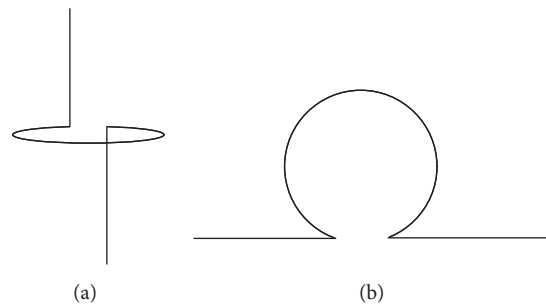


FIGURE 5: (a) Chiral particle; (b) omega particle [96].

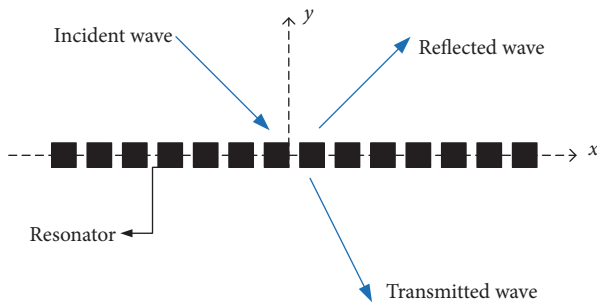


FIGURE 6: A metasheet (metafilm) consisting of arbitrarily shaped resonators periodically arranged in the  $x$ - $z$  plane [97].

At microwave frequencies, impenetrable metasurfaces are realized as a dense periodic texture of small elements printed on a grounded slab. A penetrable metasurface (called metasheet) involves a periodic planar distribution of small elements placed on a very thin host medium penetrable for electromagnetic waves [39–42].

Despite their small thickness, metasheets can fully control reflection, absorption, and transmission of electromagnetic waves (e.g., plane, surface or guided), including polarization, phase, and amplitude of the transmitted wave [35, 43–45]. As shown in literature, it is theoretically possible to design devices for almost arbitrary manipulations of plane waves,

which results in such devices as self-oscillating teleportation metasheets, transmitarrays, double current sheets, and metasheets formed by only lossless components [46].

The interaction between an incident field and the field scattered at an electrically small particle is described by electric and magnetic polarizabilities, which can be dyadics or tensors in the most general case. When particles are arranged in an array, the field illuminating a given particle consists of the incident wave and the field scattered at surrounding particles. This effect can be accounted for by effective polarizabilities that relate the incident field to the dipole moments induced on the particles in the array. Transmission and reflection coefficients are expressed in terms of the effective polarizabilities, and one can search for optimal arrays of optimal particles by imposing desirable requirements on the transmission and reflection coefficients, for example, by minimizing reflection and absorption and maximizing transmission of a given wave. To get more degrees of freedom, bianisotropic particles are needed, which is the most general type of particles, polarizable by both electric and magnetic fields and with magnetoelectric coupling [31, 47]. Chiral particles are a special case of bianisotropic particles, and bianisotropy is a combination of anisotropy with magnetoelectric coupling [48].

In the design of metasheets capable of influencing in a desired way the propagation of an incident wave, the Huygens principle can be applied [49]. According to the Huygens principle, each point on a wave front may behave

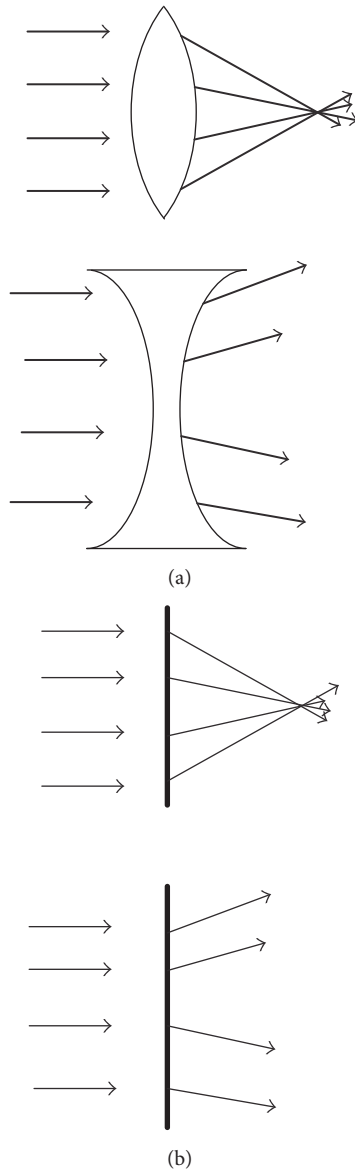


FIGURE 7: (a) Conventional optical lenses should be curved for focusing or defocusing the light; (b) planar Huygens' metasheets behave like a lens by locally controlling electric and magnetic currents induced on the surface [49, 51].

as a secondary source of spherical waves, and the sum of all secondary waves regulates the travel and the form of the wave [49, 50].

Conventional optical lenses can be replaced with planar metasheets as shown in Figure 7 [51]. Several metasheets combined together may work as a metamaterial with a negative index of refraction. Such structures can operate as a superlens providing images with the details finer than those allowed by the diffraction limit as shown in Figure 8 [52]. Realization of a superlens is however difficult as small deviations from ideal values of material parameters may significantly distort the image, for example, [53].

Transparent metasheets can be useful for the design of radomes since every radome must ensure high transmission

and low reflection and absorption within the operation frequency band of the enclosed antennas. A suitable radome wall can be created by using a bulk metamaterial or by adding a metasheet to the existing radome from a conventional material. Metamaterial particles are embedded in a host dielectric medium, and their shape and size are adjusted so as to achieve desired values of the radome parameters [7, 8].

## 6. Tunable Metamaterials

Reconfiguring the structural components of a metamaterial changes the effective (macroscopic) properties of the metamaterial. By doing so, it is possible to tailor metamaterials for a required purpose. This property is a remarkable attribute of metamaterials [34]. If the effective properties can be changed in real time, then the metamaterial is referred to as tunable [54].

Tunability can be achieved in a number of ways, including (i) electrical tuning of permittivity, (ii) electrical tuning of permeability, (iii) magnetic tuning of permittivity, and (iv) magnetic tuning of permeability, as well as simultaneous tuning of both permittivity and permeability [55, 56]. These changes can be achieved by adjusting the geometry of the unit-cell, for example, size, orientation, and position of resonators, or the material of the substrate. All these changes can be applied at the same time [54].

Another approach is the use of active lumped elements, such as non-Foster active elements [57], micro-electro-mechanical systems (MEMS) [58, 59], pin diodes [60, 61], varactors [62], or voltage-controlled capacitors [63]. For example, a voltage-controlled capacitance can affect the resonant frequency, so a varactor can be utilized for real-time tuning. A pin diode affects resistance. Using a non-Foster loading can influence the width of the frequency band. Liquid crystals can be inserted in unit-cells of metamaterials, and the refractive index of the substrate is tuned by applying a bias electric field which influences the orientation of liquid crystal molecules [64, 65]. FSS structures can also be combined with liquid crystals, and frequency shift can be realized with a bias voltage [66].

Still another approach is the use of small resonators with ferroelectric insertions (e.g., barium-strontium-titanate, lead-strontium-titanate, silver-tantalate-niobate, and barium-stannate-titanate) exploiting the temperature dependence of the permittivity of the material [67, 68].

Converting the radome wall into a tunable structure can bring great flexibility in controlling the properties of the covered antenna. For example, low-loss metasurfaces with reconfigurable reflection and partially reflective surfaces studied in [59, 69] can be used for this purpose.

## 7. Examples of Metaradomes

This section gives examples of metamaterial devices and components that can be used in the design of microwave radomes. The aim of every metaradome is to improve the electromagnetic response of the enclosed antenna and eliminate the negative effects of conventional microwave radomes (Section 2). Table 1 summarizes the characteristic features of the designs.

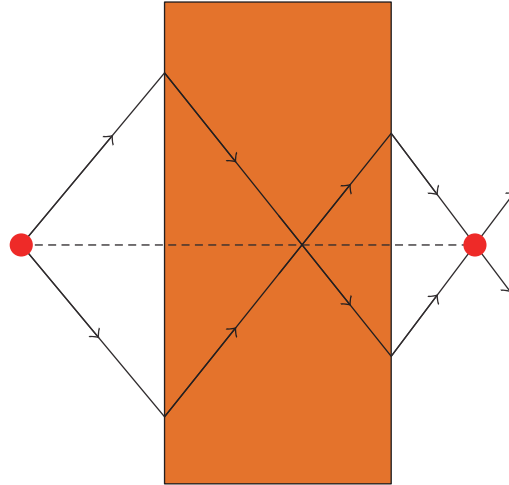


FIGURE 8: The operation of a superlens. Propagating and evanescent fields from the source go through a planar slab of negative-index material to form an image of the source. The image includes details finer than the wavelength, which cannot be realized by positive-index lenses [52].

TABLE 1: The list of the characteristic features of the metaradome designs described in Section 7.

Design	Characteristic features
(1)	PV cells as a metamaterial layer, dual band (lower band: 70 MHz bandwidth around 1185 MHz, upper band: 3400–3600 MHz), high gain (17.3 and 6.6 dBi at 3.5 and 1.23 GHz, resp.) [70]
(2)	Omega and reversed-omega elements in the unit cell, improved transmission between 13 and 17 GHz [72]
(3)	DPS and DNG media, gain increase to 6 dBi, beamwidth reduction by 37.5% [73]
(4)	Highly transparent at normal incidence, reduced reflection at oblique incidence, no phase change upon transmission [74]
(5)	Gain enhancement through 9 subwavelength holes by about 3.4 dB [75]
(6)	A 4-dB improvement in radiation pattern for blind spot angle, wide-angle impedance matching, blind spot mitigation [3]
(7)	DPS and DNG layers, gain increase by 3.45 dB, increase in the directivity by 2.9 dB, bandwidth improvement [78]
(8)	Refractive index smaller than unity, CP antenna, 3-dB improvement of the gain, increase of the bandwidth [79]
(9)	Heat-resistant structure, stable transmission at different incident angles, bandwidth increase from 10 GHz to 12 GHz by changing the size of unit cells [80]
(10)	Uniaxial medium with large permittivity along the anisotropy axis, operation on the near field, TM polarization transparent, broader radiation pattern, nearly eliminated interference within the cavity [81]
(11)	Polarization- and frequency-selective metasheets in X and Ka bands [82]
(12)	Disc-shaped electrically large metasheet, a hybrid approach (PO/FEM) to calculation of transmission [8]
(13)	Control of the phase of the transmitted wave by DC voltage, scanning over a wider range of radiation angle (up to 60° steering angle), 8 dBi maximum gain, beamwidth less than 7° [83]
(14)	Nonreciprocal ferrite structure, improved isolation, 21-dB difference between S12 and S21 at 8 GHz, transmission along one direction and attenuation along the opposite direction [85]

**7.1. Passive Metaradome Designs.** In the first 12 examples, passive metamaterials are used in the design of the radomes. They are passive in the sense that active lumped elements, which are described in Section 6, are not utilized. In the examples below, mainly the type of unit-cells and the number of layers are modified. The choice of the particles plays an important role in shaping the electromagnetic response of the structures. The particles are combinations of electrically

small metal wires and rings which interact with the incident wave as electric and magnetic resonant dipoles, respectively. Introducing gaps in the ring part of the particle (split-ring resonators and omega particles) results in a particle which combines the inductive and capacitive behavior, and this is a way of influencing the resonant frequency of the structure. The effective permittivity and permeability of the substrate are changed according to the shape of the particles. Thus,

by adjusting the geometry and size of the particles the resonance frequency can be controlled and the passband can be expanded.

The following examples are taken from the current, available studies of the use of metamaterials in the design of microwave radomes. In each example, a different electromagnetic parameter such as gain, transmission, resonance frequency, band width, and multiband feature is improved by tailoring the geometry, size, material, and position of the particles. Because of the ease of numerical simulations, planar radomes are mostly studied in the literature.

- (1) A panel of photovoltaic (PV) cells can be used as a metamaterial layer with a dual operation band [70]. The PV panel is used as a subwavelength selective periodic structure. In the first band, it behaves like a transparent sheet. In the second band, it behaves as a semitransparent sheet to ensure a high antenna gain. The structure is inspired by the concept of metamaterial Fabry-Pérot resonator [71].
  - (2) Differently positioned omega particles such as combinations of two or four omega and reversed-omega elements in the unit-cell can be used to design planar metamaterial radomes with an advanced performance. The omega-shaped particle is a bianisotropic particle. In this design, for eliminating this intrinsic bianisotropy, reverse-omega particles are combined with omega particles. The design described in [72] is characterized by good transmission between 13 and 17 GHz.
  - (3) Another design involving S-shaped particles is suggested in [73] to improve the antenna gain at a frequency around 5 GHz (Figure 9). Multilayered models, which include two materials with negative and positive refraction indices, are used.
  - (4) Combining a conventional dielectric material, which is always right-handed, with a left-handed metamaterial can increase the transmittance. The metamaterial helps to compensate the phase change as a wave propagates within the structure, implying reflection and transmission without the phase changes [74].
  - (5) For modifying the antenna pattern and improving the antenna gain, a subwavelength hole in the middle of a Jerusalem-cross structure as shown in Figure 10 can be used. The structure, called “a gain enhanced antenna radome,” concentrates electromagnetic fields and can change the antenna performance. The structure can play an important role in wireless communication [75].
  - (6) A metaradome can be designed to improve the response of a phased-array antenna at a blind condition. The blind direction of antenna arrays is the result of interaction between the Bloch array eigenmodes and the propagating surface waves or leaky waves [76]. The blind spot causes a failure of sending and receiving signals in that space angle region [76]. The scan blindness is also discussed in [77].
- A metaradome has been designed as a wide-angle impedance matching slab in [3] to alleviate this problem.
- (7) In [78], a radome with an operation frequency around 2 GHz is designed with different layers of positive refractive index materials and an SRR-based negative permeability metamaterial. By adjusting the electrical and geometrical parameters, the gain, the bandwidth, and the directivity can be improved.
  - (8) Many communication systems operate in the circular polarization mode. The advantage of circular polarization (CP) is that it eliminates the need to continuously align the two slits of the apertures; otherwise, the power of the system has to be increased. Cross-S-shaped inclusions can be used for CP antennas. For example, a design described in [79] involves the cross-S-shaped inclusions printed on an FR4 substrate with the size of the unit-cell 18 mm × 18 mm to create a metamaterial structure with an effective index of refraction, which is positive but smaller than unity and close to zero between 3.3 GHz and 3.7 GHz. According to the Snell law, rays leave such a slab almost normally to its surface. As a result, antenna gain and bandwidth have been improved.
  - (9) A structure suitable for high temperatures is described in [80]. It consists of an Ag (silver) microstructure pressed between two layers of quartz glass. The transmission can be controlled by changing the geometry of the Ag grid and the size of the unit-cells.
  - (10) A layer of a uniaxial medium with very large permittivity along the anisotropy axis can be used to transmit both propagating and evanescent spatial harmonics of the source onto the outer interface of an antenna to eliminate the effects of diffraction. Such a medium can be realized as a block of metal wire media embedded in a dielectric material and used as a radome [81].
  - (11) A simple prototype of a polarization- and frequency-selective metaradome is described in [82]. The structure consists of a periodic array of copper strips printed on top of a 2 mm thick layer of the FR4 epoxy (Figure 11). The structure blocks the transmission of fields polarized along the strips in a particular frequency range. By changing the dimension of the strips and the size of the unit-cells the operation frequency range can be changed. Two designs have been manufactured and measured, one for the X band (Figure 12) and another for the Ka band (Figure 13). For the X-band structure, the length of wire is 8.21 mm, the width of strip is 2 mm, and the unit-cell size is 14 mm. For Ka band, the dimensions of strips and unit-cells are smaller by the factor 3.48. The slight disagreement between the simulation and measurement is due to the fact that simulations assume an infinite planar periodic structure, whereas the manufactured plates are finite.

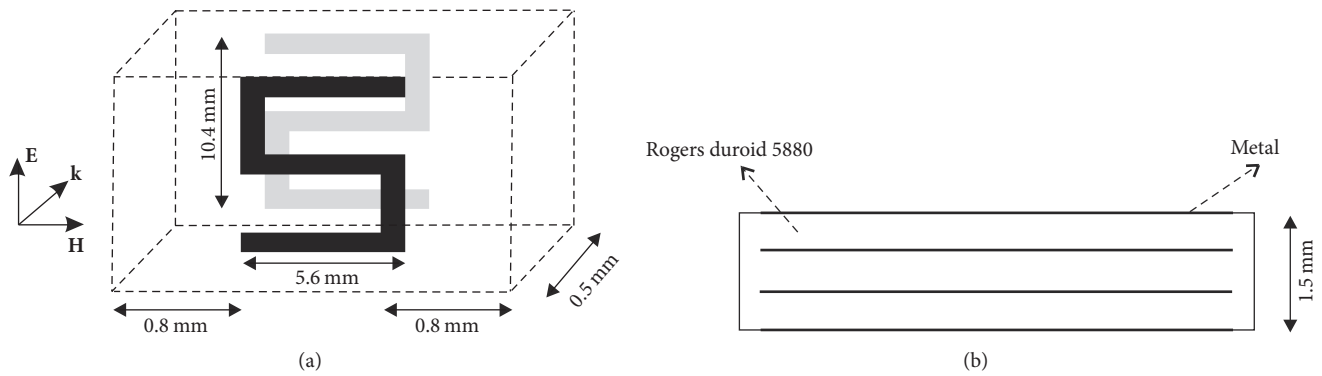


FIGURE 9: (a) Unit-cell structure; (b) structure for simulation [73].

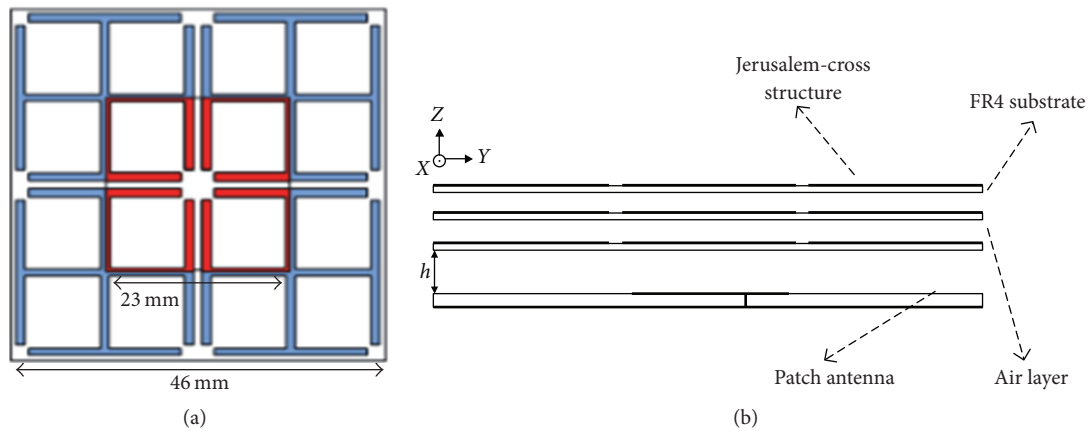


FIGURE 10: (a) Jerusalem-cross structure; (b) configuration of metamaterial radome and antenna [75].

(12) Calculation of transmission through metasheets of finite size is difficult because the assumption of periodicity of the structure is not applicable. Full-wave numerical simulations of such structures are limited to structures of several wavelengths in size. A hybrid approach combining Physical Optics (PO) approximation with transmission coefficients obtained from full-wave calculation for an infinite planar periodic structure is proposed in [8]. The unit-cells should be sufficiently small to justify the use of homogenized transmission coefficients. To estimate the accuracy of the hybrid approach, a circular metasheet consisting of copper rings on the FR4 substrate (Figure 14) was used as a test configuration. The diameter of the disc (160 mm) and the wavelength (30 mm) are such that the full-wave simulation is still possible and the structure is sufficiently large in order the PO method to apply. There is a good match of full-wave simulation and PO calculation (Figure 15).

### 7.2. Metaradome Designs Involving Active/Lumped Elements.

In the next two examples, active metamaterials are used in the design of the radome surface. Active metamaterials mean that active lumped elements or ferrite insertions (Section 6) are included in the designs to control the electromagnetic

response. An active element, varactor, is used in example (13). The ferrite is used in example (14). The use of ferrite insertions may lead to a nonreciprocal radome. Both examples show metaradomes that can be externally controlled.

(13) A metasheet with tunable refractive index can be realized by using varactors in the resonant cells of the metamaterial (Figure 16). The varactor with applied DC voltage behaves as an adjustable capacitor, which can be used to control the effective refractive index by changing the resonance frequency. Such a radome can control the phase of the transmitted wave by applying different DC voltages to different zones of the metamaterial slab since the phase shift depends on the bias voltage [83].

(14) Transmission can be permitted in one direction and suppressed in the opposite direction by a nonreciprocal metasheet. This feature comes from Faraday rotation, when electromagnetic waves propagate parallel to the applied bias field or in the direction of remanence magnetization in self-biased magnetic materials. Ferrites have low eddy current losses, which make them suitable for the use in some electronic applications such as power generation, conditioning, and conversion. Ferrites are particularly useful for

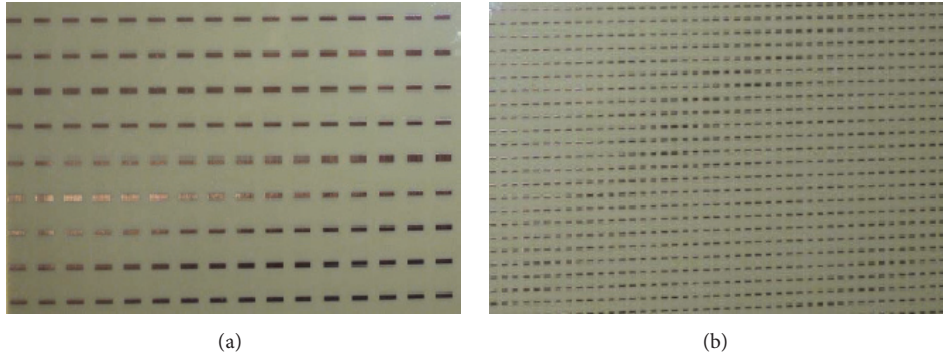


FIGURE 11: The X-band (a) and Ka-band (b) structures consisting of differently sized copper straight wires (strips) printed on top of the FR4 substrate.

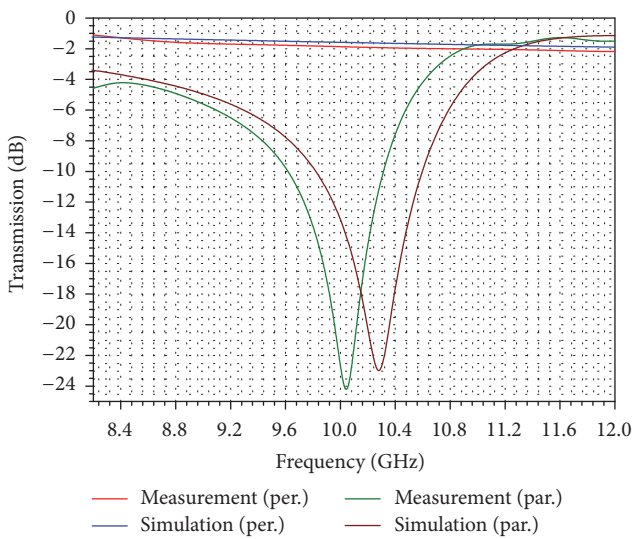


FIGURE 12: Measured and simulated (HFSS) transmission through the X-band structure.

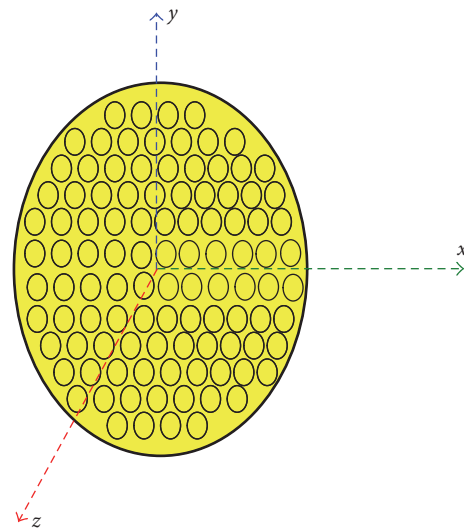


FIGURE 14: The circular electrically large metasheet in the  $x$ - $y$  plane. Copper rings are placed on the FR4 substrate [8].

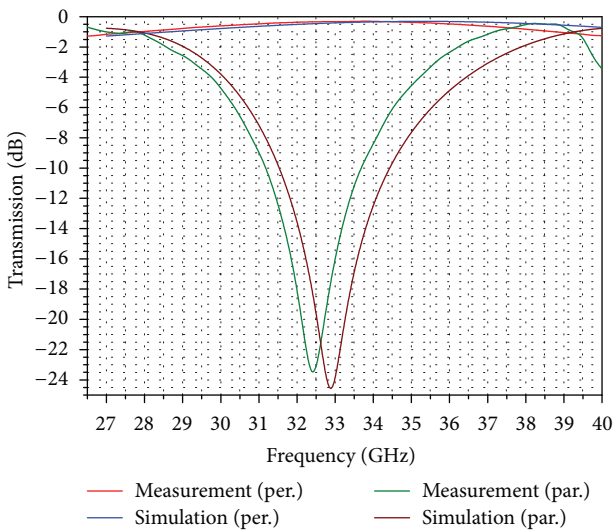


FIGURE 13: Measured and simulated (HFSS) transmission through the Ka-band structure.

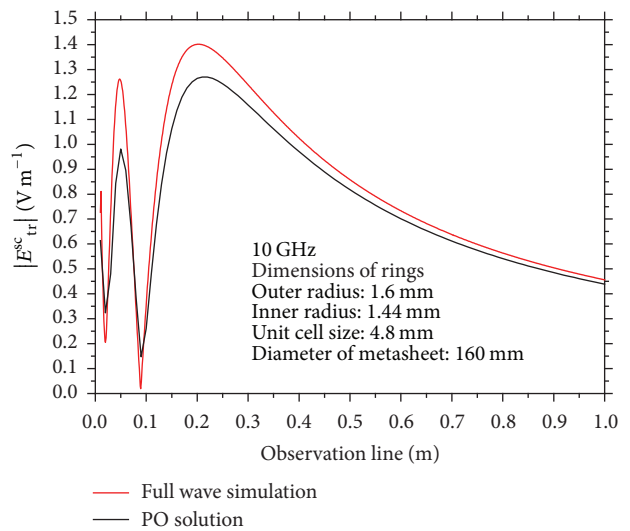


FIGURE 15: Scattered electric field along the observation line (along  $z$ -axis) in the shadow region behind the metasheet [8].

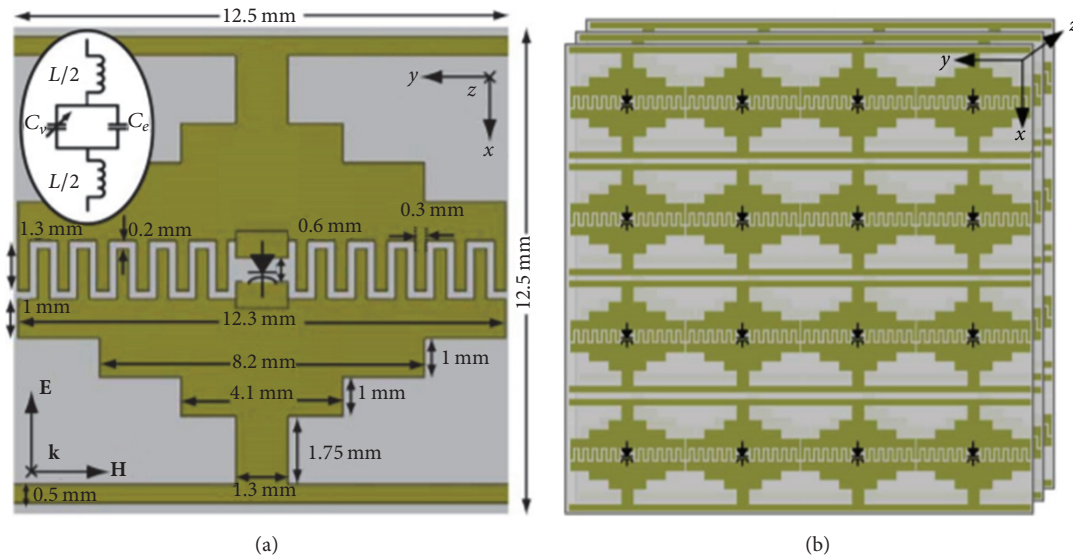


FIGURE 16: (a) Unit-cell of the realized metamaterial and its equivalent circuit; (b) metamaterial structure as a combination of unit-cells. The operating frequency is 4.7 GHz [83].

microwave devices that need strong coupling to electromagnetic signals and nonreciprocal behavior [84]. In the design described in [85], highly conductive strip gratings are adjusted on each side of a ferrite layer. The strips behave as microwave polarizer. The direction of the polarization rotation depends on the direction of the applied bias field.

## 8. Metaradomes: Pros and Cons, Potential Applications

Metamaterials and particularly their quasi two-dimensional versions, metasheets, promise many important applications in conjunction with microwave radomes. A metasheet with tailored transmission, absorption, and reflection properties can be mounted on the wall of a radome to bring additional features and benefits such as correction of phase distortions, reduction of transmission losses, shaping the frequency dependence of the transmission, and making the radome tunable, including the ability of being switched on/off. Implementation of the concept may result in multiband radomes with reconfigurable frequency pass bands, on/off modes, enhanced out-of-band rejection and eventually in an enhanced antenna gain.

The problems to be solved are as follows:

- (i) Most of the available realizations of metaradomes are planar, partly because of the relative ease of simulation (as infinite periodic structures) and partly due to the ease of manufacturing. Simulation of bounded and/or curved metamaterial structures is a difficult calculation problem because of the need to sample extremely fine subwavelength inclusions distributed over an electrically large area without the periodicity assumption. Simulation of curved metasurfaces is an open problem and a future research field. A possible approach is addressed in [8].

- (ii) The limited bandwidth, which is due to the resonance behavior of the individual inclusions, is an inherent feature of metamaterials. A number of recent studies are devoted to the extension of the bandwidth of metamaterial absorbers but little is known about extending the bandwidth of transparent structures. It should be noted however that a narrow bandwidth is not necessarily a negative situation because narrow-band systems are as necessary as wide-band systems in communication networks. For example, narrow-band systems help to have the cost-effective wireless networking for large outdoor environments such as seaports and rail yards, where simple data transactions are required [86].

Metaradome designs should be developed and adjusted to different application areas such as maritime, telecom, radar, aerospace, and automotive applications [87]. Metaradomes may help in shaping the directivity of antennas. Directional antennas are used in wireless networks [88], and the use of metamaterials in the antenna design is described in [88, 89]. Another application is cognitive radio. Such a radio automatically detects available channels in a frequency spectrum and accordingly changes its transmission or reception parameters to have an optimum communication bandwidth within a defined spectral region. Such a software-defined radio platform should convert into a completely reconfigurable wireless system that automatically alters its communication variables according to network and demand of user [90]. For this propose, there are studies to design suitable reconfigurable antennas [91–93].

## 9. Conclusion

The potential of metamaterials for improving the performance of microwave radomes has been outlined, and the concept of a metaradome has been presented. Several examples of

the use of metamaterials in the design of radomes have been given. The examples discussed here are by no means the only examples possible.

The application of metamaterials to microwave radomes is a new research field which is open for further analysis and development. Potential applications are diverse and promising. Much more work is still needed in the understanding, analysis, design, and fabrication of both metamaterials and metasheets for radomes.

## Conflicts of Interest

The authors declare that there are no conflicts of interest regarding the publication of this paper.

## References

- [1] A. B. Munk, *Frequency Selective Surfaces: Theory and Design*, Wiley, 2000.
- [2] E. Öziş, A. V. Osipov, and T. Eibert, "Analyzing scattering and reflection from metasheets of bi-anisotropic particles," *14th Onera-DLR Aerospace Symposium, ODAS*, June 2014.
- [3] P. Rodriguez-Ulibarri, M. Beruete, F. Falcone et al., "Metaradome for blind spot mitigation in phased-array antennas," in *Proceedings of the 8th European Conference on Antennas and Propagation, EuCAP 2014*, pp. 2504–2508, Netherlands, April 2014.
- [4] A. Alù, F. Bilotti, N. Engheta, and L. Vegni, "Metamaterial covers over a small aperture," *IEEE Transactions on Antennas and Propagation*, vol. 54, no. 6, pp. 1632–1643, 2006.
- [5] M. Veysi, A. Jafargholi, and M. Kamyab, "Theory and applications of metamaterial covers," in *Trends in Electromagnetism - From Fundamentals to Applications*, pp. 277–291, InTech, 2012.
- [6] J. Hu, C.-S. Yan, and Q.-C. Lin, "A new patch antenna with metamaterial cover," *Journal of Zhejiang University: Science A*, vol. 7, no. 1, pp. 89–94, 2006.
- [7] E. Öziş, A. V. Osipov, and T. F. Eibert, "Metamaterials for microwave radomes: an overview," *Progress In Electromagnetics Research Symposium, PIERS 2015*, July 2015.
- [8] E. Öziş, A. V. Osipov, and T. F. Eibert, "Physical Optics and full-wave simulations of transmission of electromagnetic fields through electrically large planar meta-sheets," *URSI-Landesausschuss in der Bundesrepublik Deutschland e.V., Kleinheubacher Tagung*, September 2016.
- [9] N. Engheta and R. W. Ziolkowski, Eds., *Metamaterials: Physics and Engineering Explorations*, Wiley, 2006.
- [10] G. V. Eleftheriades and K. G. Balmain, Eds., *Negative-Refractive Metamaterials: Fundamental Principles and Applications*, Wiley, 2005.
- [11] C. Caloz and T. Itoh, *Electromagnetic Metamaterials: Transmission Line Theory and Microwave Applications*, Wiley, 2005.
- [12] L. Solymar and E. Shamonina, *Waves in Metamaterials*, Oxford University Press, 2009.
- [13] F. Capolino, Ed., *Theory and Phenomena of Metamaterials*, CRC Press, 2009.
- [14] R. Marqués, F. Martín, and M. Sorolla, *Metamaterials with Negative Parameters: Theory, Design, and Microwave Applications*, Wiley, 2008.
- [15] T. J. Cui, D. R. Smith, and R. Liu, Eds., *Metamaterials: Theory, Design, and Applications*, Springer, 2010.
- [16] W. M. Cady, M. B. Karelitz, and L. A. Turner, *Radar Scanners and Radomes*, McGraw-Hill Book Company, 1948.
- [17] A. W. Rudge, K. Milne, A. D. Olver, and P. Knight, Eds., *The Handbook of Antenna Design*, IET, 1983.
- [18] J. D. Walton, Ed., *Radome Engineering Handbook, Design and Principles*, Dekker, 1970.
- [19] C. A. Balanis, Ed., *Modern Antenna Handbook*, Wiley, 2008.
- [20] D. J. Kozakoff, *Analysis of Radome-Enclosed Antennas*, Artech House, 2010.
- [21] D. F. Groutage and D. E. Smith, "Multi-layered tangent power series radome with integrated lens," in *Proceedings of 14th Symposium on Electromagnetic Windows*, pp. 7–11, USA, June 1978.
- [22] F. R. Youngren and M. Bedford, "Tapered radomes," April 11, 1967, US patent 3,314,070.
- [23] J. Pendry, "Negative  $\mu$ , negative  $\epsilon$ , negative refractive index, and how to exploit them," in *Euroconference on Electromagnetic Confinement - from Basic Research to the Marketplace: Electromagnetic Crystal Structure*, Scotland, June 2001.
- [24] A. Sihvola, "Electromagnetic emergence in metamaterials, deconstruction of terminology of complex media," *Advances in Electromagnetics of Complex Media and Metamaterials, NATO Science Series*, vol. 89, pp. 3–17, 2002.
- [25] T. Weiland, R. Schuhmann, R. B. Gregor et al., "Ab initio numerical simulation of left-handed metamaterials: comparison of calculations and experiments," *Journal of Applied Physics*, vol. 90, no. 10, pp. 5419–5424, 2001.
- [26] Metamaterials home page of the future projects of the defense advanced research projects agency (DARPA), Defence Sciences Office (DSO), <https://www.darpa.mil/>.
- [27] R. M. Walser, "Electromagnetic metamaterials," in *Proceedings of the SPIE Complex Mediums II: Beyond Linear Isotropic Dielectrics*, vol. 4467, pp. 1–15, 2001.
- [28] S. J. Pendry, "Metamaterials and the control of electromagnetic fields," in *Conference on Coherence and Quantum Optics, OSA Technical Digest*, pp. 1–11, 2007.
- [29] M. Durán-Sindreu, J. Naqui, F. Paredes, J. Bonache, and F. Martín, "Electrically small resonators for planar metamaterial microwave circuit and antenna design: a comparative analysis," *Applied Sciences*, vol. 2, no. 2, pp. 375–395, 2012.
- [30] L. M. Pulido-Mancera, J. D. Baena, and J. L. Araque Quijano, "Thickness effects on the resonance of metasurfaces made of SRRs and C-SRRs," in *Proceedings of IEEE Antennas and Propagation Society International Symposium, AP-S/URSI 2013*, pp. 314–315, USA, July 2013.
- [31] Y. Rađi and S. A. Tretyakov, "Balanced and optimal bianisotropic particles: maximizing power extracted from electromagnetic continuous fields," *New Journal of Physics*, vol. 15, pp. 1–15, June 2013.
- [32] C. R. Simovski, P. A. Belov, and M. S. Kondratjev, "Electromagnetic interaction of chiral particles in three-dimensional arrays," *Journal of Electromagnetic Waves and Applications*, vol. 13, no. 2, pp. 189–204, 1999.
- [33] J. Bonache, M. Gil, I. Gil, J. Garcia-Garcia, and F. Martín, "On the electrical characteristics of complementary metamaterial resonators," *IEEE Microwave and Wireless Components Letters*, vol. 16, no. 10, pp. 543–545, October 2006.
- [34] A. Sihvola, "Metamaterials in electromagnetics," *Metamaterials*, vol. 1, pp. 2–11, February 2007.
- [35] A. Priyanka, "A Review paper on metamaterial," *International Journal of Engineering Sciences and Research Technology*, vol. 3, no. 12, pp. 612–618, 2014.

- [36] D. M. Pozar, S. D. Targonski, and H. D. Syrigos, "Design of millimeter wave microstrip reflectarrays," *IEEE Transactions on Antennas and Propagation*, vol. 45, no. 2, pp. 287–296, 1997.
- [37] T. K. Chang, R. J. Langley, and E. A. Parker, "Active frequency-selective surfaces," *IEE Proceedings - Microwaves Antennas and Propagation*, vol. 143, no. 1, pp. 62–66, March 1996.
- [38] D. M. Pozar, "Flat lens antenna concept using aperture coupled microstrip patches," *Electronics Letters*, vol. 32, no. 23, pp. 2109–2111, 1996.
- [39] E. Martini and S. Maci, "Metasurface Transformation Theory," in *Transformation Electromagnetics and Metamaterials: Fundamental Principles and Applications*, D. H. Werner and D.-H. Kwon, Eds., Springer, 2014.
- [40] S. Maci, G. Minatti, M. Casaletti, and M. Bosiljevac, "Metasurfing: Addressing waves on impenetrable metasurfaces," *IEEE Antennas and Wireless Propagation Letters*, vol. 10, pp. 1499–1502, 2011.
- [41] Z. Wei, Y. Cao, X. Su, Z. Gong, Y. Long, and H. Li, "Highly efficient beam steering with a transparent metasurface," *Optics Express*, vol. 21, no. 9, pp. 10739–10745, 2013.
- [42] S. H. Mousavi, A. B. Khanikaev, J. Allen, M. Allen, and G. Shvets, "Gyromagnetically induced transparency of metasurfaces," *Physical Review Letters*, vol. 112, no. 11, Article ID 117402, 2014.
- [43] D. Ramaccia, F. Bilotti, and A. Toscano, "Analytical model of a metasurface consisting of a regular array of sub-wavelength circular holes in a metal sheet," *Progress In Electromagnetics Research M*, vol. 18, pp. 209–219, 2011.
- [44] S. A. Tretyakov, "Metasurfaces for general transformations of electromagnetic fields," *Philosophical Transactions of the Royal Society A*, vol. 373, no. 2049, Article ID 20140362, 2015.
- [45] K. Achouri, B. A. Khan, S. Gupta, G. Lavigne, M. A. Salem, and C. Caloz, "Synthesis of electromagnetic metasurfaces: principles and illustrations," *EPJ Applied Metamaterials*, vol. 2, no. 12, pp. 1–11, 2016.
- [46] V. Asadchy, M. Albooyeh, S. Tcvetkova, Y. Radi, and S. A. Tretyakov, "Metasurfaces for perfect and full control of refraction and reflection," in *Proceedings of 10th International Congress on Advanced Electromagnetic Materials in Microwaves and Optics (METAMATERIALS)*, pp. 364–366, Greece, September 2016.
- [47] T. Niemi, A. O. Karilainen, and S. A. Tretyakov, "Synthesis of polarization transformers," *IEEE Transactions on Antennas and Propagation*, vol. 61, no. 6, pp. 3102–3111, 2013.
- [48] T. G. Mackay and A. Lakhtakia, *Electromagnetic Anisotropy and Bianisotropy: A Field Guide*, World Scientific Publishing Company, 2010.
- [49] C. Pfeiffer and A. Grbic, "Metamaterial Huygens' surfaces: tailoring wave fronts with reflectionless sheets," *Physical Review Letters*, vol. 110, no. 19, Article ID 197401, 2013.
- [50] H.-T. Chen, A. J. Taylor, and N. Yu, "A review of metasurfaces: physics and applications," *Reports on Progress in Physics*, pp. 1–44, 2016.
- [51] A. Alù, "Viewpoint: wave-shaping surfaces," *Physics*, 2013, <https://physics.aps.org/articles/v6/53>.
- [52] J. B. Pendry and D. R. Smith, "The quest for the superlens," *Scientific American*, vol. 295, no. 1, pp. 60–67, 2006.
- [53] A. E. Culhaoglu, A. V. Osipov, and P. Russer, "Imaging by a double negative metamaterial slab excited with an arbitrarily oriented dipole," *Radio Science*, vol. 49, no. 1, pp. 68–79, 2014.
- [54] J. P. Turpin, J. A. Bossard, K. L. Morgan, D. H. Werner, and P. L. Werner, "Reconfigurable and tunable metamaterials: a review of the theory and applications," *International Journal of Antennas and Propagation*, Article ID 429837, pp. 1–18, 2014.
- [55] A. Ahmed, I. A. Goldthorpe, and A. K. Khandani, "Electrically tunable materials for microwave applications," *Applied Physics Reviews*, vol. 2, no. 1, Article ID 011302, 2015.
- [56] Z. Sheng and V. V. Varadan, "Tuning the effective properties of metamaterials by changing the substrate properties," *Journal of Applied Physics*, vol. 101, no. 1, Article ID 014909, 2007.
- [57] M. Barbuto, A. Monti, F. Bilotti, and A. Toscano, "Design of a non-foster actively loaded SRR and application in metamaterial-inspired components," *IEEE Transactions on Antennas and Propagation*, vol. 61, no. 3, pp. 1219–1227, 2013.
- [58] D. Bouyge, D. Mardivirin, J. Bonache et al., "Split ring resonators (SRRs) based on micro-electro-mechanical deflectable cantilever-type rings: Application to tunable stopband filters," *IEEE Microwave and Wireless Components Letters*, vol. 21, no. 5, pp. 243–245, 2011.
- [59] T. Debogovic and J. Perruisseau-Carrier, "MEMS-reconfigurable metamaterials and antenna applications," *International Journal of Antennas and Propagation*, vol. 2014, Article ID 138138, 8 pages, 2014.
- [60] D. Peroulis, K. Sarabandi, and L. P. B. Katehi, "Design of reconfigurable slot antennas," *IEEE Transactions on Antennas and Propagation*, vol. 53, no. 2, pp. 645–654, 2005.
- [61] S. Shelley, J. Costantine, C. G. Christodoulou, D. E. Anagnostou, and J. C. Lyke, "FPGA-controlled switch-reconfigured antenna," *IEEE Antennas and Wireless Propagation Letters*, vol. 9, pp. 355–358, 2010.
- [62] D. Huang, E. Poutrina, and D. R. Smith, "Analysis of the power dependent tuning of a varactor-loaded metamaterial at microwave frequencies," *Applied Physics Letters*, vol. 96, no. 10, Article ID 104104, 2010.
- [63] E. Özbay, K. Aydin, S. Butun, K. Kolodziejek, and D. Pawlak, "Ferroelectric based tuneable SRR based metamaterial for microwave applications," in *Proceedings of European Microwave Conference, EUMC*, pp. 497–499, Germany, October 2007.
- [64] D. Shrekenhamer, W.-C. Chen, and W. J. Padilla, "Liquid crystal tunable metamaterial absorber," *Physical Review Letters*, vol. 110, no. 17, Article ID 177403, 2013.
- [65] Q. Zhao, L. Kang, B. Du et al., "Electrically tunable negative permeability metamaterials based on nematic liquid crystals," *Applied Physics Letters*, vol. 90, no. 1, Article ID 011112, 2007.
- [66] A. Ebrahimi, P. Yaghmaee, W. Withayachumnankul, C. Fumeaux, S. Al-Sarawi, and D. Abbott, "Interlayer tuning of X-band frequency-selective surface using liquid crystal," in *Proceedings of 3rd Asia-Pacific Microwave Conference, APMC 2013*, pp. 1118–1120, Korea, November 2013.
- [67] C. Kittel, "Introduction to Solid State Physics," in *Wiley Series on the Science and Technology of Materials*, Second edition, 1961.
- [68] K. Bi, G. Dong, X. Fu, and J. Zhou, "Ferrite based metamaterials with thermo-tunable negative refractive index," *Applied Physics Letters*, vol. 103, no. 13, Article ID 131915, 2013.
- [69] G. Oliveri, D. Werner, F. Bilotti, and C. Craeye, "Reconfigurable electromagnetics through metamaterials," *International Journal of Antennas and Propagation*, vol. 2014, Article ID 215394, 2 pages, 2014.
- [70] T.-C. Pu, H.-H. Lin, C.-Y. Wu, and J.-H. Chen, "Photovoltaic panel as metamaterial antenna radome for dual-band application," *Microwave and Optical Technology Letters*, vol. 53, no. 10, pp. 2382–2388, 2011.

- [71] H. Boutayeb and T. A. Denidni, "Internally excited fabry-Pérot type cavity: power normalization and directivity evaluation," *IEEE Antennas and Wireless Propagation Letters*, vol. 5, no. 1, pp. 159–162, 2006.
- [72] R. Basiry, H. Abiri, and A. Yahaghi, "Electromagnetic performance analysis of omega-type metamaterial radomes," *International Journal of RF and Microwave Computer-Aided Engineering*, vol. 21, no. 6, pp. 665–673, 2011.
- [73] H.-N. Liu, H.-L. Su, K.-H. Lin, C.-Y. Wu, C.-L. Tang, and S.-H. Yeh, "Design of antenna radome composed of metamaterials for high gain," in *Proceedings of IEEE Antennas and Propagation Society International Symposium, APS 2006*, pp. 19–22, USA, July 2006.
- [74] H. Cory, Y. J. Lee, Y. Hao, and C. G. Parini, "Use of conjugate dielectric and metamaterial slabs as radomes," *IET Microwaves, Antennas and Propagation*, vol. 1, no. 1, pp. 137–143, 2007.
- [75] K.-S. Chen, K.-H. Lin, and H.-L. Su, "Microstrip antenna gain enhancement by metamaterial radome with more subwavelength holes," in *Proceedings of Asia Pacific Microwave Conference 2009, APMC 2009*, pp. 790–792, Singapore, December 2009.
- [76] T. Crépin, C. Martel, B. Gabard et al., "Blind spot mitigation in phased array antenna using metamaterials," in *Proceedings of International Radar Conference, Radar 2014*, 4 pages, France, October 2014.
- [77] D. M. Pozar and D. H. Schaubert, "Scan blindness in infinite phased arrays of printed dipoles," *IEEE Transactions on Antennas and Propagation*, vol. 32, no. 6, pp. 602–610, 1984.
- [78] M. Latrach, H. Rmili, C. Sabatier, E. Seguenot, and S. Toutain, "Design of a new type of metamaterial radome for low frequencies," *Microwave and Optical Technology Letters*, vol. 52, no. 5, pp. 1119–1123, 2010.
- [79] H.-L. Su, H.-C. Huang, K.-H. Lin, C.-Y. Wu, and H.-H. Lin, "Gain-enhanced metamaterial radome for circularly-polarized antenna," in *Proceedings of IEEE International Symposium on Antennas and Propagation and CNC-USNC/URSI Radio Science Meeting, AP-S/URSI 2010*, pp. 661–664, Canada, July 2010.
- [80] X. G. Zhang, X. G. Miao, X. W. Fang et al., "Artificial ceramic metamaterial with meshed grid structure for radome application," *Advanced Materials Research*, vol. 893, pp. 11–14, 2014.
- [81] R. Dubrovka, G. Palikaras, and P. Belov, "Near-field antenna radome based on extremely anisotropic metamaterial," *IEEE Antennas and Wireless Propagation Letters*, vol. 11, pp. 438–441, 2012.
- [82] A. V. Osipov, E. Kemptner, E. Özis, and H. Kobayashi, "Microwave metamaterials for increased survivability of future systems," *IEICE Technical Report*, vol. 116, no. 427, pp. 35–40, January 2017.
- [83] T. Jiang, Z. Wang, D. Li et al., "Low-DC voltage-controlled steering-antenna radome utilizing tunable active metamaterial," *IEEE Transactions on Microwave Theory and Techniques*, vol. 60, no. 1, pp. 170–178, 2012.
- [84] V. G. Harris, A. Geiler, Y. Chen et al., "Recent advances in processing and applications of microwave ferrites," *Journal of Magnetism and Magnetic Materials*, vol. 321, no. 14, pp. 2035–2047, 2009.
- [85] A. Parsa, T. Kodera, and C. Caloz, "Ferrite based non-reciprocal radome, generalized scattering matrix analysis and experimental demonstration," *IEEE Transactions on Antennas and Propagation*, vol. 59, no. 3, pp. 810–817, 2011.
- [86] White Paper, *Narrowband technology: the most intelligent choice for wireless connectivity in the most expansive outdoor spaces (Choosing the right wireless network for expansive outdoor spaces)*, Zebra Technologies, 2015.
- [87] D. J. Kozakoff, "Multi-frequency and ultrawideband antenna radomes," Antenna Systems 2011, USA, September 2011, available at <http://www.slideserve.com/duy/multi-frequency-and-ultrawideband-antenna-radomes>.
- [88] R.-X. Wu, Y. Gu, and L. Tan, "Optimizing the directional radiation of metamaterial antenna," in *Proceedings of 7th International Congress on Advanced Electromagnetic Materials in Microwaves and Optics, METAMATERIALS 2013*, pp. 106–108, France, September 2013.
- [89] L.-M. Si and X. Lv, "CPW-fed multi-band omni-directional planar microstrip antenna using composite metamaterial resonators for wireless communications," *Progress in Electromagnetics Research*, vol. 83, pp. 133–146, 2008.
- [90] P. P. Bhattacharya, R. Khandelwal, R. Gera, and A. Agarwal, "Smart radio spectrum management for cognitive radio," *International Journal of Distributed and Parallel Systems (IJDPDS)*, vol. 2, no. 4, pp. 12–24, July 2011.
- [91] P.-Y. Qin, F. Wei, and Y. J. Guo, "A Wideband-to-Narrowband Tunable Antenna Using A Reconfigurable Filter," *IEEE Transactions on Antennas and Propagation*, vol. 63, no. 5, pp. 2282–2285, 2015.
- [92] Y. Tawk and C. G. Christodoulou, "A new reconfigurable antenna design for cognitive radio," *IEEE Antennas and Wireless Propagation Letters*, vol. 8, pp. 1378–1381, 2009.
- [93] G. Prema and P. Gayatri, "A frequency reconfigurable rotatable antenna design for cognitive radio systems," *International Journal of Engineering Research and Technology (IJERT)*, vol. 2, no. 12, pp. 1342–1349, December 2013.
- [94] Y. Liu and X. Zhang, "Metamaterials: a new frontier of science and technology," *Chemical Society Reviews*, vol. 40, no. 5, pp. 2494–2507, 2011.
- [95] O. Vanbesien, *Artificial Materials*, Wiley, 2012.
- [96] C. R. Simovski, M. S. Kondratiev, P. A. Belov, and S. A. Tretyakov, "Excitation dyadics for the grids of chiral and omega particles," in *Proceedings of SPIE the Smart Structures and Materials 1997: Mathematics and Control in Smart Structures*, vol. 3039, pp. 692–703, USA, March 1997.
- [97] J. A. Gordon, C. L. Holloway, and A. Dienstfrey, "A physical explanation of angle-independent reflection and transmission properties of metafilms/metasurfaces," *IEEE Antennas and Wireless Propagation Letters*, vol. 8, pp. 1127–1130, 2009.

## Research Article

# Carbon Fiber Reinforced Polymer with Shredded Fibers: Quasi-Isotropic Material Properties and Antenna Performance

Gerald Artner,<sup>1,2</sup> Philipp K. Gentner,<sup>1,2</sup> Johann Nicolics,<sup>3</sup>  
and Christoph F. Mecklenbräuer<sup>1,2</sup>

<sup>1</sup>The Christian Doppler Laboratory for Wireless Technologies for Sustainable Mobility, Vienna, Austria

<sup>2</sup>Institute of Telecommunications, Technische Universität Wien, Vienna, Austria

<sup>3</sup>The Institute of Sensor and Actuator Systems, Technische Universität Wien, Wien, Austria

Correspondence should be addressed to Gerald Artner; [gerald.artner@nt.tuwien.ac.at](mailto:gerald.artner@nt.tuwien.ac.at)

Received 19 January 2017; Revised 6 April 2017; Accepted 20 April 2017; Published 29 May 2017

Academic Editor: Mirko Barbuto

Copyright © 2017 Gerald Artner et al. This is an open access article distributed under the Creative Commons Attribution License, which permits unrestricted use, distribution, and reproduction in any medium, provided the original work is properly cited.

A carbon fiber reinforced polymer (CFRP) laminate, with the top layer consisting of shredded fibers, is proposed and manufactured. The shredded fibers are aligned randomly on the surface to achieve a more isotropic conductivity, as is desired in antenna applications. Moreover, fiber shreds can be recycled from carbon fiber composites. Conductivity, permittivity, and permeability are obtained with the Nicolson-Ross-Weir method from material samples measured inside rectangular waveguides in the frequency range of 4 to 6 GHz. The decrease in material anisotropy results in negligible influence on antennas. This is shown by measuring the proposed CFRP as ground plane material for both a narrowband wire monopole antenna for 5.9 GHz and an ultrawideband conical monopole antenna for 1–10 GHz. For comparison, all measurements are repeated with a twill-weave CFRP.

## 1. Introduction

Composites are materials consisting of a mixture of components present as separate phases. They are created for engineering applications to combine the desired qualities of its individual components. Carbon fiber reinforced polymers (CFRP) are carbon fiber composites (CFC) consisting of carbon fibers embedded in a polymer matrix, typically a resin. The most common production technique is to build CFRP as laminates. These laminates are stacked from unidirectional or woven carbon fiber plies preimpregnated with resin, which are commonly referred to as prepreg. The laminate is stacked in a mold to form the desired part geometry, vacuum-bagged, and cured in an autoclave.

The motivation to use CFRP is found in their mechanical properties. While Young's modulus  $E$  of CFRP is lower than that of many metals, the density of CFRP is much lower. Young's modulus per material density of CFRP is much higher than that of metals; for example, the specific tensile modulus of steel is about  $26 \text{ GPa}/(\text{g}/\text{cm}^3)$ , while for unidirectional CFRP (UD-CFRP) values  $> 100 \text{ GPa}/(\text{g}/\text{cm}^3)$  can be

easily achieved in fiber direction. This makes CFRP a suitable material for lightweight construction.

Carbon fibers are electric conductors, while the matrix is almost exclusively nonconductive. The electromagnetic properties of CFRP laminates are in general anisotropic and depend on fiber and matrix materials, ply weave, orientation of the layers in the laminate, and frequency. In the past, due to their application in avionics and aeronautics, the research focus was on the electromagnetic shielding properties of carbon fiber composites [1, 2]. For antenna design the electrical conductivity, permittivity, and magnetic permeability of the materials in the vicinity of the antenna are of interest.

Measurements of radio-frequency electromagnetic properties are performed by inserting a material sample (material under test, MUT) inside a well understood system, such as a waveguide [3, 4] and coaxial cable, or between horn antennas [5]. The electrical conductivity and permittivity transverse and parallel to UD-CFRP and with different fiber volume fractions were measured with waveguides in [6]; values are given in a large frequency range up to 10 GHz. The conductivity of CFRP is much higher than that of carbon-black

or graphite particulate composites [7]; conductivity of UD-CFRP in and perpendicular to fiber direction differs by a factor of  $10^5$ . Horn antenna measurements have shown that the conductivity of CFC with unidirectional fibers increases with frequency if the electrical field is perpendicular to the fibers but is flat with the field parallel to the fiber direction [8]. Waveguide measurements of electrical conductivity and permittivity with the Nicolson-Ross-Weir (NRW) method and different ply orientation in the range of 8 GHz to 12 GHz have been conducted in [9], where they also provide measurements of CFRP slot antennas. CFRP are diamagnetic; the magnetic permeability of unidirectional carbon fiber polymer laminates was measured with horn antennas and waveguides in [10]. In most investigations only CFRP made with unidirectional fiber direction, and plies which are all oriented in the same direction, are considered. UD-CFRP are more interesting from a theoretical viewpoint as the material anisotropy is more pronounced and the material is easier to model. In applications however, woven fabrics are often used to compensate the small  $E$ -module and/or low electric conductivity perpendicular to fiber direction.

Modeling approaches for the electrical properties of CFC have been proposed in [11, 12] in addition to simple law of mixture models used in [1, 13].

CFRP are used in a variety of antenna applications. The whole antenna can be built from CFRP. Measurements of braided CFRP patch antennas are compared to law of mixture and geometry based simulations in [14]. The performance of bow-tie antennas with unidirectional and braided CFRP is measured in [15]. Various monopole antennas made from CFRP and carbon nanotubes are investigated in [16, 17]. Slotted waveguide antennas manufactured from CFRP are investigated in [18]. This type of antenna is especially relevant in aeronautical applications. Load bearing structures are formed from CFRP and the geometry obtained for mechanical stability is close to the geometry of rectangular waveguides. CFRP bearers can be used as rectangular waveguides and slots can be cut into them to build rectangular waveguide antennas [19]. Several elements can be combined into an antenna array, the slotted waveguide antenna stiffened structure [20].

CFRP are used for lightweight construction of reflectors, mostly in large parabolic dishes [21] or space applications [22]. Measurements in [23] show that CFRP is applicable as reflector material for millimeter-wave antennas at 100 GHz. Antenna gain with a reflector made from woven CFRP is close to the gain with a chrome plated reflector. It should be noted that CFRP cannot be used in some antenna applications as they are a source of intermodulation products [24].

CFRP are used as antenna ground plane material. In specialized applications the high anisotropy of UD-CFRP can be utilized. A mechanically reconfigurable antenna with an anisotropic CFRP ground plane is presented in [25]. Surface currents on the ground plane can flow in fiber direction, while they are blocked perpendicular to fiber direction due to the low conductivity of CFRP. This mechanism acts as a mode filter for a patch antenna which is rotated against the CFRP ground plane. In general, however, the conductivity of the antenna ground plane should be isotropic.

A typical use case as ground plane is when antennas are mounted on large CFRP structures such as an aircraft fuselage or a car chassis. The influence of the ground plane material on the antennas should be small to allow antenna design independent of composite design. To achieve this, CFRP with near anisotropic conductivity are preferred, such that electric currents are not obstructed. This is especially the case in automotive antenna design, where antenna modules are used on different types of vehicle and are required to function on the CFRP roof of electric cars as well as on steel roofs. An automotive roof mounted antenna module (shark-fin) is measured on a CFRP car roof in [26]. An antenna cavity for integration into CFRP sheets, such as aircraft skin panels or car chassis, is proposed and prototyped in [27]. In vehicular applications the antenna cavity can be manufactured as part of a carbon fiber reinforced car roof as is described in [28].

A CFRP material with carbon fiber shreds in random alignment as its top layer is proposed for antenna applications and manufactured. Fiber shreds can be obtained from recycled CFRP, resulting in a sustainable material. Due to the skin effect, it is sufficient to design the top layer of the laminate for antenna applications in the gigahertz range; the other plies can be chosen independently to meet the mechanical requirements of the composite. The material is described in Section 2. Its electromagnetic properties are measured with the NRW method in a rectangular waveguide and compared to a CFRP with a 2/2 twill weave in Section 3.1. Material measurements are performed in the frequency band from 4 GHz to 6 GHz, which includes the frequency band from 5.85 GHz to 5.925 GHz, that is reserved for dedicated short range communication (DSRC) in intelligent transportation systems (ITS), IEEE 802.11p. The influence of the proposed CFRP as ground plane material is measured with several monopole antennas in Section 4. The proposed CFRP is measured as ground plane for a wire monopole antenna for the 5.9 GHz DSRC band and with broadband conical monopole antennas in a frequency range from 1 GHz to 10 GHz.

## 2. CFRP for Antenna Applications

In general, the influence of a CFRP ground plane on the antenna should be small. For antenna applications CFC are preferred over graphite or carbon-black particulate composites due to their larger conductivity in fiber direction [7]. Woven carbon fiber plies are used to achieve a more isotropic conductivity than unidirectional plies [8]. However, the geometry of a chosen weave might result in unwanted resonances. A straightforward method to diminish the anisotropic conductivity of CFRP is to superimpose an isotropic metallic layer onto the CFRP, include it in the laminate during production, or metalize the CFRP surface. In many applications this is not possible because of the different thermal expansion coefficients of the materials or simply because of too high costs.

It is proposed to use a CFRP with fiber shreds in random alignment in antenna applications. Random fiber alignment results in a composite with a more isotropic conductivity than UD-CFRP and does not have characteristic geometries

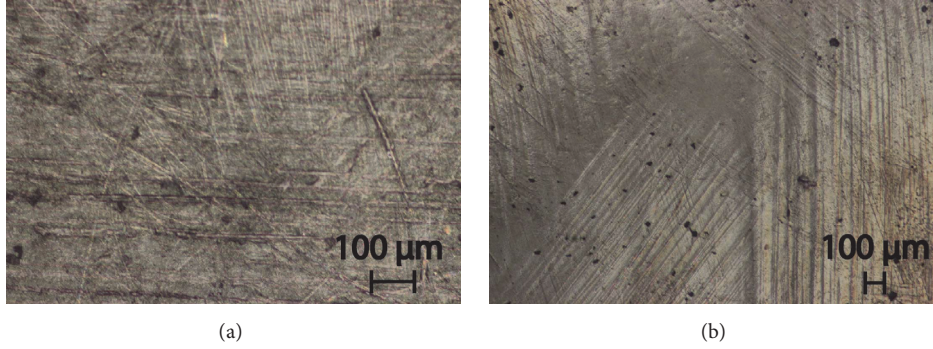


FIGURE 1: Microscopic photographs of (a) the proposed CFRP with fiber shreds in random alignment on top and (b) the twill-weave CFRP reference material. The unidirectional filaments are visible underneath the fiber shreds as horizontal lines.

associated with woven carbon plies. The quasi-random fiber alignment is easy in production, as the fiber shreds can be dropped or blown onto the mold or laminate. Fiber shreds can be obtained from CFRP recycling processes [29]. Due to the skin effect it is sufficient to design the top layer of the laminate for antenna applications; the remaining plies can be designed to meet mechanical requirements.

A microscopic photograph of a material sample taken from a CFRP with unidirectional plies and fiber shreds in random alignment on top is depicted in Figure 1(a). The unidirectional filaments under the fiber shreds are visible as horizontal lines in the photograph. In production the fiber shreds are of course not aligned completely random; an example is depicted on the top border of Figure 1(a), where a bundle of carbon fiber shreds is aligned facing downwards. The shred-CFRP has a total thickness of 2.26 mm. The material is compared to a 2/2 twill-weave CFRP depicted in Figure 1(b). The twill-CFRP has a thickness of 0.9 mm, consists of 5 layers of 2/2 twill weave stacked as [45 90 45 90 45], and has 1000 fiber filaments per roving.

### 3. Material Measurements

**3.1. NRW Method.** The electromagnetic properties (conductivity, permittivity, and permeability) of the proposed CFRP with fiber snippets on top are measured at radio frequencies. Results are compared to measurements of a CFRP with a twill weave as described in Section 2. Values for UD-CFRP are already well known in literature. A method developed by Nicolson-Ross-Weir (NRW) [30, 31] enables the characterization of material samples inside a waveguide by calculating the electrical characteristics from measured scattering parameters (S-parameters). Rectangular material samples are cut from the CFRP and placed in a fixture inside a rectangular waveguide that operates in its dominant TE<sub>10</sub> mode. The waveguide is connected to a vector network analyzer and S-parameters are measured. The NRW method is then used to calculate the electrical and magnetic material parameters from the S-parameters obtained by waveguide measurements. The formulas for S-parameter conversion, where the complex material parameters  $\epsilon_r$ ,  $\mu_r$  and the conductivity  $\sigma$  are extracted, can be found in [5, 32]. The position of the MUT inside the fixture is considered according to

[32], where  $L_1$  and  $L_2$  are the distance from the MUT to the calibration plane of port 1 and port 2 inside the waveguide, respectively:

$$R_i = e^{-\gamma_0 L_i}, \quad i \in \{1, 2\},$$

$$S_{11}^C = \frac{S_{11}}{R_1^2}, \quad (1)$$

$$S_{21}^C = \frac{S_{21}}{R_1 R_2}.$$

The scattering parameters  $S_{11}^C$  and  $S_{21}^C$  are the basis for the Nicolson-Ross-Weir (NRW) equations:

$$\Gamma = X \pm \sqrt{X^2 - 1}, \quad (2)$$

$$X = \frac{(S_{11}^C)^2 - (S_{21}^C)^2 + 1}{2S_{11}^C}, \quad (3)$$

$$\frac{1}{\Lambda^2} = -\left(\frac{1}{2\pi d} \ln\left(\frac{1}{P}\right)\right)^2, \quad (4)$$

$$P = \frac{S_{11}^C + S_{21}^C - \Gamma}{1 - (S_{11}^C + S_{21}^C)\Gamma}, \quad (5)$$

with the thickness of the MUT  $d$  and propagation factor  $P$  and with the sign in (2) to be chosen such that the reflection coefficient is  $|\Gamma| \leq 1$ .  $\text{Re}\{1/\Lambda\} = 1/\lambda_g$  with the transmission line guide wavelength  $\lambda_g$ . Note that the logarithm in (4) is ambiguous by  $2\pi n$ ,  $n \in \mathbb{N}_0$ , as  $P$  is complex in general. The ambiguity problem is resolved by choosing *thin* samples of thickness  $d < \lambda/2$  [32], resulting in  $n = 0$ . This is the case for the presented CFRP measurements in the low gigahertz range, as these composites are commonly manufactured as (thin) laminates. To check whether the  $n = 0$  assumption is valid, the method based on group delay from [31] was also implemented. For this method the group delay is calculated for each frequency as  $\tau_{gn}$  and compared to the group delay

$\tau_g$ , which is based on the slope of the propagation factor  $P$

$$\tau_{gn} = d \cdot \frac{d}{df} \left[ \left( \frac{\epsilon_r \mu_r}{\lambda_0^2} - \frac{1}{\lambda_c^2} \right)_n^{1/2} \right], \quad (6)$$

$$\tau_g = \frac{1}{2\pi} \frac{d(-\phi)}{df},$$

with  $\phi = \arg(P)$ . The derivatives in (6) are approximated by finite differences between measured frequency bins. The correct root  $n = k$  is then chosen such that  $\tau_{gk} - \tau_g \approx 0$ . The group delay method also resulted in  $n = 0$  in the frequency band of the fundamental mode of the waveguide.

The complex magnetic permeability and electric permittivity are then obtained as

$$\mu_r = \mu_r' - j\mu_r'' = \frac{1 + \Gamma}{\Lambda(1 - \Gamma) \sqrt{1/\lambda_0^2 - 1/\lambda_c^2}}, \quad (7)$$

$$\epsilon_r = \epsilon_r' - j\epsilon_r'' = \frac{\lambda_0^2}{\mu_r} \left( \frac{1}{\lambda_c^2} + \frac{1}{\Lambda^2} \right).$$

In (7)  $\lambda_0$  denotes the wavelength in free space at measurement frequency and  $\lambda_c$  the cut-off frequency of the waveguide.

The surface conductivity of the material is derived from

$$\sigma = \frac{4\pi\mu_0 f (1 - |S_{11}|^2)^2}{Z_0^2 \left( (1 + |S_{11}|^2) - \sqrt{-|S_{11}|^4 + 6|S_{11}|^2 - 1} \right)^2}, \quad (8)$$

with the magnetic constant  $\mu_0$ , frequency  $f$ , and the free space impedance  $Z_0$ ; see [9].

**3.2. Measurement Setup.** The waveguide WR187 has a dimension of  $a = 47.5 \text{ mm} \times b = 22.1 \text{ mm}$ . The cut-off frequency of the  $\text{TE}_{10}$  mode is  $f_c = c_0/2a \approx 3.16 \text{ GHz}$  and the nominal frequency range is 3.94–5.99 GHz.

Samples are cut from the CFRP materials for a selected set of discrete orientations and grinded to fit into a waveguide fixture. The waveguide was cleaned with alcohol and calibrated using a through-reflect-match (TRM) calibration. The fixture with the sample is then fastened in the middle of the waveguide, the  $S$ -parameters are measured with a network analyzer (R&S ZVA24), and the electrical properties are calculated in a Matlab script as presented in Section 3.1. The disassembled measurement setup is depicted in Figure 2.

To measure the angular dependency of the materials, the samples are cut in various orientations  $\varphi$ . Twill-CFRP sample orientations range from  $0^\circ$  to  $90^\circ$  in steps of  $10^\circ$  and shred-CFRP samples are cut from  $0^\circ$  to  $110^\circ$  in  $5^\circ$  steps, where  $\varphi$  is the deviation from an arbitrary defined direction on the material surface. Three additional samples with  $\varphi = 0^\circ$  are cut from different positions of shred-CFRP to assess the impact of cutting precision and material inhomogeneity.

There are several known sources of inaccuracies when measuring material samples inside a waveguide. The sample might be displaced inadvertently from the calibration plane.

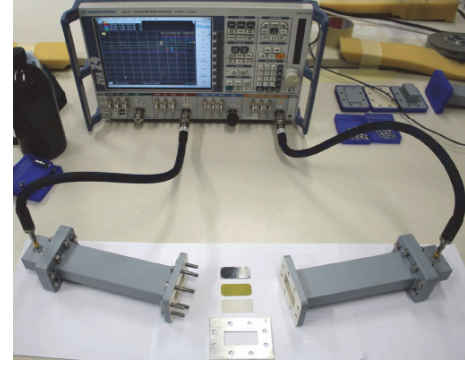


FIGURE 2: Measurement setup consisting of WR187 waveguides, sample fixture, and R&S ZVA24 network analyzer.



FIGURE 3: Attachment of a sample with air-gap in the waveguide fixture by clamping a piece of styrofoam into the air-gap, on the example of a twill-CFRP sample with an alignment of  $60^\circ$ .

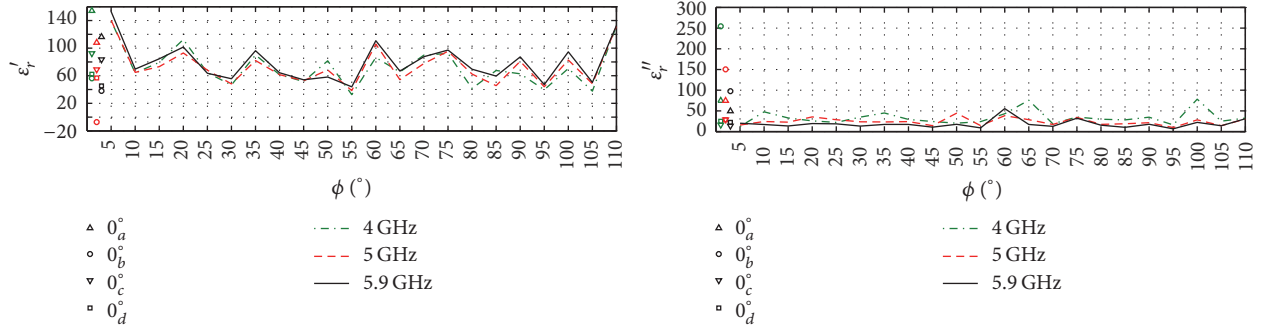
It may tilt and, due to imprecise manufacturing, air-gaps might appear between sample and the waveguide walls. To mitigate these sources of inaccuracies, a small piece of styrofoam is clamped between sample and fixture when necessary, as shown in Figure 3.

**3.3. Measurement Results.** Results for the permittivity, permeability, and conductivity of shred-CFRP are presented in Figures 4(a), 5(a), and 6(a), respectively and results for twill-CFRP are depicted in Figures 4(b), 5(b), and 6(b), respectively. The orientation dependent results are shown for 4 GHz, 5 GHz, and 5.9 GHz (ITS G5). Measured values for different sample orientations are connected by straight lines only for visual guidance.

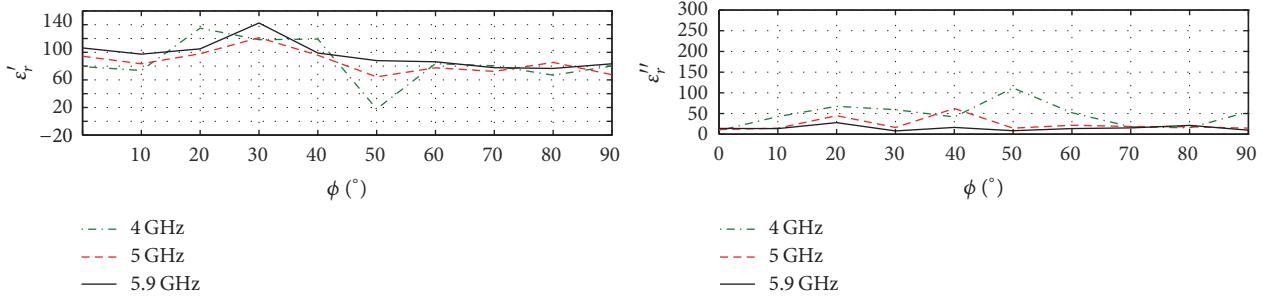
The permittivity of the two CFRP is high when compared to [6], where  $\epsilon_r$  for unidirectional fibers in epoxy was around 1 for electrical field parallel to fiber alignment and ranged from 5 to 20 for transverse fields, and [9], where  $\epsilon_r$  was approximately 30 for both unidirectional and [0 45 90 -45] fiber alignment.

Twill-CFRP shows strong dependency of  $\mu_r$  on the angle, while all measured shred-CFRP samples have low  $\mu_r$  independent of their alignment. The diamagnetic behavior of CFRP (Figure 5) is in accordance with [10], where the real part of  $\mu_r$  varies between 0 and 1 dependent on orientation of a UD-CFRP.

The conductivity anisotropy of the shred-CFRP (and the twill-CFRP) is significantly lower than that of UD-CFRP. The

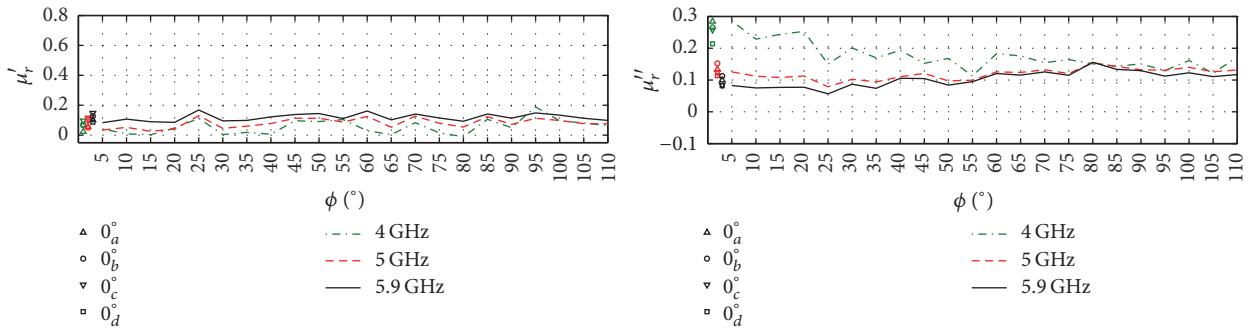


(a) Permittivity, shred-CFRP

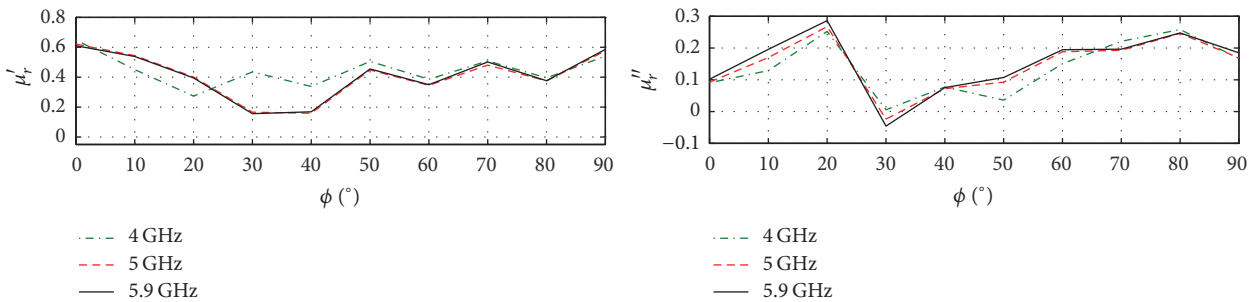


(b) Permittivity, twill-CFRP

FIGURE 4: Permittivity of (a) shred-CFRP and (b) twill-CFRP dependent on the orientation of the cut sample.



(a) Permeability, shred-CFRP



(b) Permeability, twill-CFRP

FIGURE 5: Permeability of (a) shred-CFRP and (b) twill-CFRP dependent on the orientation of the cut sample.

conductivity of shred-CFRP is about  $10^4$  S/m. Conductivity varies by a factor of 10 depending on the angle for a given frequency. Reference [7] reports a factor of  $10^5$  between conductivity in fiber direction ( $\approx 10^2$  S/cm) and that perpendicular to fiber direction ( $\approx 10^{-3}$  S/cm). Reference [6] reports

a longitudinal conductivity of  $\approx 400$  S/cm with a sharp decline towards zero between  $10^8$  Hz and  $10^{10}$  Hz and transverse conductivity around  $10^{-2}$  S/cm. For a CFRP with unidirectional plies that are stacked as  $[0 \ 45 \ 90 \ -45]_{2s}$  conductivity varies between 5000 S/m (parallel) and 1000 S/cm

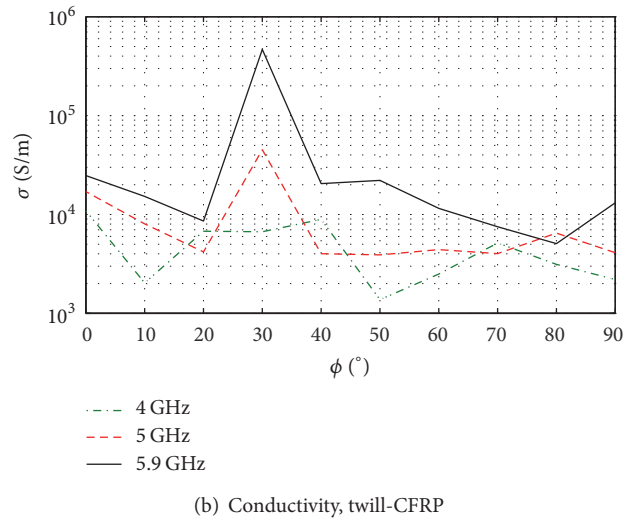
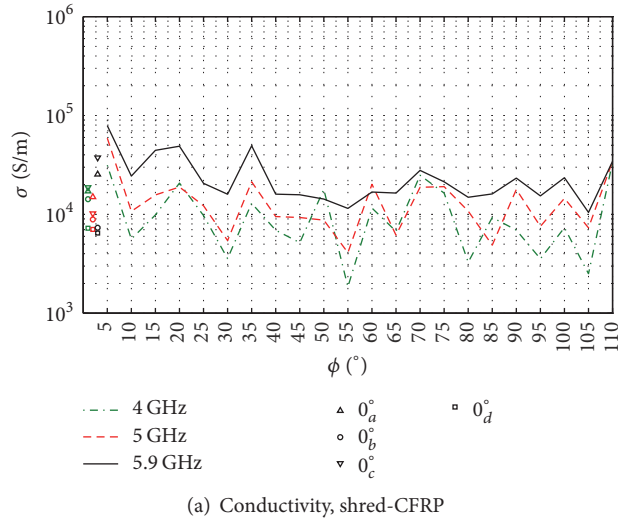


FIGURE 6: Conductivity of (a) shred-CFRP and (b) twill-CFRP dependent on the orientation of the cut sample.

(perpendicular) [9] (8–12 GHz). The conductivity of the shred-CFRP is slightly higher than that of the twill-CFRP.

Note that the NRW estimates allow slightly negative values for the magnetic permeability, although such negative values are not compatible with passivity of the material. These stem from measurement inaccuracies together with the numerical sensitivity of the NRW method which does not enforce passivity of the material. Negative parameter estimates become apparent when the permeability is close to zero, as depicted in Figure 5(a). The  $\epsilon_r'$  value of the  $0^\circ_b$  shred-CFRP sample in Figure 4(a) and  $\mu_r''$  of the  $30^\circ$  twill-CFRP sample in Figure 5(b) serve as indicators for the overall accuracy of the parameter estimates.

To investigate the homogeneity of the shred-CFRP, four samples with the same orientation were cut from different regions of the material. They are referred to as  $0^\circ_a$ ,  $0^\circ_b$ ,  $0^\circ_c$ , and  $0^\circ_d$ . The conductivity measurements of these four samples dependent on frequency are depicted in Figure 7. Although the four samples in Figure 7 have the same orientation, their frequency behavior is different. The conductivity of samples  $0^\circ_a$  and  $0^\circ_c$  increases with increasing frequency, the conductivity of sample  $0^\circ_b$  decreases with frequency, and the conductivity of sample  $0^\circ_d$  stays approximately the same over the investigated frequency range. Additionally, the spread of values for the  $0^\circ$  samples resembles the value range of the other samples in Figures 4(a), 5(a), and 6(a). The conclusion must be that the material is either inhomogeneous or that the measurements are not accurate enough to measure an angular dependency of the radio-frequency properties of the proposed CFRP. The microscopic photograph depicted in Figure 1(a) suggests that the proposed CFRP is not homogenous, as fibers were not uniformly distributed during production and strands of fibers with same alignment are still present on the surface. However, it is shown in Section 4 that the local inhomogeneity and anisotropy of the CFRP ground plane with fiber shreds have no relevant influence on monopole antennas.

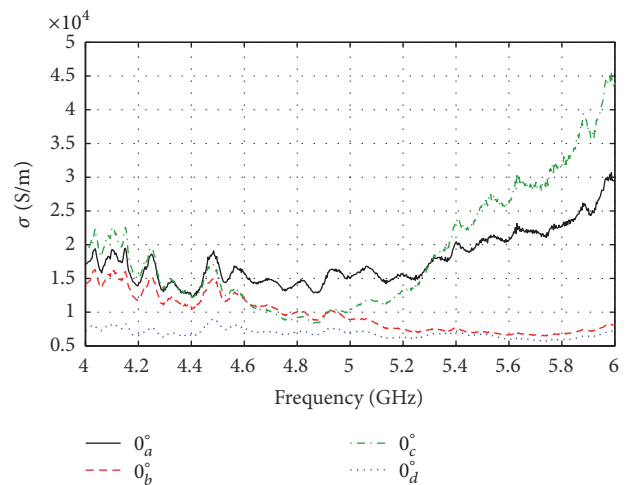


FIGURE 7: Conductivity of four shred-CFRP samples with the same alignment ( $0^\circ$ ), cut from different positions of the material.

At 5.9 GHz the fiber shreds of shred-CFRP lead to a smaller spread of conductivity values than a woven structure like that of twill-CFRP. The conductivity of shred-CFRP varies only between  $10^4$  S/m and  $8 \cdot 10^4$  S/m at 5.9 GHz. When building monopole antennas with a shred-CFRP ground plane, this change leads to a negligible influence on antenna radiation patterns as presented in Section 4.1. Broadband measurements of conical monopole antennas in Section 4.2 show that shred-CFRP is an excellent ground plane material with results close to aluminum.

#### 4. Antennas with CFRP Ground Planes

To the best of the authors' knowledge, the first measurement of the influence of CFRP as a ground plane material of a monopole antenna was performed in [33] for 1 GHz.

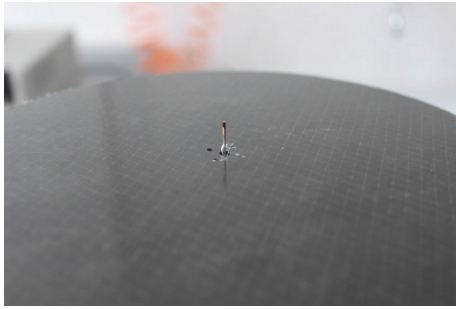


FIGURE 8: Monopole antenna for 5.9 GHz on a circular shred-CFRP ground plane.

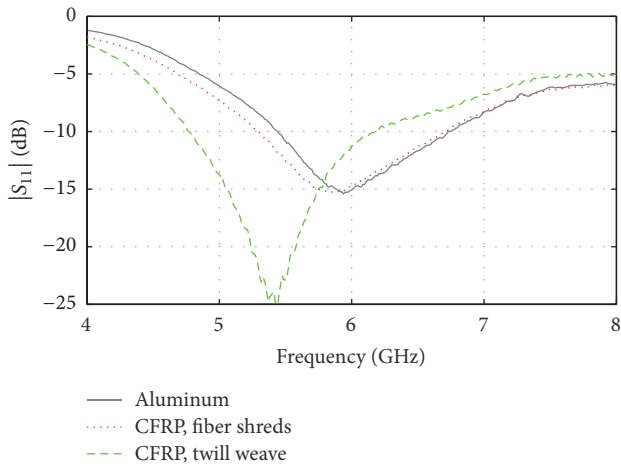


FIGURE 9: Measured S-parameters of the wire monopole antennas on different ground planes (reprinted with permission from [34]; ©2014 IEEE).

The influence of the composite anisotropy was undetectable within the measurement accuracy. However, no detailed description of the investigated CFRP was given. Monopole antennas are investigated, because they are well known antennas and are already used in various applications where large CFRP ground planes are available. Performance of shred-CFRP is expected to be similar for other antenna types.

**4.1. Wire Monopole Antenna for 5.9 GHz.** A wire monopole antenna for DSRC at 5.9 GHz is measured on CFRP ground planes [34]. The monopole antenna is a metal wire cut to a length of about  $\lambda/4$  such that it is resonant at 5.9 GHz. The wire is soldered to the inner connector of a subminiature version A (SMA) flange, which is screwed to threaded holes in the ground plane. The wire monopole antenna is measured on circular ground planes with 195 mm diameters. The wire monopole antenna on a circular ground plane from shred-CFRP is depicted in Figure 8. The shred-CFRP and twill-CFRP are the same as in Section 3.

To measure the influence of a CFRP ground plane on a narrowband antenna, the monopole wire is trimmed such that it is resonant at 5.9 GHz on an aluminum ground plane. The measured S-parameters are depicted in Figure 9. The resonance frequency of the antenna is shifted to about

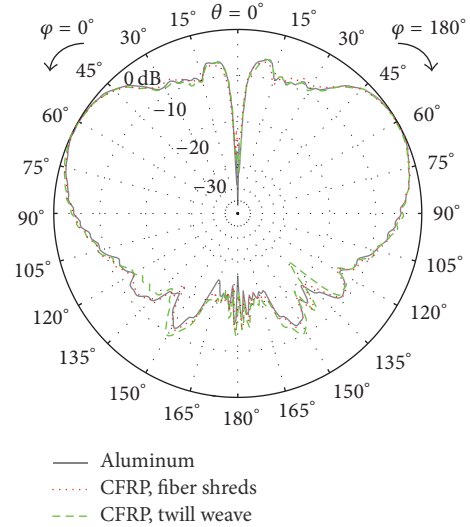


FIGURE 10: Monopole antenna for 5.9 GHz on a circular ground plane. Vertical cut of the normalized measured gain pattern for azimuth  $\varphi = 0^\circ$  (reprinted with permission from [34]; ©2014 IEEE).

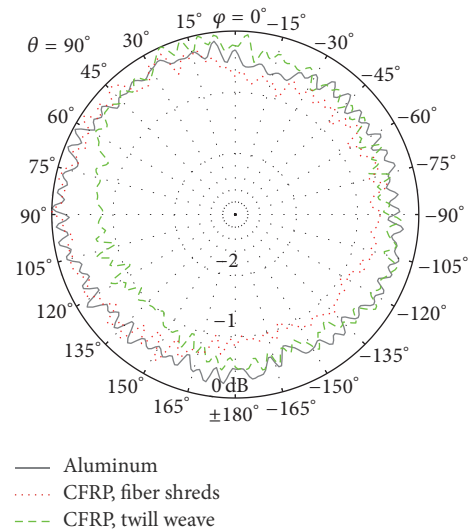


FIGURE 11: Monopole antenna for 5.9 GHz on a circular ground plane. Horizontal cut of the normalized measured gain pattern for polar angle  $\theta = 90^\circ$  (reprinted with permission from [34]; ©2014 IEEE).

5.4 GHz when placed on the twill-CFRP. The length of the wire was not adjusted, as the return loss at 5.9 GHz is still better than 10 dB. In a practical application the dimensions will be adjusted, such that the antenna is resonant at the desired frequency.

Gain pattern measurements are performed inside the institute’s anechoic chamber. The vertical cuts of the gain patterns at azimuth  $\varphi = 0^\circ$  are shown in Figure 10. The horizontal cuts of the measured gain patterns are depicted in Figure 11. The patterns are normalized. Vertical cuts of the patterns show no significant deviation; no additional zeros or notches are introduced by the shred-CFRP. The influence

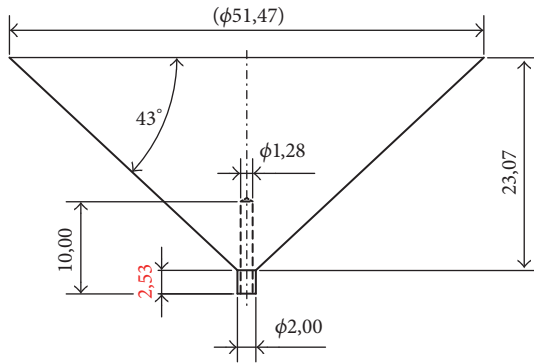


FIGURE 12: Cone dimensions of the broadband monopole antenna. The cylindrical stub on the bottom (red) is designed to fit over the inner conductor of an SMA flange, its length is adjusted to the thickness of the ground plane. All dimensions are in millimeter (reprinted with permission from [35]; ©2017 IEEE).

of the shred-CFRP on the antenna's radiation pattern in the horizontal plane is smaller than 1 dB and can be neglected in most applications. Radiation efficiency on the shred-CFRP ground plane is reduced by 23% (1.14 dB) compared to the efficiency on an aluminum ground plane in [34].

**4.2. Conical Monopole Antenna on CFRP Ground Planes.** Conical monopole antennas turned from brass are used to measure the influence of CFRP as ground plane material on antennas from 1 GHz to 10 GHz [35]. Cone dimensions are depicted in Figure 12. The cones have cylindrical stubs at the tip that fit tightly over the inner conductor of a coaxial SMA flange. As the ground planes have different thickness, several cones are manufactured with different lengths of the stubs, such that the tip of the cone is always positioned at the surface level of the material. The SMA flanges are screwed to threaded holes drilled into the ground planes. The antennas are measured on circular ground planes manufactured from shred-CFRP, twill-weave CFRP, UD-CFRP, and aluminum. All ground planes have a diameter of 300 mm. As threading the thin twill-CFRP ground plane in Section 4.1 was challenging, a thicker twill-CFRP was used as reference material for the measurements of the conical monopole antennas. The twill-CFRP is a 1.6 mm thick 2/2 twill weave stacked as [0 90] that is commercially available from CG-TEC and has a fiber volume fraction of 63% according to manufacturer.

Measured  $S$ -parameters are depicted in Figure 13. Return loss is better than 10 dB between 2 GHz and 10 GHz for all ground plane materials. The return loss with the UD-CFRP is a bit reduced but still better than 10 dB.

Gain patterns are again measured in the institute's anechoic chamber (Figure 14). Gain patterns presented in this section are not normalized and are given according to the IEEE gain definition based on accepted power, in order to emphasize the large influence of UD-CFRP in comparison to the shred-CFRP and twill-CFRP. Vertical cuts of the measured gain patterns are depicted in Figure 15. Cuts for azimuthal angle  $\varphi = 0^\circ$  and  $\varphi = 90^\circ$  are shown on the left and right side, respectively. For the UD-CFRP  $\varphi = 0^\circ$

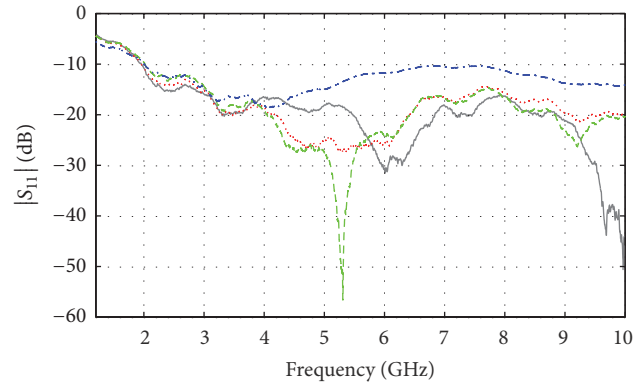


FIGURE 13: Measured  $S$ -parameters of the conical monopole antenna on different ground plane materials (reprinted with permission from [35]; ©2017 IEEE).

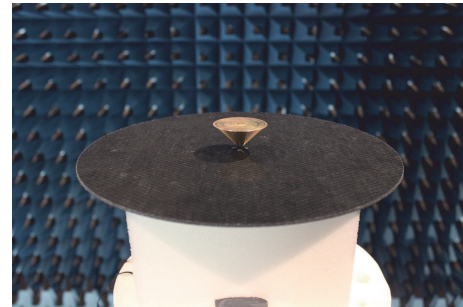


FIGURE 14: Conical monopole antenna on the shred-CFRP ground plane. The antenna is placed on a Rohacell column on an azimuth rotary stage inside the university's anechoic chamber.

corresponds with fiber direction and  $\varphi = 90^\circ$  is perpendicular to fiber direction. The CFRP with fiber shreds and the twill-weave CFRP perform similar to aluminum in the whole frequency range. With the UD-CFRP antenna gain in fiber direction ( $\varphi = 0^\circ$ ) is 1–4 dB lower than on aluminum. The shape of the gain pattern in fiber direction remains widely unchanged, but radiation perpendicular to fiber direction is greatly diminished for the UD-CFRP and the gain pattern is changed, especially for radiation in the horizontal plane  $\theta \approx 90^\circ$ . For the conical monopole antenna radiation efficiency on shred-CFRP is measured close to that of aluminum in the frequency range from 1 GHz to 10 GHz, about 0.5 dB lower at 5.9 GHz [35].

The measurements show that using a UD-CFRP has a huge influence on antennas. The anisotropic conductivity of UD-CFRP obstructs surface currents on the ground plane leading to reduced gain and changed radiation pattern perpendicular to fiber direction. Although the anisotropy may be useful [25], a good isotropic conductor is most desirable as antenna ground plane material. This issue is crucial in the automotive industry, where DSRC was recently introduced for safety relevant vehicle-to-vehicle communication. For

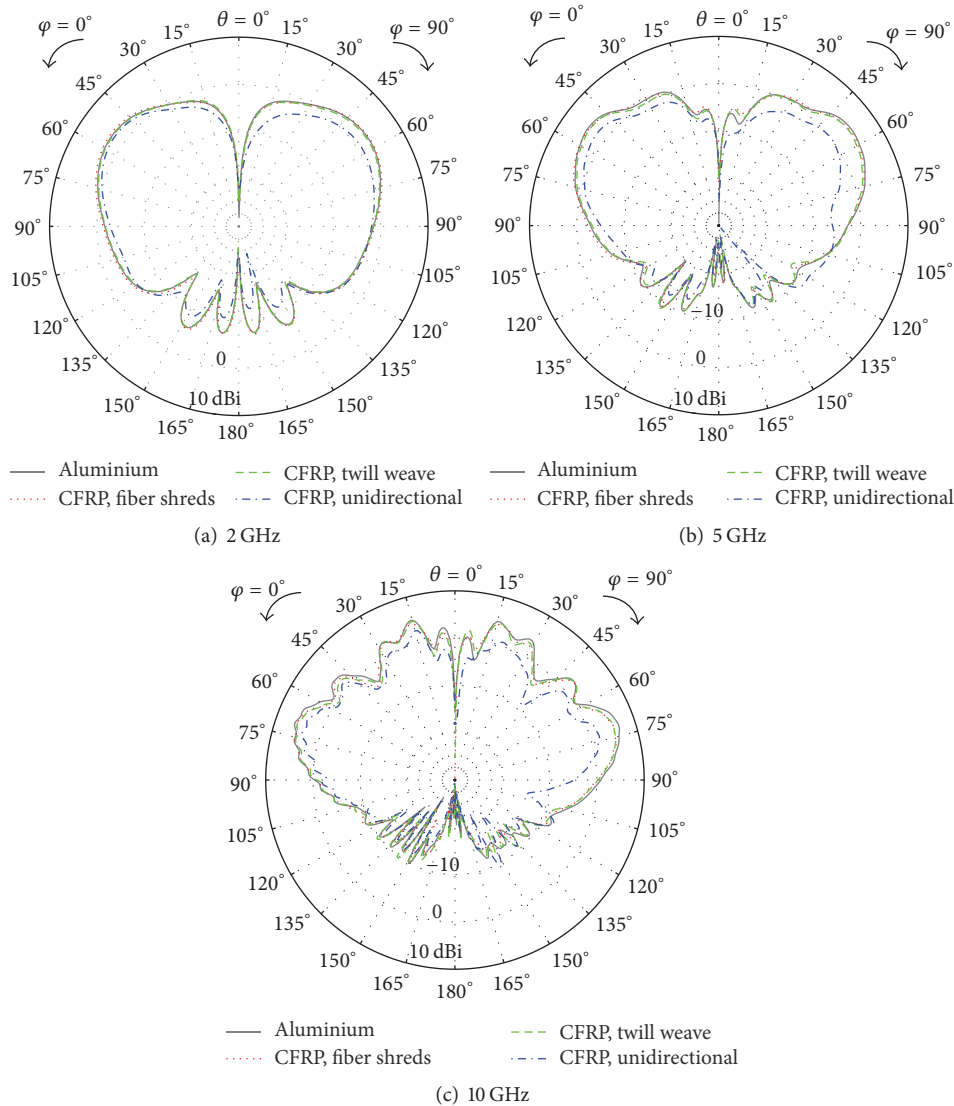


FIGURE 15: Vertical cuts of the gain patterns. Cuts for azimuthal angle  $\varphi = 0^\circ$  and  $\varphi = 90^\circ$  are shown on the left and right side, respectively (reprinted with permission from [35]; ©2017 IEEE).

electric car construction with a lightweight CFRP chassis, the materials should be chosen such that they do not impair antenna performance. The presented measurements show that this is achievable by placing either randomly oriented fiber shreds or woven fibers on top of any CFRP laminate. The electric currents are confined to the top most layer of the composite due to the skin effect. It is therefore feasible to only manufacture the top CFRP layer according to antenna considerations, whereas the remaining plies are designed to meet the mechanical requirements.

The antenna performance differences between shred-CFRP, twill-CFRP, and aluminium in the investigated frequency range are negligible in most antenna applications. The conductivity of the CFRP with the shredded fibers seems to be even somewhat more isotropic than the conductivity of the twill-CFRP. Using recycled and shredded carbon fibers is desirable from an antenna viewpoint.

## 5. Conclusion

Quasi-isotropic CFRP with shredded carbon fibers in random alignment on the top layer are proposed for antenna applications. A CFRP laminate with carbon fiber shreds on top, but unidirectional fibers in the remaining plies, was manufactured. Carbon fiber shreds can be sourced from recycled CFRP, resulting in a sustainable product design.

Material measurements with the Nicolson-Ross-Weir (NRW) method show that the radio-frequency properties of the proposed CFRP are close to isotropic in comparison to unidirectional and woven CFRP. The variations in measured material parameters can be explained by inhomogeneity in the medium, rather than anisotropy.

Measurements of monopole antennas on the shredded-fiber CFRP show no influence on the antenna's gain pattern. Radiation efficiency of a conical monopole antenna on a

ground plane made from the proposed CFRP is close to 100%.

When being utilized as a ground plane material for antennas for IEEE 802.11p at 5.9 GHz, the shredded-fiber CFRP can be modeled as an isotropic material.

## Disclosure

The current address of P. K. Gentner is Kathrein.

## Conflicts of Interest

The authors declare that there are no conflicts of interest regarding the publication of this paper.

## Acknowledgments

This work has been funded by the Christian Doppler Laboratory for Wireless Technologies for Sustainable Mobility. The financial support by the Federal Ministry of Economy, Family and Youth and the National Foundation for Research, Technology and Development is gratefully acknowledged. The authors acknowledge the TU Wien University Library for financial support through its Open Access Funding Program.

## References

- [1] S. Rea, D. Linton, E. Orr, and J. McConnell, "Electromagnetic shielding properties of carbon fibre composites in avionic systems," *Microwave Review*, pp. 29–32, 2005.
- [2] D. Micheli, S. Laurenzi, V. M. Primiani, F. Moglie, G. Gradoni, and M. Marchetti, "Electromagnetic shielding of oriented carbon fiber composite materials," in *Proceedings of the ESA Workshop on Aerospace EMC*, pp. 1–5, 2012.
- [3] M. D. Belrhiti, S. Bri, A. Nakheli, and A. Mamouni, "Dielectric properties by rectangular waveguide," *International Journal of Emerging Sciences*, vol. 3, no. 2, pp. 163–171, June 2013.
- [4] W. van Rossum, F. Nennie, D. Deiana, A. J. van der Veen, and S. Monni, "Dielectric characterisation of human tissue samples," in *Proceedings of the 8th European Conference on Antennas and Propagation, EuCAP 2014*, pp. 594–598, April 2014.
- [5] K. C. Yaw, "Measurement of dielectric material properties application note products," *Application Note Rhode and Schwarz*, 36 pages, 2012.
- [6] H. C. Kim and S. K. See, "Electrical properties of unidirectional carbon-epoxy composites in wide frequency band," *Journal of Physics D: Applied Physics*, vol. 23, no. 7, 1990.
- [7] T. A. Ezquerro, M. T. Connor, S. Roy, M. Kuleszcza, J. Fernandes-Nascimento, and F. J. Baltá-Calleja, "Alternating-current electrical properties of graphite, carbon-black and carbon-fiber polymeric composites," *Composites Science and Technology*, vol. 61, no. 6, pp. 903–909, 2001.
- [8] A. Galehdar and K. Nicholson, "The conductivity of unidirectional and quasi isotropic carbon fiber composites," in *Proceeding of the 40th European Microwave Conference*, pp. 882–885, September 2010.
- [9] A. Galehdar, W. S. T. Rowe, K. Ghorbani, P. J. Callus, S. John, and C. H. Wang, "The effect of ply orientation on the performance of antennas in or on carbon fiber composites," *Progress in Electromagnetics Research*, vol. 116, pp. 123–136, 2011.
- [10] A. Galehdar, K. J. Nicholson, P. J. Callus et al., "The strong diamagnetic behaviour of unidirectional carbon fiber reinforced polymer laminates," *Journal of Applied Physics*, vol. 112, no. 11, Article ID 113921, 2012.
- [11] C. L. Holloway, S. Member, M. S. Sarto, and M. Johansson, "Analyzing carbon-fiber composite materials with equivalent-layer models," *IEEE Transactions on Electromagnetic Compatibility*, vol. 47, no. 4, pp. 833–844, 2005.
- [12] G. Wasselynck, D. Trichet, B. Ramdane, and J. Fouldagar, "Interaction between electromagnetic field and CFRP materials: a new multiscale homogenization approach," *IEEE Transactions on Magnetics*, vol. 46, no. 8, pp. 3277–3280, 2010.
- [13] S.-E. Lee, K.-S. Oh, and C.-G. Kim, "Electromagnetic characteristics of frequency selective fabric composites," *Electronics Letters*, vol. 42, no. 8, pp. 12–13, 2006.
- [14] R. R. De Assis and I. Bianchi, "Analysis of microstrip antennas on carbon fiber composite material," *Journal of Microwaves, Optoelectronics and Electromagnetic Applications*, vol. 11, no. 1, pp. 154–161, 2012.
- [15] A. Mehdipour, C. W. Trueman, A. R. Sebak, and S. V. Hoa, "Carbon-fiber composite T-match folded bow-tie antenna for RFID applications," in *Proceedings of the IEEE International Symposium on Antennas and Propagation and USNC/URSI National Radio Science Meeting, APSURSI 2009*, June 2009.
- [16] A. Mehdipour, A. R. Sebak, C. W. Trueman, I. D. Rosca, and S. V. Hoa, "Advanced conductive carbon fiber composite materials for antenna and microwave applications," in *Proceedings of the Joint IEEE International Symposium on Antennas and Propagation and USNC-URSI National Radio Science Meeting (APSURSI '12)*, July 2012.
- [17] A. Mehdipour, A. R. Sebak, C. W. Trueman, I. D. Rosca, and S. V. Hoa, "Conductive carbon fiber composite materials for antenna and microwave applications," in *Proceedings of the 29th National Radio Science Conference (NRSC '12)*, pp. 1–8, April 2012.
- [18] D. Gray, K. Nicholson, K. Ghorbani, and P. Callus, "Carbon fibre reinforced plastic slotted waveguide antenna," in *Proceedings of the Asia-Pacific Microwave conference, APMC 2010*, pp. 307–310, December 2010.
- [19] K. J. Nicholson, W. S. T. Rowe, P. J. Callus, and K. Ghorbani, "Split-ring resonator loading for the slotted waveguide antenna stiffened structure," *IEEE Antennas and Wireless Propagation Letters*, vol. 10, pp. 1524–1527, 2011.
- [20] K. J. Nicholson, W. S. T. Rowe, P. J. Callus, K. Ghorbani, and T. Itoh, "Coaxial right/left-handed transmission line for electronic beam steering in the slotted waveguide antenna stiffened structure," *IEEE Transactions on Microwave Theory and Techniques*, vol. 62, no. 4, pp. 773–778, 2014.
- [21] G. Lacy, "Development of a 15 metre diameter high performance, low cost radio antenna for the square kilometre array," in *Proceedings of the 20th International Conference on Composite Materials*, pp. 1–9, July 2015.
- [22] K. M. Keen, "Gain-Loss Measurements on a Carbon-Fibre Composite Reflector Antenna," *Electronics Letters*, vol. 11, no. 11, pp. 234–235, 1975.
- [23] S. Futatsumori, K. Morioka, A. Kohmura, M. Shioji, and N. Yonemoto, "Fundamental applicability evaluation of carbon fiber reinforced plastic materials utilized in millimeter-wave antennas," in *Proceedings of the IEEE Conference on Antenna Measurements and Applications, CAMA 2014*, pp. 1–2, 2014.
- [24] G. Ghione and M. Orefice, "Inter-modulation products generation from carbon fibre reflector antennas," in *Proceedings of the*

- Antennas and Propagation Society International Symposium*, vol. 23, pp. 153–156, June 1985.
- [25] A. Mehdipour, T. A. Denidni, C. W. Trueman et al., “Mechanically reconfigurable antennas using an anisotropic carbon-fibre composite ground,” *IET Microwaves, Antennas & Propagation*, vol. 7, no. 13, pp. 1055–1063, 2013.
- [26] G. Artner and R. Langwieser, “Performance of an automotive antenna module on a carbon-fiber composite car roof,” in *Proceedings of the 10th European Conference on Antennas and Propagation, EuCAP 2016*, April 2016.
- [27] G. Artner, R. Langwieser, R. Zemann, and C. F. Mecklenbräuker, “Carbon fiber reinforced polymer integrated antenna module,” in *Proceedings of the 2016 IEEE-APS topical conference on antennas and propagation in wireless communications (APWC '16)*, pp. 59–62, September 2016.
- [28] G. Artner, R. Langwieser, and C. F. Mecklenbräuker, “Concealed CFRP vehicle chassis antenna cavity,” *IEEE Antennas and Wireless Propagation Letters*, 2016.
- [29] F. Teodorescu, H. Teodorescu, G. Stanca, D. Condurache, and R. S. Craciunoiu, “On the recycling of carbon fibers reinforced polymer matrix composites,” in *Proceedings of the 4th IASME/WSEAS International Conference on Energy, Environment, Ecosystems and Sustainable Development, EEESD 2008*, pp. 294–297, June 2008.
- [30] A. M. Nicolson and G. F. Ross, “Measurement of the intrinsic properties of materials by time-domain techniques,” *IEEE Transactions on Instrumentation and Measurement*, vol. 19, no. 4, pp. 377–382, 1970.
- [31] W. B. Weir, “Automatic measurement of complex dielectric constant and permeability at microwave frequencies,” *Proceedings of the IEEE*, vol. 62, no. 1, pp. 33–36, January 1974.
- [32] A. N. Vicente, G. M. Dip, and C. Junqueira, “The step by step development of NRW method,” in *SBMO/IEEE MTT-S International Microwave and Optoelectronics Conference, IMOC 2011*, pp. 738–742, November 2011.
- [33] C. A. Balanis and D. DeCarlo, “Monopole antenna patterns on finite size composite ground planes,” *IEEE Transactions on Antennas and Propagation*, vol. 30, no. 4, pp. 764–768, 1982.
- [34] G. Artner, R. Langwieser, G. Lasser, and C. F. Mecklenbräuker, “Effect of carbon-fiber composites as ground plane material on antenna performance,” in *IEEE-APS Topical Conference on Antennas and Propagation in Wireless Communications, APWC 2014*, pp. 711–714, August 2014.
- [35] G. Artner, R. Langwieser, and C. F. Mecklenbräuker, “Carbon fiber reinforced polymer as antenna ground plane material up to 10 GHz,” in *Proceedings of the European Conference on Antennas and Propagation, EuCAP 2017*, pp. 1–5, March 2017.

## Research Article

# Topological Design of Planar Circularly Polarized Directional Antenna with Low Profile Using Particle Swarm Optimization

Xiaonan Zhao,<sup>1,2</sup> Junping Geng,<sup>1</sup> Ronghong Jin,<sup>1</sup> Yao Jin,<sup>1</sup> Xiang Liu,<sup>1</sup> and Wenyan Yin<sup>1</sup>

<sup>1</sup>Department of Electronics Engineering, Shanghai Jiao Tong University, Shanghai 200240, China

<sup>2</sup>China Ship Development and Design Center, Wuhan, China

Correspondence should be addressed to Xiaonan Zhao; [sherlock\\_zxn@hotmail.com](mailto:sherlock_zxn@hotmail.com)

Received 29 January 2017; Accepted 11 April 2017; Published 17 May 2017

Academic Editor: Davide Ramaccia

Copyright © 2017 Xiaonan Zhao et al. This is an open access article distributed under the Creative Commons Attribution License, which permits unrestricted use, distribution, and reproduction in any medium, provided the original work is properly cited.

A topological method for the design and optimization of planar circularly polarized (CP) directional antenna with low profile was presented. By inserting two parasitic layers, generated by particle swarm optimization, between the equiangular spiral antenna and the ground, a low-profile wideband CP antenna with directional radiation pattern and high gain is achieved. The optimized antenna shows an impedance matching band ( $|S_{11}| < -10$  dB) of 4–12 GHz with a whole-band stable directional pattern in 4–11.5 GHz, and the antenna gain peak is 8 dBi, which work well in the available band. Measured return loss, antenna gain, and far field patterns agree well with simulation results.

## 1. Introduction

Planar circularly polarized (CP) antennas are widely used in modern wireless communications owing to their compact sizes [1, 2] that can be flexibly integrated with various systems. For achieving good directionality and high gain, a ground plane is often used at  $1/4$  wavelength away from the planar antenna as a reflector [3], which results in the deterioration of the frequency bandwidths of planar antennas and limits their scope of applications. At the motivations of increasing demands for different characteristics including high gain, wide impedance band, and low fabrication cost, many smart improvements are made based on original planar antennas [4]. For examples, photonic bandgap (PBG) [5] or electromagnetic band gap (EBG) structures [6] can be used for reducing the profiles of spiral antennas. A UWB spiral antenna with parabolic reflector was designed in [7], where  $VSWR < 2$  was achieved in a wide band from 0.94 GHz to 4.27 GHz. A small disc backed by a cavity [8] was introduced under a single-arm spiral antenna and the periphery of the cavity was loaded using ring-shaped absorbing material to realize an extremely low-profile wideband CP directional antenna. Corrugated reflectors are adopted to keep the ultra-wideband characteristic with a stable radiation pattern [9].

In [10], an irregular ground plane consisting of a circular part and several extended curved branches is proposed for a circular patch; the antenna and the irregular ground plane are shortened by a set of conductive vias to achieve wideband impedance matching.

These ingenious designs rely much on designers' skill and experience. To offer an easy method for designing and optimizing low-profile CP directional antennas, we proposed a universal scheme along with a discrete meshing optimization method to generate two optimized 2D parasitic layers, which acts as a metamaterial between the existed equiangular spiral antenna and the ground plane to achieve good radiation performance.

## 2. Semiautomatic Optimization Method

Inspired by the principle of metamaterial, which owns smart properties capable of blocking, absorbing, enhancing, or bending electromagnetic waves, we tried to find a common way to generate a metamaterial structure automatically for the optimization of planar antennas.

Firstly, the optimized antenna includes multitargets, such as lower profile, better CP characteristic, higher gain, and

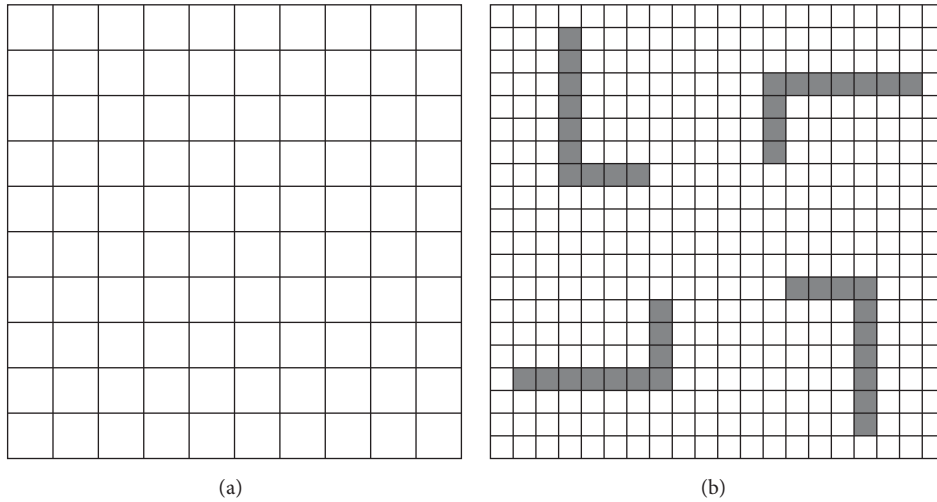


FIGURE 1: (a) Discrete grid model and (b) the rotational symmetrical layer.

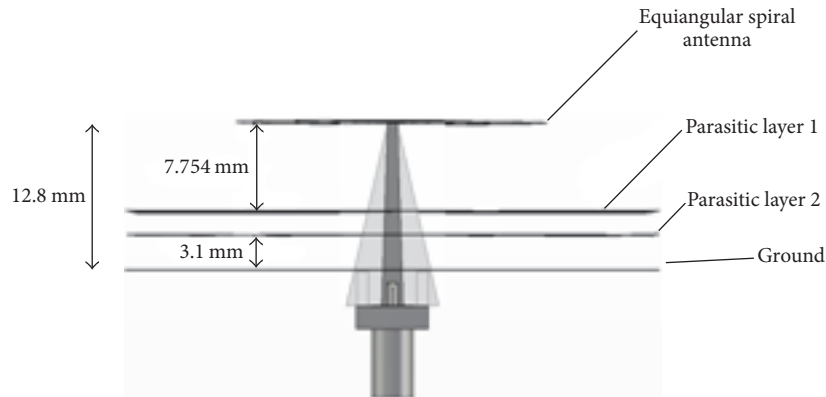


FIGURE 2: Side view of the basic scheme.

wider frequency band, so that a thin (for low profile) rotational symmetrical structure (for CP beam) with reflectance bigger than 0 (for high gain in wideband) is set as the design direction. We proposed a rotational symmetrical grid parasitic layer between the planar antenna and its ground as a preliminary plan. To make it easier to get good “metamaterial” characteristic, we took two parallel layers with different discrete grid pattern and named them parasitic layers. Each parasitic layer is equally divided into four parts, and one of them is meshed. The mesh should not be too coarse, which would make it hard for optimization, and should not be too refined, which would not be convenient for fabrication. Refer to the mesh size in computational electromagnetics (CEM) which is always set as one-tenth of the wavelength; we mesh each parasitic layer’s first quarter part into  $10 \times 10$  grids, as shown in Figure 1(a). The remaining three quarter parts are rotational symmetrical to the first one with 90-degree angle difference, as shown in Figure 1(b).

Optimization algorithm is used to determine whether each grid of the 1/4 part is to be filled with metal sheet or left empty, while the rest three quarter parts are rotational

symmetrical same counter parts of the first quarter part. Thus the energy would be assembled to the center, which is somewhat like bending electromagnetic waves. Both parasitic layers are designed in this way.

In order to prove parasitic layers’ effect as a metamaterial and their efficiency in antenna improvement, we took an example.

### 3. Example of an Equiangular Spiral Antenna

*3.1. Optimized Antenna.* We take an equiangular spiral antenna as an example to make this process more detailed. The initial structure of the antenna structure is suggested in [11]. A microstrip-to-balanced stripline balun [4] is used as the feeding, which is shown in Figure 2. Then the two rectangle parasitic layers with same size as the antenna’s ground are introduced. Both of them have a circular hole in the center for the feeding.

There are many optimization algorithms commonly used in electromagnetics including antenna design, such as genetic

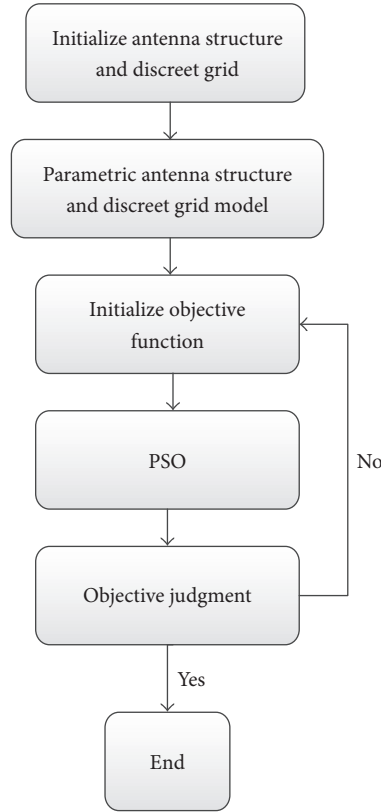


FIGURE 3: Antenna optimization process.

algorithm [12, 13], particle swarm optimization (PSO) [14–17], and more recent biogeography-based optimization [18, 19].

Here, we choose PSO as the optimization algorithm. The antenna optimization process is shown in Figure 3.

For the antenna structure, the optimization is based on continuous variables. For the parasitic layers with grid structure, optimization concerns discrete variable, which has only two values, denoted with or without grid. In order to unify the discrete and continuous variables into the same particle swarm optimization (PSO) and single fitness function, we used an improved mixed-integer multiobjective PSO. By consulting [10], PSO was edited by Visual Basic and then added to CST Microwave Studio through the macro. The detailed process is as follows. Different from [13], we define the grid element code height  $i(j, k) = 0.9 \sim 1.1$ , where “ $\text{int}(i(j, k)) = 1$ ” represents the grid with metal if  $i(j, k) \geq 1$  and “ $\text{int}(i(j, k)) = 0$ ” represents the grid without metal if  $i(j, k) < 1$ . The code height is similar to the length parameter of every grid and can be regarded as particles similar to other parameters in the PSO model in CST or any other commercial EM software.

The optimized targets (OT) include  $|S_{11}|$ , wideband (wb), directivity, and gain ( $G$ ) in the available band, and the target function can be described as

$$\text{OT} = w_1 \times |S_{11}| + \frac{w_2}{\text{wb}} + \frac{w_3}{G(\theta < 30^\circ)}. \quad (1)$$

Here,  $w_1$ ,  $w_2$ , and  $w_3$  are the weights of the targets and  $G(\theta < 30^\circ)$  is the combined target of directivity and gain, which means the gain when the main beam of the antenna is in  $\theta < 30^\circ$ . Usually, we set  $w_1 = w_2 = w_3 = 1.0$ , which can be adjusted after the crude good results appeared.

With the above optimization process, the parameters of the equiangular spiral antenna structure and the parasitic layers can be optimized at the same time.

After optimization, the top layer is an equiangular spiral antenna as shown in Figure 4(a) and the two parasitic layers are shown in Figures 4(b) and 4(c), respectively.

With  $H = 12.8$  mm,  $L = 44.2$  mm, and the maximum radius of the equiangular spiral antenna, 13.75 mm, this semiautomatic designed antenna has a low-profile structure, which is suitable to be installed on plane platform.

**3.2. Transmission and Reflection Performance of the Optimized Parasitic Layers.** In order to verify the “metamaterial” characteristic of the optimized parasitic layers in concerned frequencies, we simulated the transmission and reflection performance from 3 GHz to 12 GHz.

Here, two cases are set for simulation. In Case 1, the CP plane wave just radiated to the ground, as shown in Figure 5(a). Reflected wave power flow density at the parallel probe plane A-A (which is  $\lambda/2$  above the ground) and transmitted wave power flow density at the parallel probe

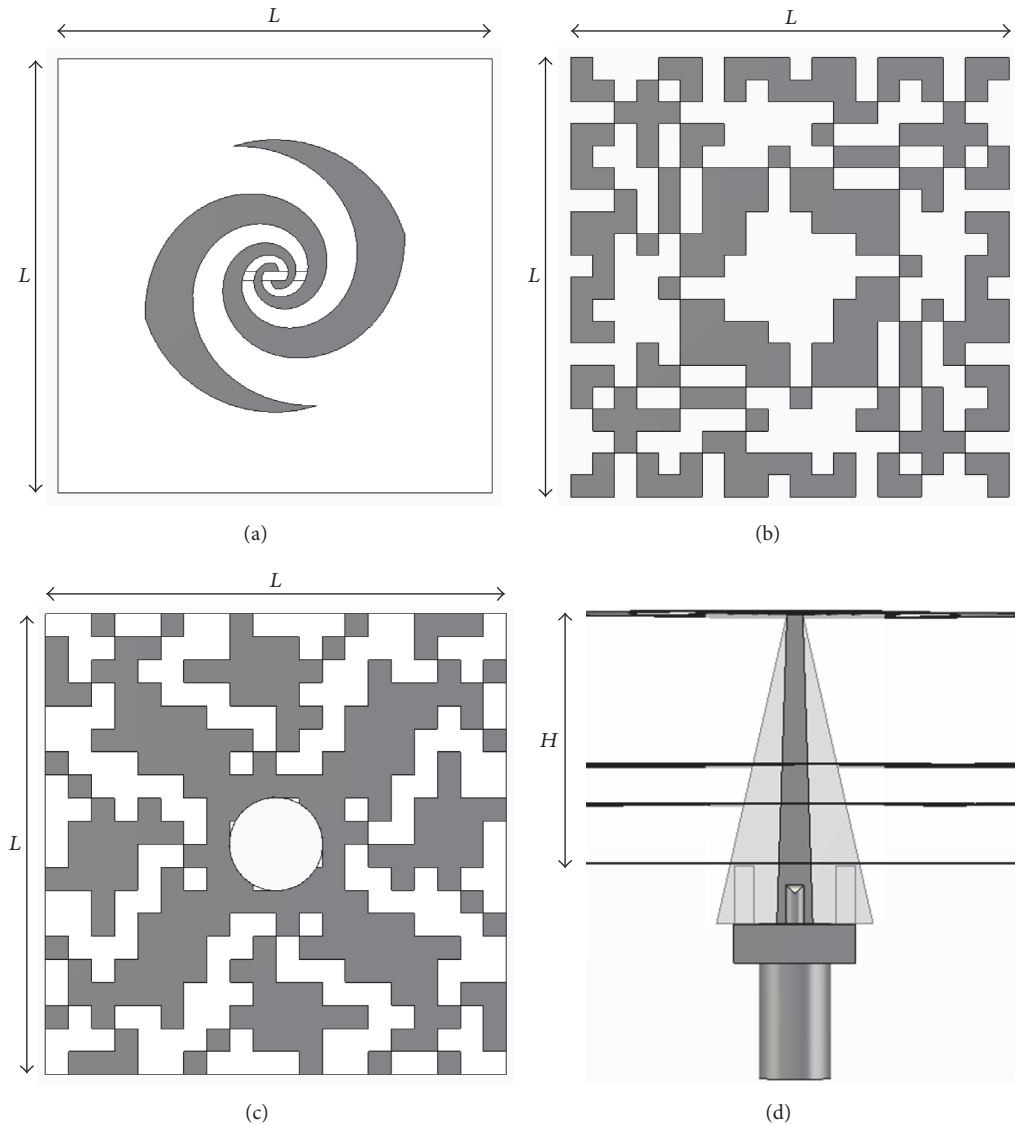


FIGURE 4: Antenna structure: (a) equiangular spiral antenna, (b) parasitic layer 1, (c) parasitic layer 2, and (d) side view and balun.

plane B-B (which is  $\lambda/2$  below the ground) are simulated; results at typical frequencies are shown in Figure 5.

In Figure 5(b), the reflected power flow density distribution is very close to the transmitted power flow at low frequencies and becomes larger than the transmitted power flow at higher frequencies. But the reflected power flow density distribution is very different from the transmitted power flow.

In Case 2, the CP plane wave radiates through the two optimized parasitic layers with ground, as shown in Figure 6(a). For the same samples,  $f = 4$  GHz, 6 GHz, and 8 GHz; the reflected power flow density is much more stronger than that in Case 1. It is obvious that adding the parasitic layers would strengthen and homogenize the reflected wave power flow density and meanwhile reduce the transmitted wave power flow density.

Further, we discretized the same-sized probe plane into  $40 \times 40$  grids. The total reflected or transmitted wave power is calculated in Table 1. The data shows that inserting the two parasitic layers could transfer the fixed narrow-band ground with  $-1$  reflection into a wideband “metamaterial” structure with positive reflection.

Graphical comparisons are shown in Figures 7 and 8. In Figure 7, the upper parasitic layer shows stronger reflected wave power in low frequency band than the lower parasitic layer and the same in the middle band but smaller in the higher band, so that the total reflected power from the two parasitic layers keeps stronger in 4 GHz~9 GHz.

In Figure 8, the upper parasitic layer transmitted less power in lower frequency band but increased quickly in higher band. The lower parasitic layer transmitted small power and equilibrium in the whole band, so that the total

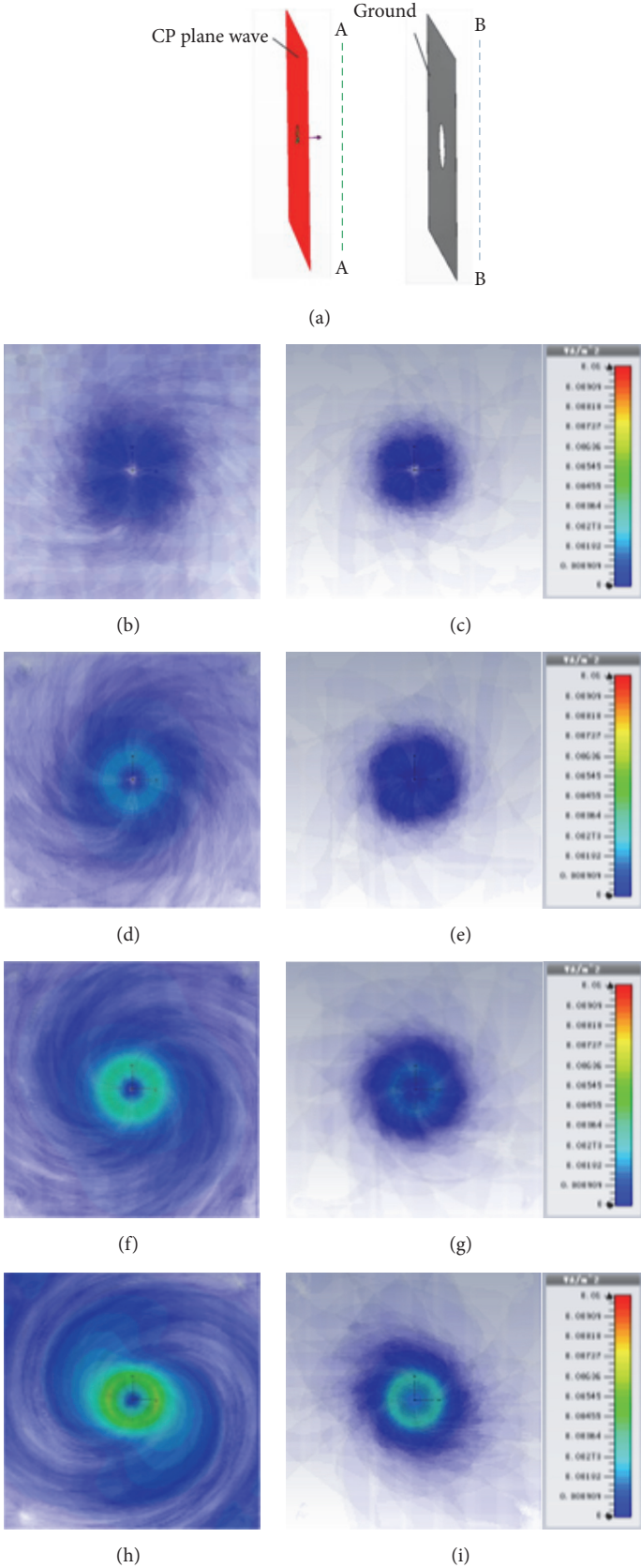


FIGURE 5: Case 1: (a) circularly polarized plane wave radiates on the limited ground. Simulated reflected wave power flow density at (b) 4 GHz, (d) 6 GHz, (f) 8 GHz, and (h) 10 GHz. Simulated transmitted wave power flow density at (c) 4 GHz, (e) 6 GHz, (g) 8 GHz, and (i) 10 GHz.

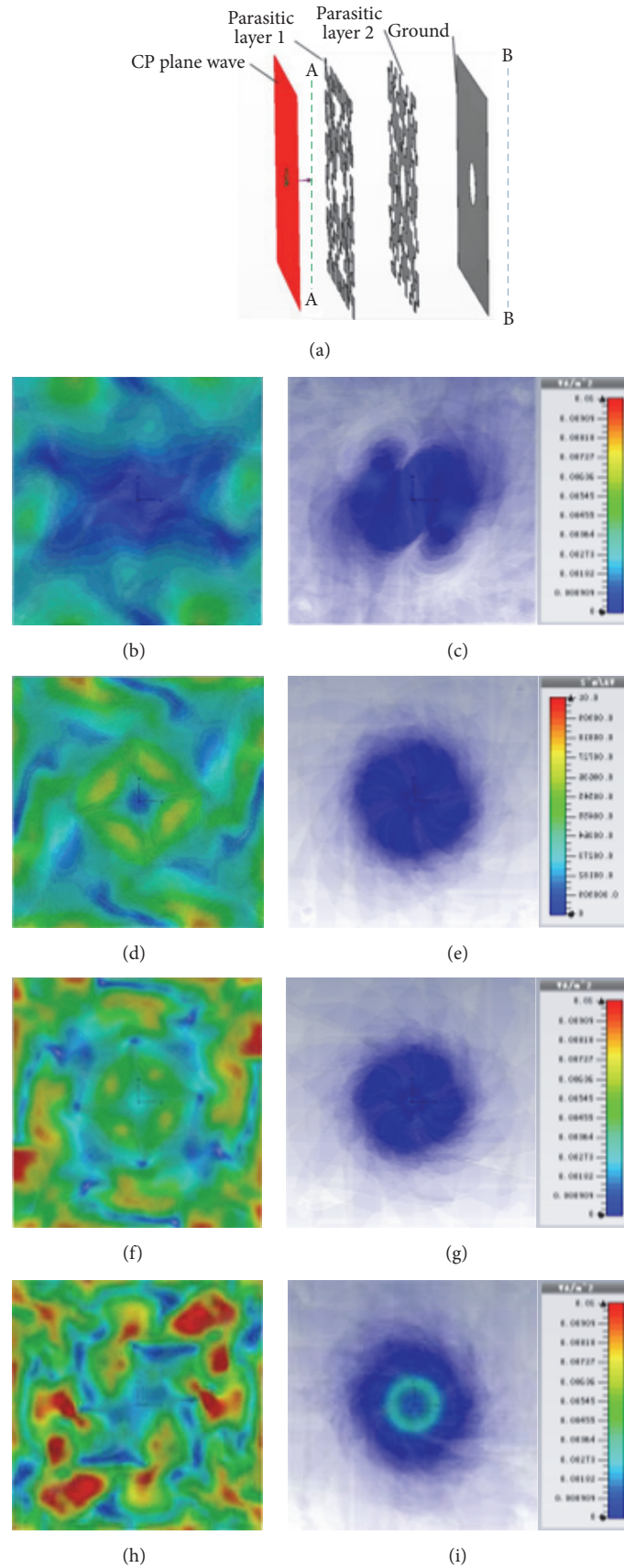


FIGURE 6: Case 2: (a) circularly polarized plane wave radiates on the limited ground. Simulated reflected wave power flow density at (b) 4 GHz, (d) 6 GHz, (f) 8 GHz, and (h) 10 GHz. Simulated transmitted wave power flow density at (c) 4 GHz, (e) 6 GHz, (g) 8 GHz, and (i) 10 GHz.

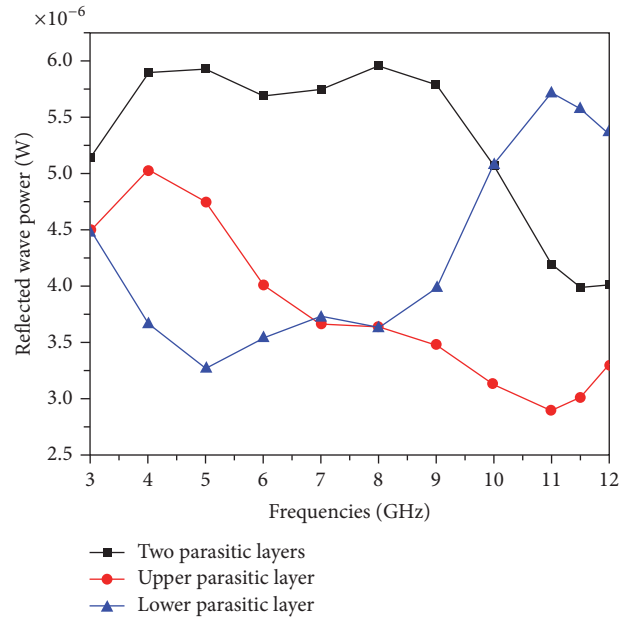


FIGURE 7: Total reflected wave power flow for parasitic layers alone and together.

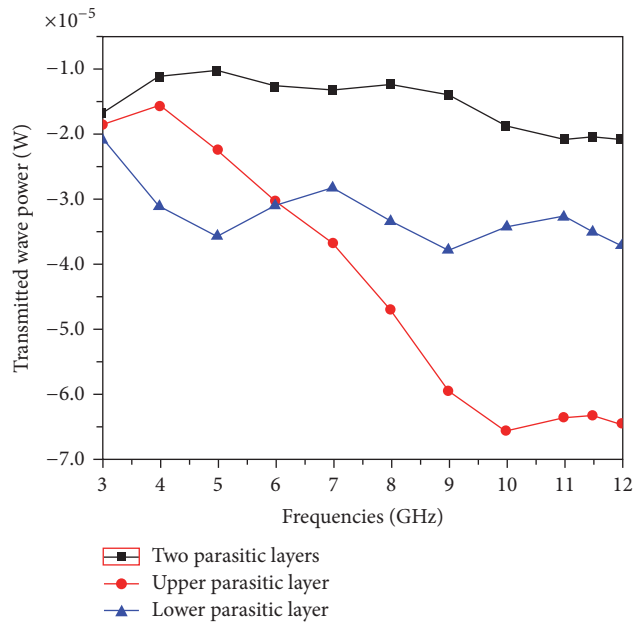


FIGURE 8: Total transmitted wave power flow for parasitic layers alone and together.

transmitted power from these two parasitic layers is very small.

Figures 7 and 8 clearly reveal the frequency selective characteristics of single quasi-periodic parasitic layer in reflection and transmission.

So, combining the two parasitic layers and ground, just as in Figure 5(a), the incident plane wave in lower frequency firstly is reflected by the upper parasitic layer, and the higher frequency band wave is mainly transmitted to the lower parasitic layer and then reflected. Only few left waves reach

the ground and would be reflected back to the parasitic layer again.

It is clear that the combination of the different frequency selective parasitic layers and the ground would reflect the wave back in very wide band.

#### 4. Results Analysis

We marked the equiangular spiral antenna with ground only as Ant1, in which the distance between equiangular spiral

TABLE 1: Total reflected and transmitted wave power flow for different structure (normalization value).

Analyzed structures	Component	Frequencies (GHz)										
		3	4	5	6	7	8	9	10	11	11.5	12
None	Trans	1	1	1	1	1	1	1	1	1	1	1
	Ref	0	0	0	0	0	0	0	0	0	0	0
Case 1	Trans	0	0	0	0	0	0	0.01	0.01	0.02	0.02	0.02
	Ref	-1	-1	-1	-1	-1	-1	-1	-1	-1	-1	-1
Case 2	Trans	0	0	0	0	0	0	0	0	0	0	0
	Ref	0.95	0.87	0.80	0.68	0.62	0.62	0.56	0.52	0.44	0.38	0.38

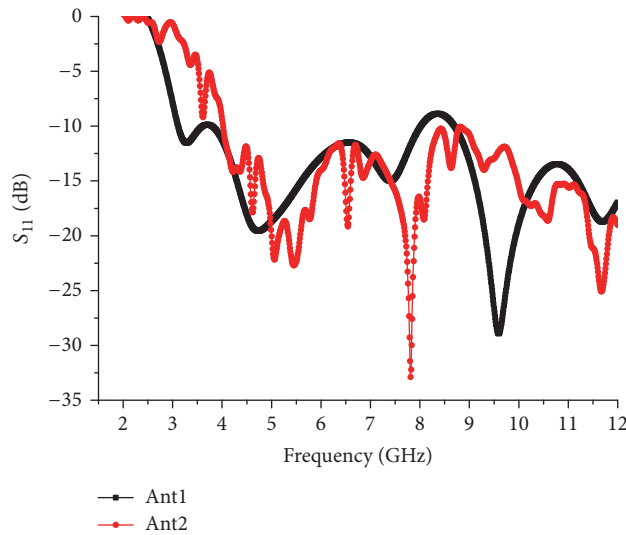


FIGURE 9: Return loss for Ant1 and Ant2.

antenna and ground is fixed, and the bandwidth with stable directional radiation is limited. The optimized antenna is marked as Ant2 for comparison.

**4.1. Simulation Results.** After optimization, simulated  $S_{11}$  of the two antennas is shown in Figure 9. The impedance bandwidth of Ant1 covers from 3 GHz to 8 GHz for  $|S_{11}| < -10$  dB, while the impedance bandwidth of Ant2 covers from 4 GHz to 9 GHz.

By adding the optimized parasitic layers, the far field pattern becomes more stable. Wideband and high gain are achieved simultaneously as the results shown in Figures 10 and 11.

The far field patterns of the two antennas are shown in Figure 10. For Ant1 without the parasitic layers, the distance from the equiangular spiral antenna to the ground is fixed, which makes the far field confusion at higher frequency, and the pattern splitted at 8 GHz. After the two parasitic layers are inserted, the “metamaterial effect” makes the max. directivity of Ant2 on different frequencies stay at the same azimuth angle; it could be said that the far field patterns of Ant2 are more stably directional compared to Ant1 from 4 GHz to 11 GHz.

The simulated gains of Ant1 and Ant2 are shown in Figure 11. From 4 GHz to 10 GHz, the gain of Ant2 is almost higher than that of Ant1.

**4.2. Measurement Result.** The real Ant2 is fabricated, which is 12.8 mm × 44.2 mm × 44.2 mm, as shown in Figure 12. The reflection coefficient of the fabricated antenna is shown in Figure 13. The measured impedance matching band is from 4 GHz to 12 GHz, which is similar to the simulation result.

In Figure 14, the measured far field patterns of Ant2 are shown at different frequencies. The measured results are similar to the simulated ones in Figure 10(b). It also shows that the far field patterns of Ant2 are stably directional.

In Figure 15, the simulated and measured gains of Ant2 are shown, which work well in most available band. The measured gain peak is about 8 dBi.

As we focus on the low-profile and directional characteristics of the antenna, which was realized by adding the metamaterial parasitic layers, and the prototype antenna is a spiral antenna, the axial ratio is not the characteristic of interest in this paper. Smaller beamwidth is another important advantage of CP antenna compared with linear

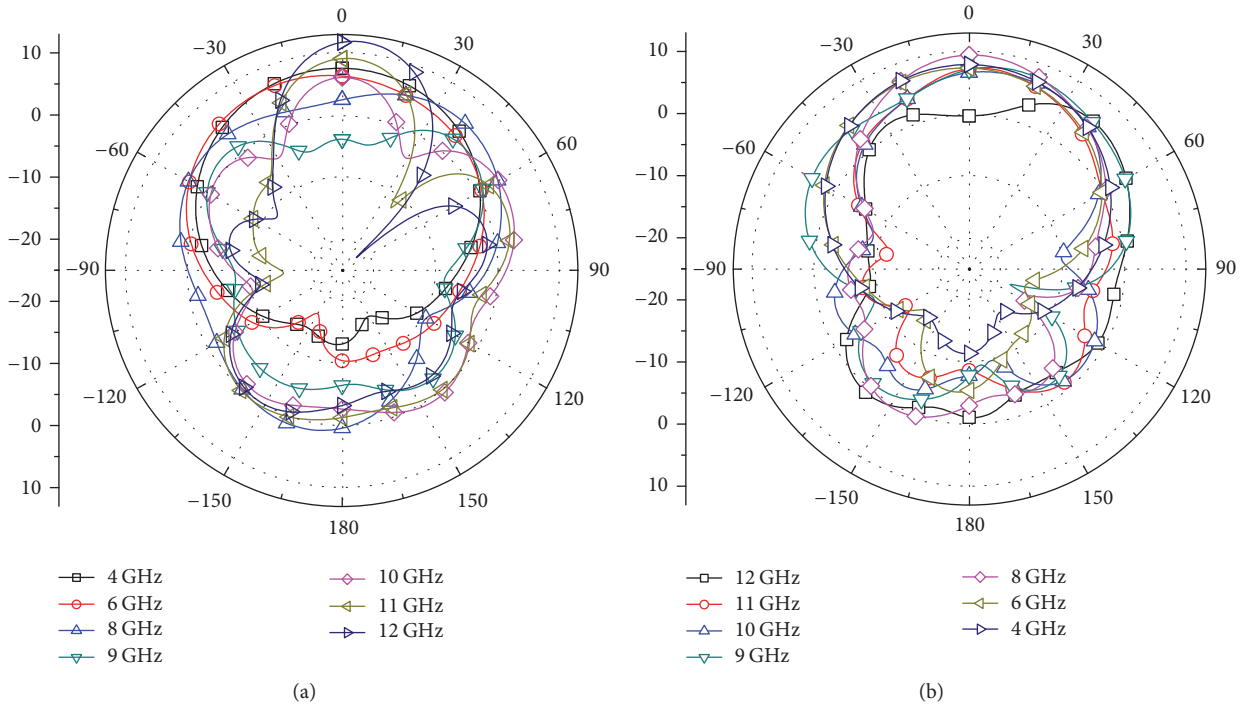


FIGURE 10: Far field pattern of (a) Ant1 and (b) Ant2.

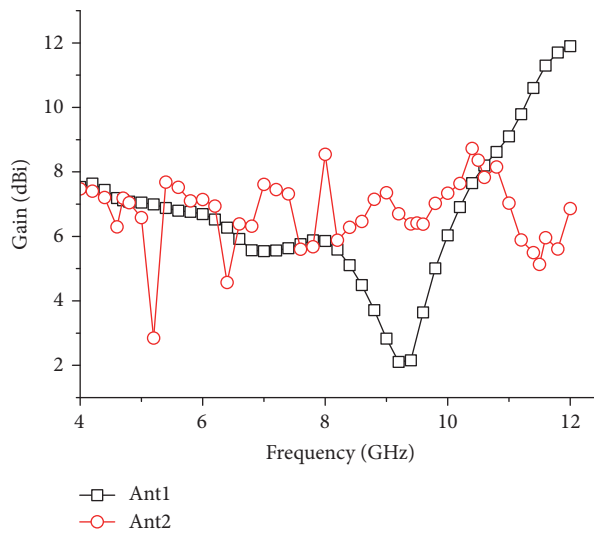


FIGURE 11: Simulated gain of Ant1 and Ant2.

polarized antenna, so the stability of the far field patterns in wideband receives more concern in this paper.

### 5. Conclusion

In this paper, we have presented a topological method for the design and optimization of planar CP directional antennas with metamaterial parasitic layers. Particle swarm optimization is employed for generating metamaterial parasitic layers. By inserting such metamaterial layers, a low-profile wideband

CP antenna with directional radiation pattern and high gain was designed, fabricated, and characterized. The optimized antenna has an impedance matching band ( $|S_{11}| < -10$  dB) of 4–12 GHz with a whole-band stably directional pattern in 4–11.5 GHz, and the antenna gain peak is 8 dBi, which work well in most available band. The proposed method offers code-based self-generation of metamaterial parasitic layers, which requires less designer’s skill/experience and is very suitable for improving various kinds of plane antennas with any reasonable targets.

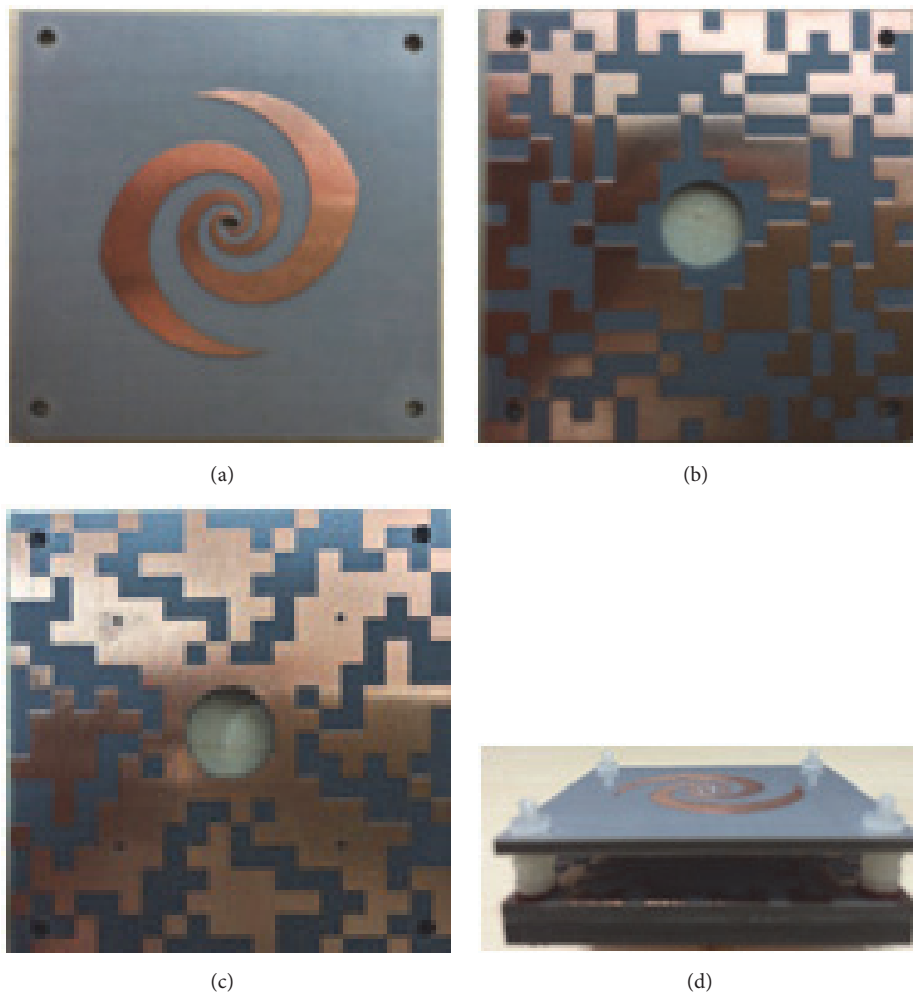


FIGURE 12: (a) Equiangular spiral antenna, (b) parasitic layer 1, (c) parasitic layer 2, and (d) side view of Ant2.

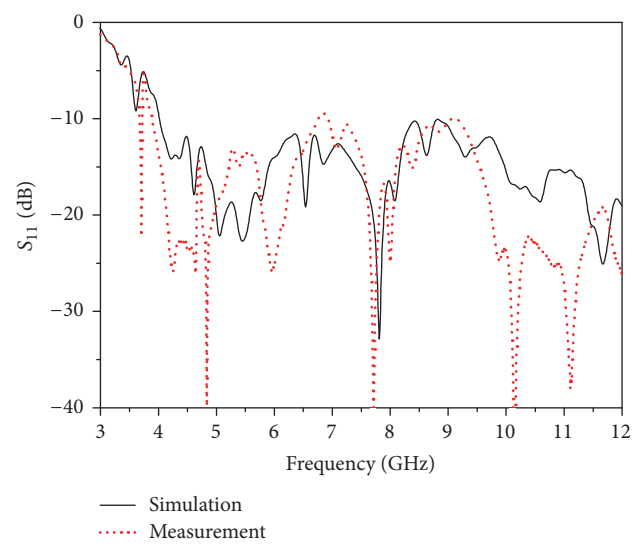


FIGURE 13: Simulated and measured  $S_{11}$  of the fabricated Ant2.

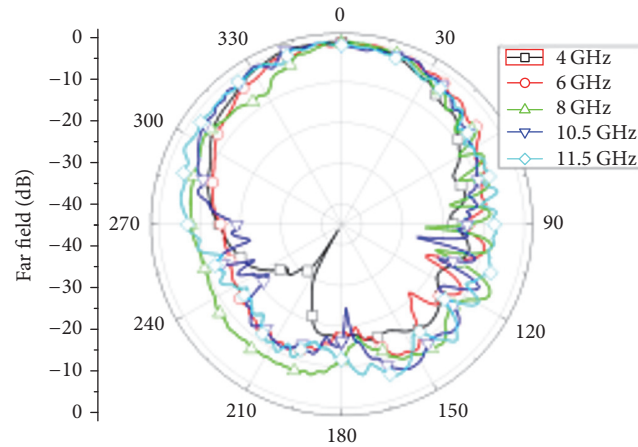


FIGURE 14: The measured far field pattern of Ant2 at 4 GHz, 6 GHz, 8 GHz, 10.5 GHz, and 11.5 GHz.

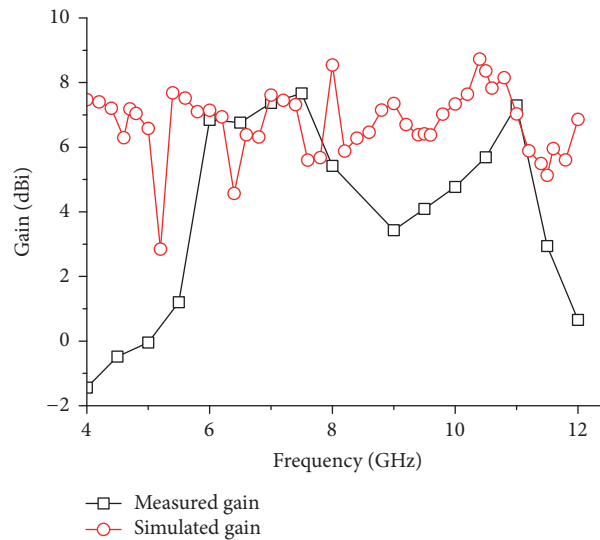


FIGURE 15: Simulated and measured gain of Ant2.

## Conflicts of Interest

The authors declare that they have no conflicts of interest.

## References

- [1] Q. Liu, C. L. Ruan, L. Peng et al., "A novel compact archimedean spiral antenna with gap-loading," *Progress In Electromagnetics Research Letters*, vol. 3, pp. 169–177, 2008.
- [2] K. Fujita, K. Yoshitomi, K. Yoshida, and H. Kanaya, "A circularly polarized planar antenna on flexible substrate for ultra-wideband high-band applications," *AEU - International Journal of Electronics and Communications*, vol. 69, no. 9, pp. 1381–1386, 2015.
- [3] H. Nakano, Y. Shinma, and J. Yamauchi, "A monofilar spiral antenna and its array above a ground plane-formation of a circularly polarized tilted fan beam," *IEEE Transactions on Antennas and Propagation*, vol. 45, no. 10, pp. 1506–1511, 1997.
- [4] J. Thaysen, K. B. Jakobsen, and H.-R. Lenler-Eriksen, "Wide-band cavity backed spiral antenna for stepped frequency ground penetrating radar," in *Proceedings of the IEEE Antennas and Propagation Society International Symposium and USNC/URSI Meeting*, pp. 418–421, July 2005.
- [5] T. H. Liu, W. X. Zhang, M. Zhang, and K. F. Tsang, "Low profile spiral antenna with PBG substrate," *Electronics Letters*, vol. 36, no. 9, pp. 779–780, 2000.
- [6] Z. Li, G. Wang, and Y. Cao, "A low-profile equiangular spiral antenna using a novel EBG ground plane," in *Proceedings of the 7th International Symposium on Antennas, Propagation & EM Theory, (ISAPE '06)*, pp. 1–3, 2006.
- [7] J. Lao, R. H. Jin, and J. P. Geng, "UWB spiral antenna with parabolic reflector," *XXIX URSI General Assembly, Chicago, Illinois, USA, 2008*, [https://www.researchgate.net/publication/228858199\\_UWB\\_Spiral\\_Antenna\\_with\\_Parabolic\\_Reflector](https://www.researchgate.net/publication/228858199_UWB_Spiral_Antenna_with_Parabolic_Reflector).
- [8] H. Nakano, R. Satake, and J. Yamauchi, "Extremely low-profile, single-arm, wideband spiral antenna radiating a circularly polarized wave," *IEEE Transactions on Antennas and Propagation*, vol. 58, no. 5, pp. 1511–1520, 2010.

- [9] Q. Wu, R. Jin, J. Geng, and D. Su, "On the performance of printed dipole antenna with novel composite corrugated-reflectors for low-profile ultrawideband applications," *IEEE Transactions on Antennas and Propagation*, vol. 58, no. 12, pp. 3839–3846, 2010.
- [10] Y. M. Pan, S. Y. Zheng, and B. J. Hu, "Wideband and low-profile omnidirectional circularly polarized patch antenna," *IEEE Transactions on Antennas and Propagation*, vol. 62, no. 8, pp. 4347–4351, 2014.
- [11] M. Ding, R. Jin, and J. Geng, "Optimal design of ultra wideband antennas using a mixed model of 2-D genetic algorithm and finite-difference time-domain," *Microwave and Optical Technology Letters*, vol. 49, no. 12, pp. 3177–3180, 2007.
- [12] R. L. Haupt and D. H. Werner, *Genetic Algorithms in Electromagnetics*, Wiley-IEEE Press, 2007.
- [13] Y. Kim and E. K. Walton, "Automobile conformal antenna design using non-dominated sorting genetic algorithm (NSGA)," *IEE Proceedings: Microwaves, Antennas and Propagation*, vol. 153, no. 6, pp. 579–582, 2006.
- [14] J. Kennedy and R. Eberhart, "Particle swarm optimization," in *Proceedings of the IEEE International Conference on Neural Networks (ICNN '95)*, vol. 4, pp. 1942–1948, 1995.
- [15] J. Robinson and Y. Rahmat-Samii, "Particle swarm optimization in electromagnetics," *IEEE Transactions on Antennas and Propagation*, vol. 52, no. 2, pp. 397–407, 2004.
- [16] N. Jin and Y. Rahmat-Samii, "Hybrid real-binary particle swarm optimization (HPSO) in engineering electromagnetics," *IEEE Transactions on Antennas and Propagation*, vol. 58, no. 12, pp. 3786–3794, 2010.
- [17] S. Rani and A. P. Singh, "On the design and optimisation of new fractal antenna using PSO," *International Journal of Electronics*, vol. 100, no. 10, pp. 1383–1397, 2013.
- [18] A. Sharaqa and N. Dib, "Design of linear and circular antenna arrays using biogeography based optimization," in *Proceedings of the 1st IEEE Jordan Conference on Applied Electrical Engineering and Computing Technologies (AEECT '11)*, pp. 1–6, Amman, Jordan, December 2011.
- [19] U. Singh, D. Singh, and P. Singh, "Concentric Circular Antenna Array design using hybrid differential evolution with Biogeography Based Optimization," in *Proceedings of the 4th IEEE International Conference on Computational Intelligence and Computing Research*, 2013.

## Review Article

# A Review of Sensing Strategies for Microwave Sensors Based on Metamaterial-Inspired Resonators: Dielectric Characterization, Displacement, and Angular Velocity Measurements for Health Diagnosis, Telecommunication, and Space Applications

Lijuan Su, Javier Mata-Contreras, Paris Vélez, and Ferran Martín

*CIMITEC, Departament d'Enginyeria Electrònica, Universitat Autònoma de Barcelona, 08193 Bellaterra, Spain*

Correspondence should be addressed to Lijuan Su; [lijuan.su@uab.cat](mailto:lijuan.su@uab.cat)

Received 17 January 2017; Accepted 9 March 2017; Published 14 May 2017

Academic Editor: Mirko Barbuto

Copyright © 2017 Lijuan Su et al. This is an open access article distributed under the Creative Commons Attribution License, which permits unrestricted use, distribution, and reproduction in any medium, provided the original work is properly cited.

Four sensing approaches for the implementation of microwave sensors based on transmission lines loaded with metamaterial-inspired resonators are considered in this review paper, and examples of applications are pointed out. In all the cases, sensing is based on the effects that the magnitude under measurement causes in the transmission properties of the resonator-loaded line. Such four strategies are (i) resonance frequency variation, (ii) coupling modulation through symmetry disruption (causing variation of the notch depth), (iii) frequency splitting (also exploiting symmetry properties), and (iv) amplitude modulation of a harmonic signal. Such sensors are useful in various scenarios, of interest in fields as diverse as characterization of dielectric materials for communication circuits, medical diagnosis and treatment with microwave technologies, and sensors for space applications, among others.

## 1. Introduction

Metamaterial-inspired resonators are electrically small resonant particles useful for the implementation of one-dimensional (e.g., metamaterial transmission lines [1]), two-dimensional (e.g., metasurfaces [2]), and three-dimensional (e.g., lenses for MRI [3]) metamaterials. Such resonant elements are “atoms” (sometimes called “meta-atoms”), which can be structured (or engineered) to form periodic artificial materials with unusual electromagnetic properties (negative refraction [4], backward wave propagation [5] and radiation [6], slow and fast waves [4–7], cloaking [8], etc.). Such properties, in general, arise as long as the composite acts as an effective medium for the electromagnetic field with which it interacts. In an effective medium, the properties can be tailored to some extent and are different from those of the constitutive elements, typically conventional metals and dielectrics in most metamaterials (obviously, this does not exclude the use of advanced materials, such as ferroelectrics [9, 10],

liquid crystals [11, 12], and graphene [13], or components, such as microelectromechanical systems—MEMS [14, 15]). A well-known example of unusual (effective medium) property is the negative refractive index achievable in composites made of split ring resonators (SRRs) and metallic strips (or posts), related to the simultaneous negative effective permeability (due to the SRRs) and permittivity (related to the metallic strips) of the structure [7]. Key to achieve such effective medium properties is the characteristic dimension (period) of the composite, which must be much smaller than the wavelength of the illuminating radiation. In this regard, metamaterial-inspired resonators are semilumped elements with electrical size significantly smaller than the wavelength at their fundamental resonance frequency, and hence they are useful particles (“atoms”) for the implementation of metamaterials. Examples of such resonant elements are the SRR [16], the complementary split ring resonator (CSRR) [17], the broadside coupled SRR (BC-SRR) [18], the electric LC (ELC) resonator [19], the S-shaped SRR (S-SRR) [20],

the folded SIR (F-SIR) [21], and many others (the authors recommend the book [22] for an exhaustive list, analysis, and applications of such resonant particles).

Besides these effective medium properties, which arise in periodic (or quasi-periodic) structures made of the previous (or other) metamaterial resonators and are useful for the implementation of microwave components with small size or superior performance or based on novel functionalities [1, 22], it is possible to use the resonance, electrical size, shape, and specific properties of some metamaterial resonators in other applications, including sensing (the purpose of this review article). Metamaterial-inspired resonators are very useful particles for the implementation of compact, high-sensitivity, and robust sensors on the basis of different strategies or approaches, for applications as diverse as characterization of dielectric materials for communication circuits, medical diagnosis and treatment with microwave technologies, and sensors for space applications, among others.

In this paper, four sensing approaches for the implementation of microwave sensors based on metamaterial resonators are reviewed, and examples of applications are pointed out. In all the cases, the sensing strategies are based on transmission lines loaded with such resonant elements. Such lines resemble metamaterial transmission lines, but the resonance phenomenon, rather than effective medium properties, is exploited. Such sensing strategies are resonance frequency variation, coupling modulation through symmetry disruption (causing variation of the notch depth), frequency splitting (also exploiting symmetry properties), and amplitude modulation of a harmonic signal.

## 2. Sensing Strategies

In this section, the four sensing strategies (or principles) are reviewed, whereas some applications of them are included in the next section.

*2.1. Sensors Based on Frequency Variation.* A transmission line loaded with a resonant element (either coupled to it or in contact with it) exhibits a set of transmission zeros (notches) in the frequency response. These transmission zeros occur at those frequencies where the resonant element produces an open or a virtual ground to the line, and the injected power is completely reflected back at these frequencies (excluding the effects of losses). Typically, the frequency of interest for microwave circuit and sensor design is the first (fundamental) resonance frequency, where metamaterial resonators can be used in order to achieve compact dimensions. This frequency (and higher order harmonic frequencies) may be altered by the effects of external stimulus or perturbations (e.g., moisture, temperature), by the relative position or orientation between the line and the resonant element (distance, lateral displacement, etc.), or by the presence of substances/materials surrounding the resonant element. Therefore, it follows that resonance frequency variation can be used for sensing many different variables, including position, velocity, material characteristics (e.g., permittivity), and moisture. These sensors are in general very simple but may suffer from cross-sensitivities, defined as the sensitivity of the

sensors to other variables different from the one of interest (measurand). For example, since permittivity depends on environmental conditions (e.g., temperature), the resonance frequency can be unintentionally shifted by spurious effects in permittivity sensors. Nevertheless, in many applications, external factors such as temperature or humidity do not experience significant variations. Moreover, these frequency variation based sensors are typically calibrated for accurate measurements. Therefore, these sensors are useful in many applications where design simplicity and low cost are key aspects.

*2.2. Coupling Modulation Based Sensors.* This sensing approach belongs to the so-called symmetry-based sensing [22–24], where symmetry properties are exploited for the implementation of sensors. In these sensors, a transmission line is loaded with a single symmetric resonator (electromagnetically coupled to the line), and the sensing principle is the control of the level of coupling between the line and the resonator, caused by the measurand and related to disruption of symmetry. These sensors are particularly useful for the measurement of spatial variables (e.g., alignment, displacement, and velocity) [24–27], and in this case the resonator is etched on a substrate (or object) different from that of the transmission line, in order to allow for a relative motion between the line and the resonator. However, symmetry can also be disrupted by asymmetric dielectric loading of the resonant element.

In these sensors, the symmetry plane of the transmission line is aligned with the symmetry plane of the resonant element, and both symmetry planes must be of different electromagnetic nature (one an electric wall and the other one a magnetic wall). Under these conditions, line-to-resonator coupling is prevented, and the structure exhibits total transmission. Conversely, by breaking symmetry through the effects of the variable under measurement (e.g., a spatial variable), a transmission zero, or notch, appears, and the notch depth depends on the level of asymmetry, since such level determines the magnitude of electromagnetic coupling between the line and the resonant element. Figure 1 illustrates this sensing principle, where symmetry disruption is caused by lateral displacement of the resonant element, a SRR, and the considered transmission line is a CPW. It is interesting to mention that, for the parasitic slot mode (odd mode) of the CPW transmission line, where the axial plane is an electric wall, rather than a magnetic wall, the structure exhibits a notch when the SRR is symmetrically loaded.

As compared to the previous approach, a key advantage of coupling modulation sensors is their robustness against variable environmental conditions. The reason is that the principle of operation relies on geometrical alignment/misalignment, which cannot be altered by environmental factors. Although these sensors cannot be considered to be true differential sensors, indeed they exhibit a similar behavior since the net coupling between the line and the resonator can be expressed in terms of the difference between partial couplings related to each half of the structure [32]. The output variable in these sensors is the notch depth expressed in dB (as usual to quantify attenuation). A disadvantage of these

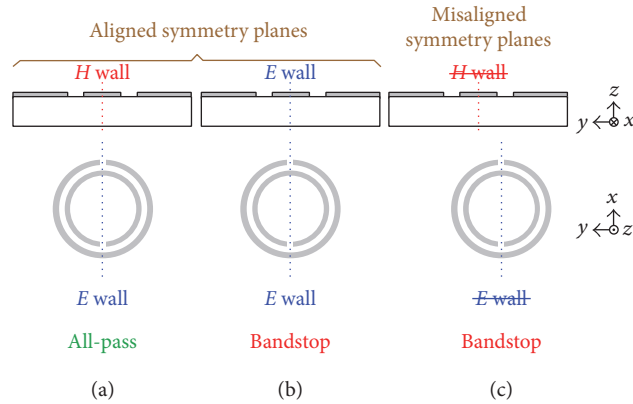


FIGURE 1: CPW transmission line loaded with a single SRR. (a) Line and resonator aligned and excitation with the fundamental (even) mode; (b) line and resonator aligned and excitation with the slot (odd) mode; (c) line and resonator misaligned and excitation with the fundamental (even) mode. It is apparent that, for misaligned loadings, the magnetic wall at the symmetry plane of the line is altered.

sensors is, therefore, their susceptibility to electromagnetic interference (EMI) and noise. Nevertheless, the resonance frequency of the resonant element can be tailored in order to avoid interfering signals (if they are present). Shielding of the sensors is also an alternative to mitigate the effects of EMI. For the measurement of spatial variables, these sensors are very interesting since the measurement can be contactless (by means of an air gap between the line and the resonator). By this means, mechanical friction is avoided, and aging effects are less severe as compared to sensors where friction is present, such as in rotary potentiometers [33].

**2.3. Frequency Splitting Sensors.** In this approach, the sensors are composed of a transmission line loaded with a pair of resonators in a symmetric configuration. The sensing principle is based on resonance frequency splitting. Thus, in the reference (symmetric) state, the structure exhibits a single notch, but two notches appear when symmetry is disrupted, and the frequency separation between them is related to the level of asymmetry [23].

Typically, these sensors find applications in material characterization. A test region in the vicinity of the resonators should be defined. By adding a material or substance in those regions, a single transmission zero appears if the material distribution (specifically the permittivity) is symmetric. On the contrary, if the material loading is not symmetric, two notches in the transmission coefficient, indicative of such asymmetry, arise. Note that this strategy is useful for the implementation of sensors and comparators. Such sensors are differential sensors, able to provide the difference between two permittivity values. As a comparator, the structure solely compares two permittivities, indicating whether their values are the same or not. This latter application is useful for the detection of defects or abnormalities in material samples as compared to a well-known reference. Similar to the previous sensing approach, frequency splitting sensors are robust in front of changing environmental conditions since a true differential measurement is performed in such sensors.

One important drawback of these frequency splitting sensors is the coupling between resonators, unavoidable if

these resonators are close enough. Coupling tends to degrade sensor performance, specifically the sensitivity at small perturbations, as reported in [34]. To circumvent the coupling between resonant elements, one possibility is to cascade the resonant elements [35]. By this means, the structure is not necessarily symmetric, but the working principle is exactly the same. However, if the resonators are separated enough, coupling no longer arises. Alternatively, a divider/combiner configuration, where each transmission line branch is loaded with a resonant element, can be considered [30, 36]. In this case, coupling is prevented, but, in general, the two notches for the asymmetric configuration are related to an interference phenomenon. The result is that sensitivity is degraded as well, unless the lengths of the transmission line sections of the splitter/combiner are appropriately chosen [30, 36]. Figure 2 depicts the three considered configurations, where the resonant element is a stepped impedance resonator (SIR).

As reported in [30], the electrical lengths of the transmission line sections connecting the Y-junction of the divider/combiner with the plane where the SIRs are connected (Figure 2(c)) must be exactly  $\pi$  at the fundamental resonance frequency of the SIRs. With this choice, the shorts at the plane where the SIRs are connected to the lines are translated to the Y-junction, and a transmission zero at the frequency of the SIRs arises. By disrupting symmetry by altering one of the SIRs (e.g., by means of a dielectric load), the transmission zero at the SIRs frequency prevails, whereas the other one is a consequence of an interfering phenomenon. The fact that one of the transmission zeros is kept unaltered regardless of the level of asymmetry explains the optimized sensitivity under the mentioned conditions relative to the electrical length of the divider/combiner transmission line sections. Importantly, if the previous conditions are satisfied, the two notches that appear for the asymmetric case are quite similar. This is interesting in order to properly detect small perturbations (asymmetries).

**2.4. Amplitude Modulation Based Sensors.** These sensors consist of a transmission line fed by a harmonic signal tuned at the fundamental frequency of a certain resonator coupled

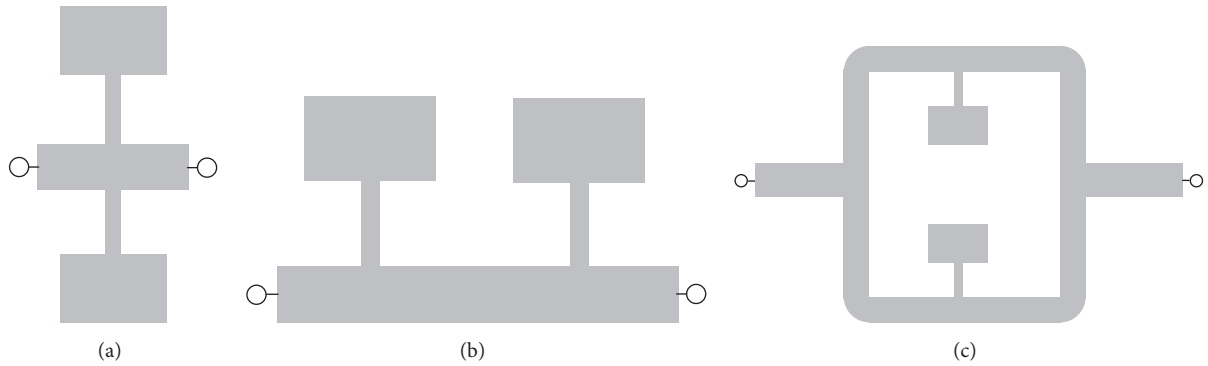


FIGURE 2: Various topologies of sensors based on microstrip lines loaded with SIRs. (a) Parallel configuration; (b) cascaded configuration; (c) splitter/combiner configuration.

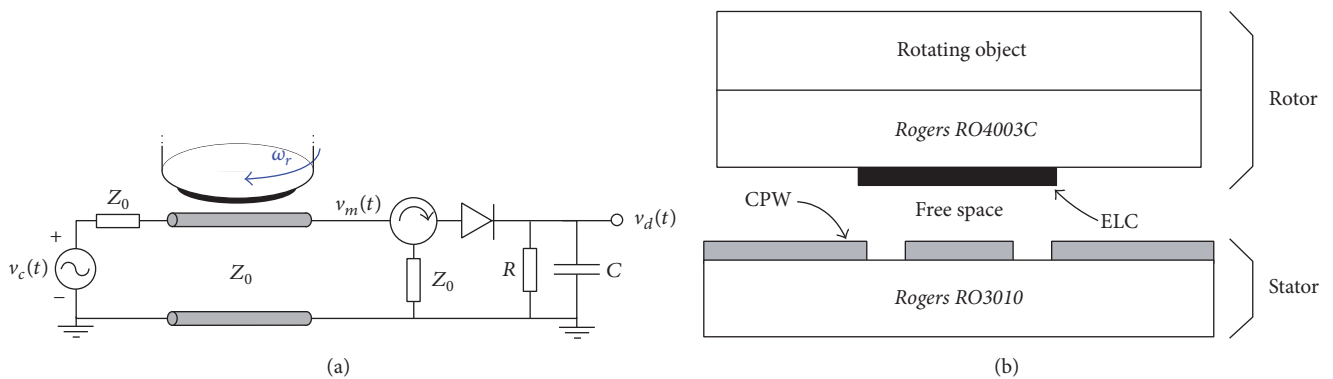


FIGURE 3: Schematic for the angular velocity measurement (axial configuration) (a) and cross section of the active part of the sensor (b).

to it. The amplitude of the feeding signal at the output port of the line depends on the level of coupling between the line and the resonant element. Namely, if the coupling is negligible, the line is transparent, and the amplitude at the output port is maximized. Conversely, if the coupling is significant, the injected signal is reflected back to the source, minimizing the amplitude of the output signal. Thus, line-to-resonator coupling effectively modulates the amplitude of the output signal, and this can be used for sensing purposes. Specifically, these amplitude modulation sensors are very appropriate for measuring angular velocities [31, 32, 37, 38]. One possible approach consists of using a symmetric resonant element exhibiting an electric wall at the fundamental resonance frequency, attached to a rotating object (rotor) in an axial configuration [32, 37, 38]. By placing the rotor in close proximity to the stator, a transmission line with a magnetic wall at its symmetry plane (e.g., a CPW transmission line), the coupling between the line and the resonator depends on the relative orientation between the symmetry planes of the line and resonator and hence on the angular position of the rotor. Since each time the axial plane of the line and the symmetry plane of the resonator are aligned the amplitude of the output signal is a maximum, and this occurs twice per cycle, it follows that the angular velocity can be inferred from the envelope of the modulated signal. To this end, a circulator and an envelope detector, implemented by means of a diode,

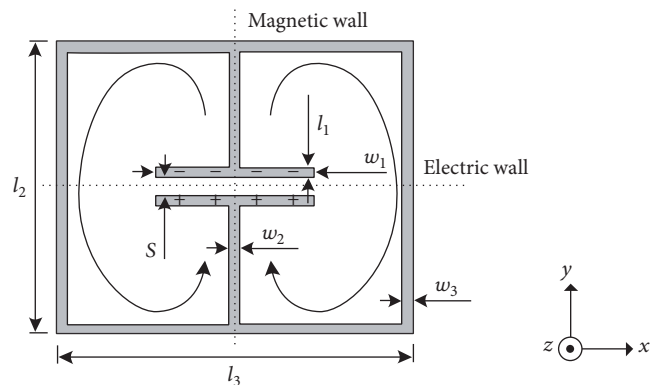


FIGURE 4: Topology of the bisymmetric ELC resonator with indication of charges and current flow at the fundamental resonance frequency.

are used. The circulator is sandwiched between the line and the detector, in order to prevent reflected signals from the diode. The schematic of the structure is depicted in Figure 3.

An appropriate resonator for the implementation of these angular velocity sensors is the so-called electric LC (ELC) resonator [19]. This resonant particle (see Figure 4) is bisymmetric, exhibiting an electric wall and a magnetic wall at the fundamental resonance. According to Section 2.2,

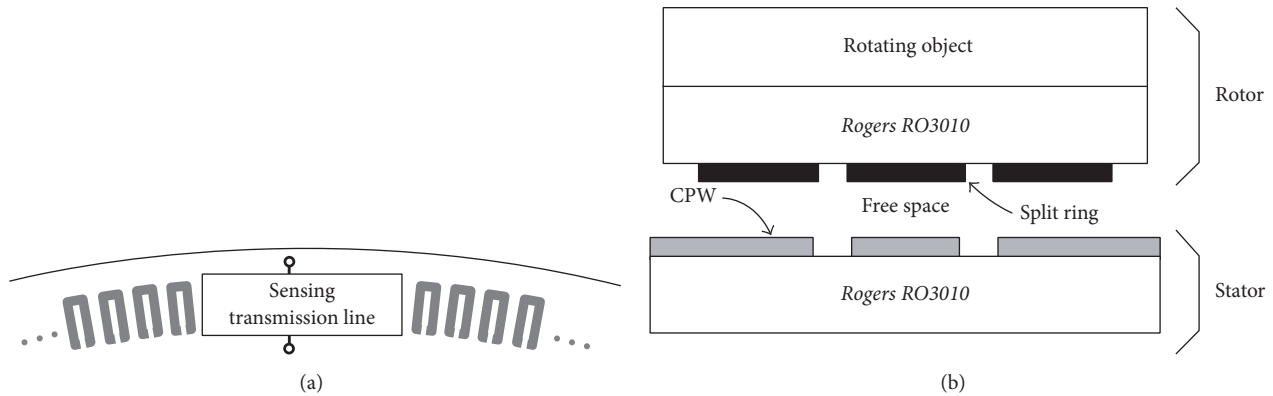


FIGURE 5: Perimetric configuration. (a) Top view scheme; (b) cross-sectional view.

when the electric wall of the ELC is aligned with the axial plane of the line, coupling is prevented and the line is transparent. Contrarily, the coupling is a maximum, and the transmission is a minimum, for an ELC angle corresponding to perfect alignment between the axial plane of the line and the magnetic wall of the resonant element. If both the ELC and the line are circularly shaped, the linearity between the amplitude of the output signal (in logarithmic scale) and the rotation angle is quite linear, and the sensor can be used for the measurement of angular position as well.

Alternatively to the axial configuration, the amplitude modulation based angular velocity sensors can be implemented by considering a chain of resonant elements distributed along the perimeter of the rotating object (rotor) [31]. In this case, the resonant elements must be oriented such that the coupling between the line (stator) and the resonator is maximized when the resonator is perfectly aligned with the axial plane of the line. Each time such alignment occurs, the amplitude (envelope) of the output signal is minimum, and hence the angular velocity can be inferred from the time between adjacent minimums (or maximums) and the number of resonant elements distributed along the circular chain. By this means, it is possible to measure instantaneous angular velocities with good accuracy, provided a large number of resonant elements in the rotor are considered. The schematic of the perimetric configuration is identical to the one shown in Figure 3, with the exception of the position of the stator (transmission line), which in this case is positioned in the external perimeter of the rotor, as indicated in Figure 5.

### 3. Examples of Applications

In this section, some examples of applications of the previous sensing strategies are given.

**3.1. Examples of Sensors Based on Frequency Variation.** The variation of the resonance frequency in SRR- and CSRR-loaded lines has been considered for sensing purposes. These resonators exhibit high sensitivity and are therefore good candidates for the implementation of sensors. By loading a microstrip line with a triangularly shaped CSRR, the coupling capacitance between the line and the resonator

strongly depends on the relative position between the line and the CSRR. Hence, these resonators can be used as displacement sensors. The idea, pointed out in [28], where a two-dimensional displacement sensor was proposed, consists of etching the triangular CSRRs on a movable substrate, different from the one where the line is etched. By this means, a relative motion between the line and the CSRRs can be achieved. In order to achieve sensing in two dimensions, a bended microstrip line was considered in [28], and two CSRRs in the separated substrate were etched as well. One of the CSRRs is in close proximity to one of the line sections, whereas the other one is in close proximity to the other line section, as depicted in Figure 6.

Note that two orthogonally polarized receiving and transmitting antennas were cascaded to the input and output ports of the host line in order to provide a wireless connection between the sensor and the source. Figure 6(c) shows the variation of the frequency response that is obtained by laterally displacing one of the rings with regard to the line axis.

Another example concerns sensors able to spatially resolve the dielectric properties of a material. It has been achieved in [29] by loading a line with an array of SRRs tuned at different frequencies. In such sensors, a frequency shift of one individual resonant peak indicates the dielectric properties of the material under test and its location within the array. One of the structures considered in [29] is depicted in Figure 7 and corresponds to a transmission line loaded with two SRRs. In the figure, the presence of pig lung tissue can be observed in the sensitive region of one of the SRRs. Figure 7(b) shows the response of a similar structure with four SRRs and pig lung tissue in one of them. The variation of the corresponding resonance peak can be appreciated, indicating the presence of a different material on top of the sensitive region of the SRR.

Finally, CSRR-loaded microstrip lines can be used as sensors to characterize dielectric samples [39–42], particularly microwave substrates (used for circuit implementation). In these sensors, the dielectric constant is determined from the shift of the resonance frequency experienced when the material under test is placed in contact with the CSRR of the line. Such dielectric constant can be inferred through

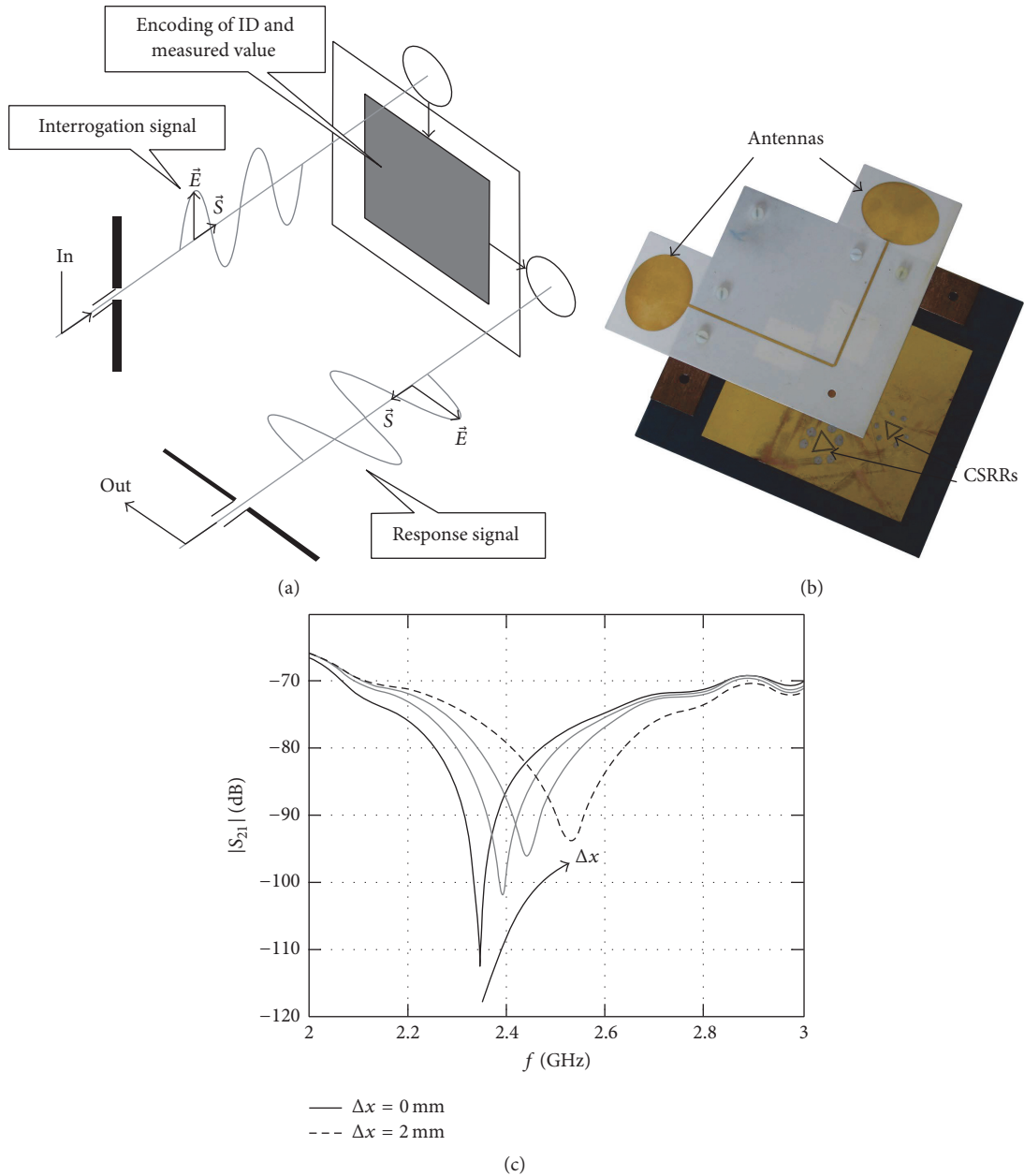


FIGURE 6: Two-dimensional wireless displacement sensor based on detuning of triangularly shaped CSRRs. (a) Scheme showing the polarization decoupling of interrogation and response signals; (b) photograph; (c) frequency response for various displacement values. For better visualization in (b), the movable sensitive plate was rotated  $180^\circ$ . Reprinted with permission from [28].

a calibration curve, by considering dielectric slabs with known permittivity. However, if the dielectric constant of the substrate is known, it is possible to obtain the dielectric constant of the sample under test (SUT) from the following expression:

$$\epsilon_{\text{SUT}} = 1 + \frac{(\omega_0'^{-2} - \omega_0^{-2})}{L_c C_c} (1 + \epsilon_r), \quad (1)$$

where  $L_c$  and  $C_c$  are the inductance and capacitance of the CSRR in the CSRR-loaded line without SUT,  $\epsilon_r$  is the dielectric constant of the substrate, and  $\omega_0$  and  $\omega_0'$  are

the notch frequencies of the structure without and with SUT, respectively. As an example, the CSRR-loaded line of Figure 8 has been loaded with a dielectric sample (SUT) corresponding to an identical substrate to that of the line (Rogers RO3010 with dielectric constant 10.2). The measured response of the line with and without the SUT is depicted in Figure 8(b). In the structure without the SUT,  $L_c$  and  $C_c$  have been inferred from the parameter extraction method reported in [43]. Thus, expression (1) can be evaluated, and the dielectric constant of the SUT has been found to be  $\epsilon_{\text{SUT}} = 9.39$ , in good agreement with the nominal value. It is worth

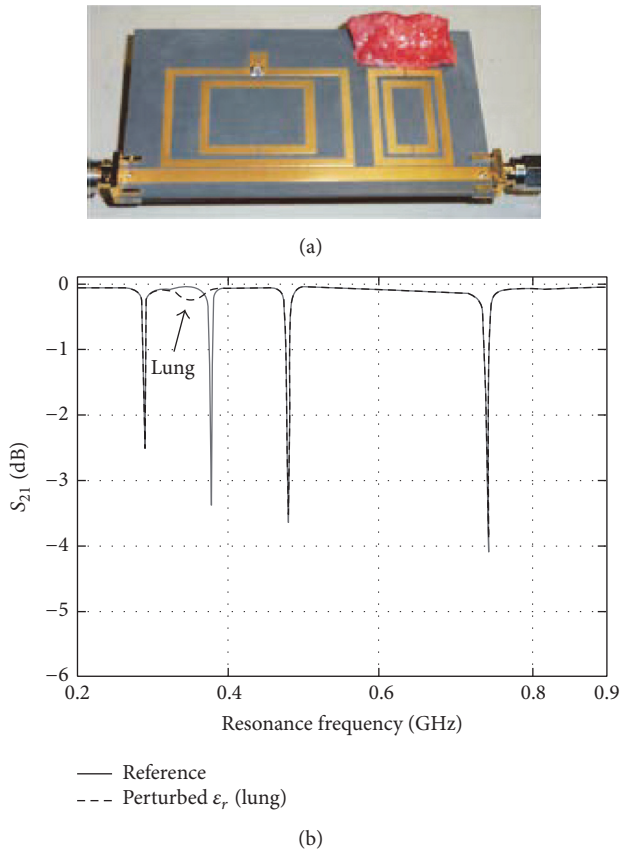


FIGURE 7: (a) Transmission line loaded with two SRRs and pig lung tissue on top of the sensitive region of one of the SRRs; (b) frequency response for the case of 4 SRRs loading the line. Reprinted with permission from [29].

mentioning that we have repeated the measurements several times by putting pressure to the SUT in order to minimize the effects of the air gap and the results are stable.

**3.2. Examples of Sensors Based on Coupling Modulation.** Several types of sensors based on coupling modulation have been reported [24–27, 32]. Most of them use the transmission coefficient of a transmission line loaded with one or several resonant elements. A different approach is used in [27], where a two-dimensional displacement and alignment sensor is implemented on the basis of the reflection coefficients of orthogonally oriented open microstrip lines loaded with SRRs. The layout of the device is depicted in Figure 9. For the unperturbed state, the resonators are not excited and the injected signals to both ports are reflected back to the source. Hence, the reflection coefficients are  $|S_{11}| = |S_{22}| = 1$ . However, if the alignment is broken by displacement in the  $x$ - and  $y$ -directions, the SRRs will be excited and notches will appear in the reflection coefficients. Further displacement in the  $x$ - and  $y$ -directions gives rise to a stronger coupling between the transmission lines and the SRRs, in turn resulting in deeper notches in the reflection coefficients at the resonance frequency of the SRRs. These notches result from radiation effects, and this is another relevant feature

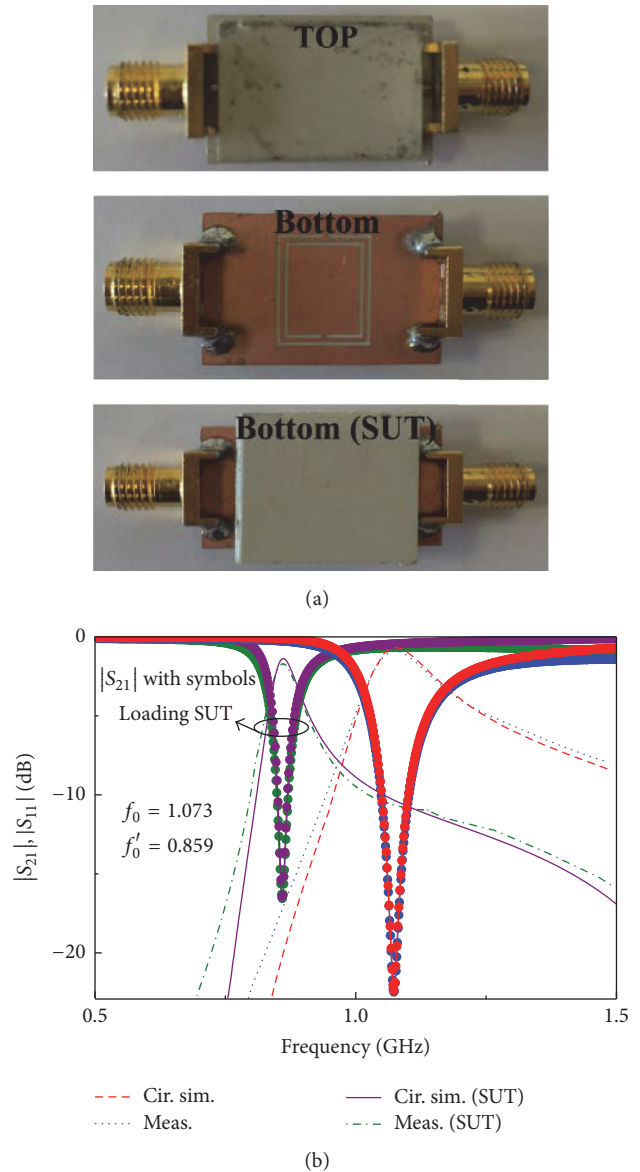


FIGURE 8: CSRR-loaded line used as permittivity sensor (a) and insertion and return loss (b). The reactive elements values are  $C_c = 6.81$  pF and  $L_c = 2.42$  nH. Note that in the top view the metallic strip of the microstrip line is not visible since it is covered by a piece of slab with the same parameters as the substrate. This has been done in order to have a homogeneous material surrounding the line strip, resulting in an embedded microstrip line, required in this application.

of this sensing strategy based on (one-port) open-ended transmission lines.

Note that displacement in the  $x$ -direction has no effect on the depth of notch in  $|S_{22}|$  (nor displacement in the  $y$ -direction onto  $|S_{11}|$ ). Thus, misalignment in the  $x$ - and  $y$ -directions can be independently sensed from the depth of notches in  $|S_{11}|$  and  $|S_{22}|$ , respectively. One advantage of this method is that both SRRs can be designed to operate at the same resonance frequency. This is in contrast to the previous two-dimensional displacement sensor based on the

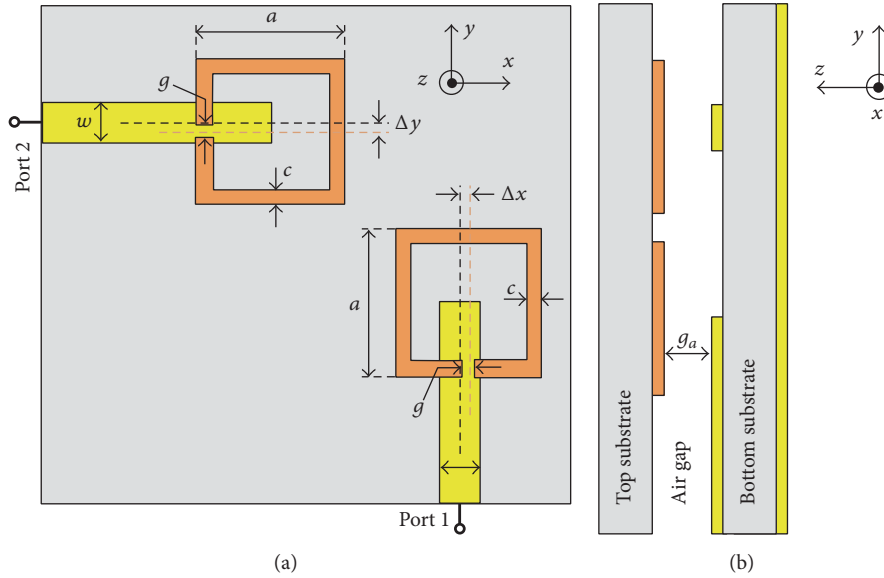


FIGURE 9: Top (a) and side (b) views of the two-dimensional displacement sensor based on the resonance in the reflection coefficients. The structures are patterned on Rogers RO4003 substrates with 0.81 mm thickness. The geometrical dimensions of the line and SRR are  $w = 1.84$  mm,  $a = 7$  mm,  $g = 0.5$  mm, and  $c = 0.5$  mm. There is an air gap with  $g_a = 0.76$  mm between the two substrates. Reprinted with permission from [27].

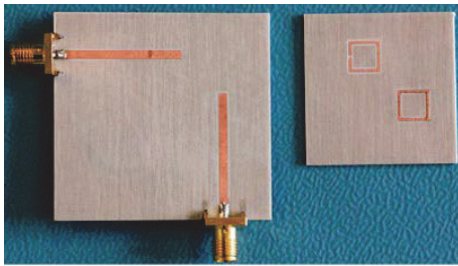


FIGURE 10: Photograph of the fabricated sensor implemented through open-ended transmission lines. Reprinted with permission from [27].

transmission characteristics of a CPW, where SRRs needed to have distinct resonance frequencies. Note that the direction of motion cannot be determined with the sensor depicted in Figure 9. Nevertheless, additional resonant elements, tuned at different frequencies, can be added to the movable substrate in order to distinguish the directions of motion.

The photograph of the fabricated device is shown in Figure 10. Figure 11 depicts the reflection coefficient measured from any of the ports for different lateral displacement values (seen from the corresponding port). One important feature of the proposed sensor is that displacement affects only the depth of the notch and leaves the resonance frequency nearly intact. A fixed resonance frequency is an important feature that enables the proposed sensor to operate at a fixed frequency. This invariability of the resonance frequency is due to the fact that such frequency mainly depends on the characteristics of the SRRs, rather than on their coupling to the line. However, for some resonators and lines, the

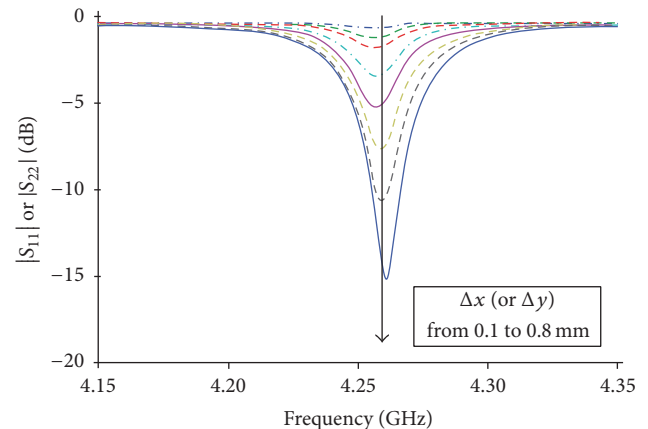


FIGURE 11: Measured  $|S_{11}|$  (or  $|S_{22}|$ ) for different values of displacement  $\Delta x$  (or  $\Delta y$ ) from 0.1 to 0.8 mm in steps of 0.1 mm. Reprinted with permission from [27].

SRRs may be affected by the presence of the line and this invariability is not always guaranteed.

**3.3. Examples of Sensors Based on Frequency Splitting.** Let us consider in this section frequency splitting sensors based on splitter/combiner structures loaded with SIRs [30]. The same type of sensors implemented by loading the splitter/combiners with CSRRs is reported in [36]. The photograph and frequency response of one of these sensors without loading on top of the SIRs are depicted in Figure 12. It can be appreciated that a single notch in the frequency response appears, as expected on account of symmetry. However, when symmetry is disrupted, the single notch is split into two

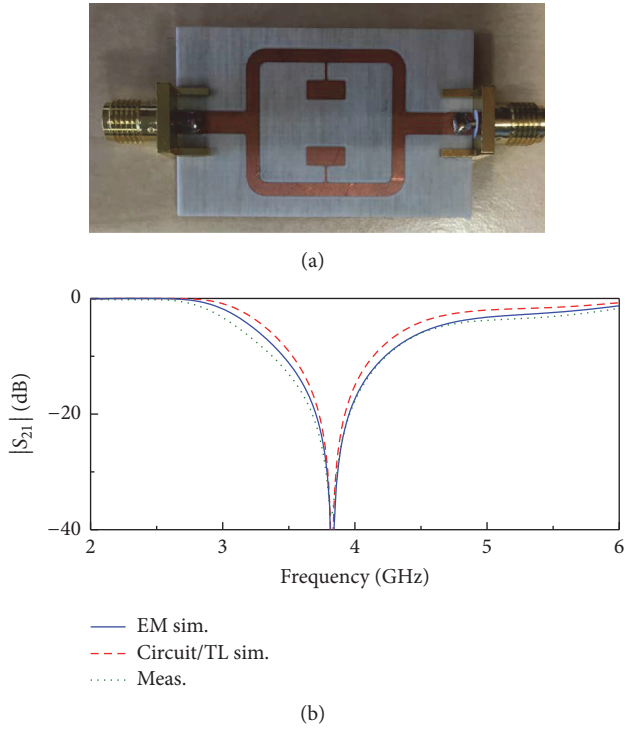


FIGURE 12: Fabricated splitter/combiner based sensor (a) and insertion loss (b). The structure has been fabricated on the *Rogers RO4003C* substrate with thickness  $h = 812.8 \mu\text{m}$  and dielectric constant  $\epsilon_r = 3.38$ . Reprinted with permission from [30].

notches. This is illustrated in Figure 13, where a trisection splitter/combiner structure is depicted, and the response to different loading combinations is reported. To this end, a dielectric slab (a square-shaped piece of unmetallized *Rogers RO3010* substrate with thickness  $h = 1.27 \text{ mm}$  and dielectric constant  $\epsilon_r = 10.2$ ) has been added on top of one of the SIRs of each pair. With these unbalanced loads, frequency splitting of the three resonance frequencies of the SIRs is expected, and this is confirmed from the measured response, also included in Figure 13. Then, each pair of SIRs has been loaded with unbalanced loads, but in this case considering dielectric slabs with different dielectric constants (i.e., square-shaped pieces of unmetallized *Rogers RO3010* substrate with thickness  $h = 1.27 \text{ mm}$  and dielectric constant  $\epsilon_r = 10.2$  and *Arlon CuClad 250 LX* with  $\epsilon_r = 2.43$  and  $h = 0.49 \text{ mm}$ ). Again, frequency splitting (see Figure 13) points out the difference in the dielectric constants of both slabs loading the different pairs of SIRs. To summarize, note that in the red curve only three notches are present, indicating that no loading is present in the three pairs of resonant elements. However, for the other curves, three pairs of notches appear as a consequence of unbalanced loads in the three pairs of resonant elements.

**3.4. Examples of Sensors Based on Amplitude Modulation.** In this section, an amplitude modulation based sensor potentially useful for the measurement of the angular velocity in reaction wheels of spatial vehicles is presented [31]. For that application, the perimetric configuration is more convenient

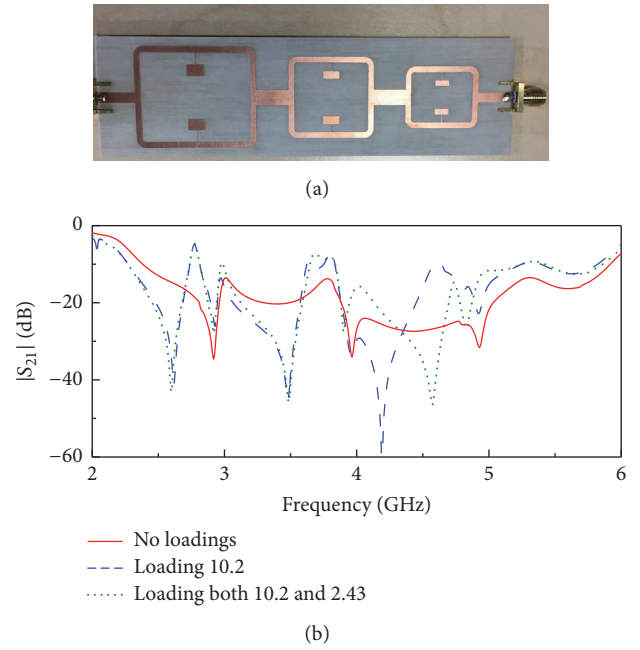


FIGURE 13: Fabricated trisection splitter/combiner sensor (a) and measured response (insertion loss), compared with the response that results by loading one of the SIRs of each pair with a dielectric slab of dielectric constant 10.2 and by loading both SIRs of each pair with dielectric slabs of different dielectric constants (10.2 and 2.43) (b). Reprinted with permission from [30].

than the axial configuration for two main reasons: (i) from a mechanical viewpoint, the axial configuration is more complex since the axial region of the wheels may contain the rotating axis, or other mechanical elements for rotation; (ii) with the perimetric configuration, the measurement of instantaneous velocities is possible, and the accuracy is determined by the number of resonant elements of the perimetric chain (see Section 2.4).

The sensor is based on a broadside coupled SRR (BC-SRR) loaded coplanar waveguide (CPW) (Figure 14(a)). The stator is a CPW loaded with a pair of split rings, whereas the rotor consists of a periodic circular chain of split rings, identical to those of the stator but rotated  $180^\circ$ . The cross-sectional view scheme of the assembly is indicated in Figure 14(b). Note that this configuration is not exactly the one indicated in Figure 5(b). The justification is as follows: in order to measure quasi-instantaneous angular velocities, the space between adjacent rings must be minimized. If a CPW is coupled directly to an array of split rings, as indicated in Figure 5(b), there are two cross-coupling effects: (i) the CPW is simultaneously coupled to multiple resonators and (ii) neighboring resonators are coupled to each other. Using the reported approach, both parasitic effects can be ignored; namely, the CPW is coupled only to the BC-SRRs and the interresonator coupling is at frequencies higher than the frequency of interest,  $f_0$ , the resonance frequency of the BC-SRR, which must be the frequency of the harmonic signal injected to the CPW. Figure 14(c) shows the insertion loss of the CPW at  $f_0$  for different relative displacement values

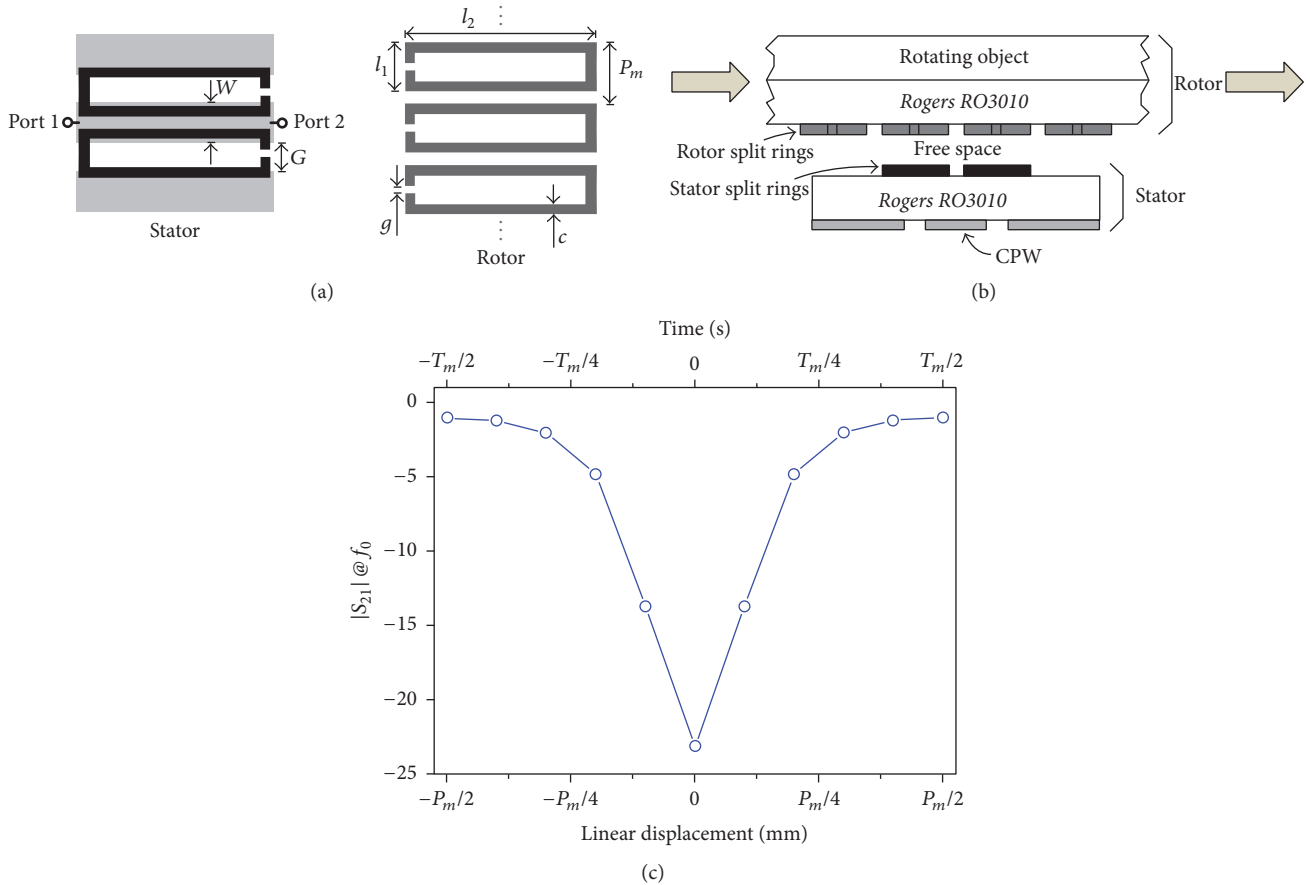


FIGURE 14: Layout of the stator and rotor parts (a), scheme of the cross-sectional view, indicating the direction of motion of the rotor (b), and insertion loss at  $f_0$  for different displacement values (0 mm displacement corresponds to the reference position). Reprinted with permission from [31].

between the rings of the rotor and those of the stator. It can be appreciated that maximum attenuation occurs for the reference position, defined as that in which a pair of rotor rings are aligned with the pair of stator rings, forming a perfect (aligned) BC-SRR.

The prototype of the sensor can be seen in Figure 15, where a chain of 300 resonators is etched over a 101.6 mm radius rotor. The experimental setup consists of a signal generator (*Agilent E4438C*), a Schottky diode (*Avago HSMS-2860*), an oscilloscope (*Agilent MSO-X-3104A*), and a stepper motor (*STM 23Q-3AN*) to control the displacement and velocity of the rotor. Figure 16 depicts the measured envelope function for a 3,000 rpm angular speed, where it can be appreciated that the period corresponds to this velocity, taking into account the number of resonators of the chain.

#### 4. Discussion

Let us briefly discuss some advantages of the sensors considered in the previous section. The use of metamaterial-inspired resonators for the implementation of sensors based on frequency variation has the main advantage of resonator size. This is especially critical in applications such as the one

reported in Figure 7 (sensors to spatially resolve the dielectric properties of a material). Moreover, these resonant elements (SRRs, CSRRs, etc.) typically exhibit good sensitivity (i.e., variation of frequency with dielectric properties or with spatial variables). Particularly, the use of CSRR for measuring dielectric properties of slabs, or even liquids [36, 39–41, 44], is very convenient since the capacitance (and hence resonance frequency) of these resonant elements is very sensitive to the presence of a dielectric load on top of the resonators.

In sensors based on coupling modulation or frequency splitting, the main advantage is that these sensors are similar to differential-mode sensors, and therefore they are robust in front of cross-sensitivities caused by external factors, since variations in variables related to ambient factors such as temperature or moisture have effects that are seen as common mode stimulus. Both sensor types are very useful as comparators as well. It is worth mentioning that coupling modulation sensors are more sensitive to noise, as compared to frequency splitting sensors, since the output variable is the notch depth. Nevertheless, the typical sensitivities and dynamic ranges of these coupling modulation sensors applied to the measurement of spatial variables have been found to be reasonable. Frequency splitting sensors are less sensitive

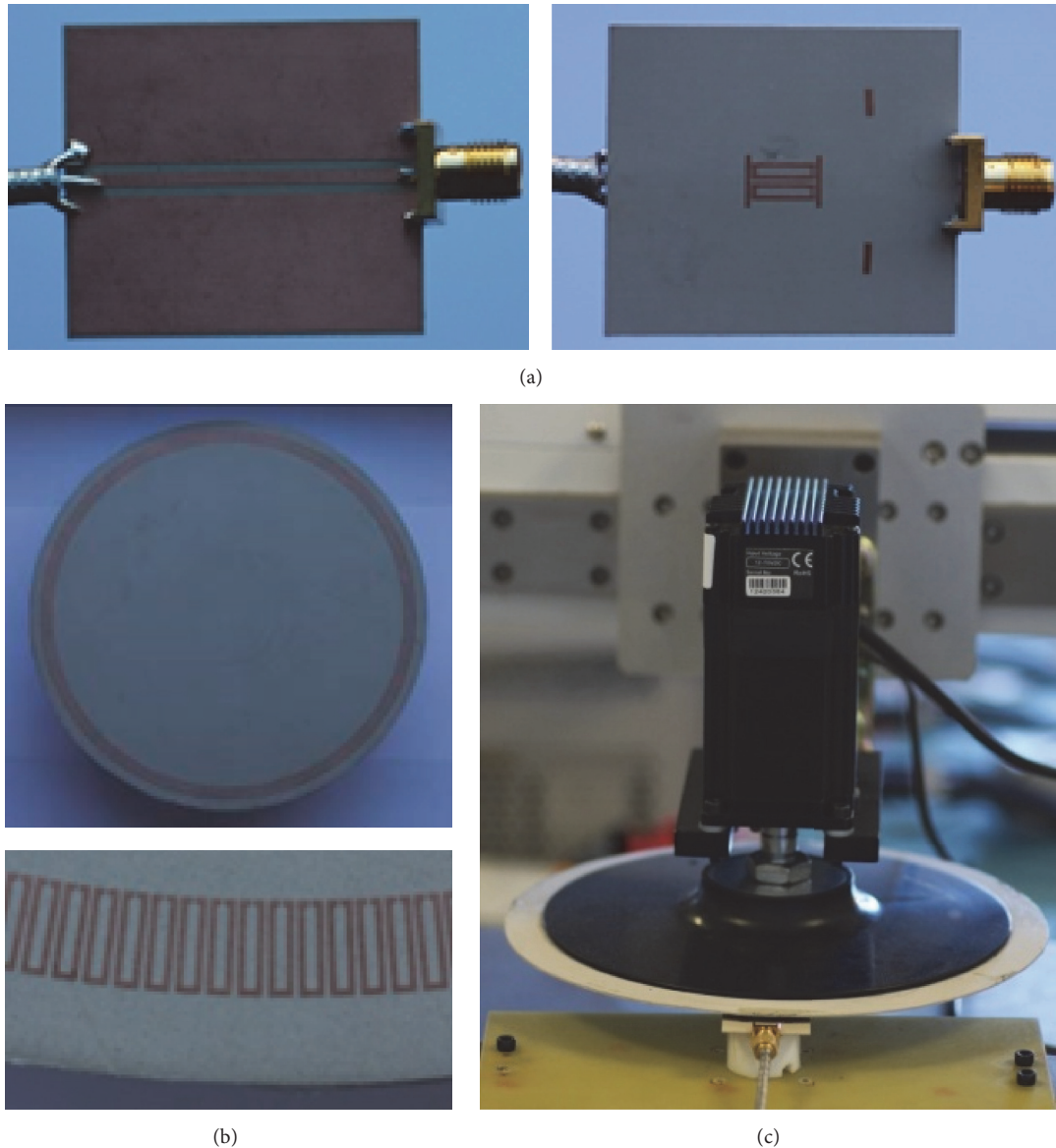


FIGURE 15: (a) Stator, (b) rotor, and (c) assembly of the prototype. Via holes and strips connecting the CPW ground planes are used to suppress the slot mode. Calibration marks on the stator are visible.

to noise and are suitable for real-time differential measurements. Moreover, it has been demonstrated that these sensors can be used for measuring several samples simultaneously.

Finally, the latter sensors of the previous section, based on amplitude modulation, can be considered a particular case of coupling modulation sensors, where the output variable is contained in the envelope function of an amplitude modulated carrier signal. The particular application is the measurement of the angular velocity, based on the distance between pulses in the envelope function. One figure of merit of these sensors is the number of pulses, which provides the angle resolution and determines the capability of the sensor to detect fast changes in the instantaneous angular velocity. In the proposed sensor, 300 pulses are considered, but this number can be enhanced by adding further resonant elements in an additional SRR chain (concentric but displaced

one semiperiod as compared to the one of Figure 15(b)) and an additional SRR pair in the rotor. As compared to optical encoders, these sensors are cheaper. As compared to angular velocity sensors based on potentiometers, the proposed sensors do not suffer from mechanical friction and hence are more robust against aging effects.

## 5. Conclusions

In conclusion, several sensing strategies for the implementation of microwave sensors based on metamaterial-inspired resonators have been reviewed, and examples of applications have been provided. Particularly, the reviewed sensors are useful for material characterization and as displacement and velocity sensors. Of interest for telecommunication circuits and space applications are the frequency variation sensors

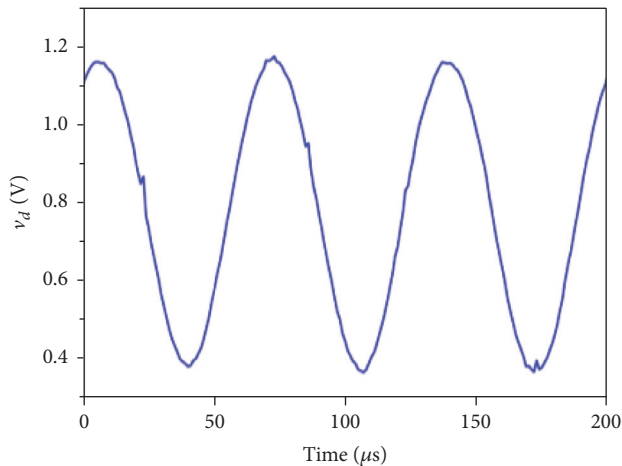


FIGURE 16: Measured envelope function for a 3,000 rpm speed. Reprinted with permission from [31].

based on CSRRs, useful to determine the dielectric constant of microwave substrates, and the amplitude modulation sensors based on BC-SRRs, which are able to provide the angular velocity of rotating cylinders and are therefore of potential interest to replace optical sensors in reaction wheels, or for the determination of the angular position in pointing mechanisms, among others.

## Conflicts of Interest

The authors declare that they have no conflicts of interest regarding the publication of this paper.

## Acknowledgments

This work has been supported by MINECO-Spain (Projects TEC2013-40600-R and TEC2016-75650-R) and by Generalitat de Catalunya (Project 2014SGR-157). Ferran Martín has been awarded with an ICREA Academia Award. The work has been also supported by FEDER funds. Lijuan Su acknowledges the China Scholarship Council (CSC) for Grant 201306950011.

## References

- [1] R. Marqués, F. Martín, and M. Sorolla, *Metamaterials with Negative Parameters: Theory, Design, and Microwave Applications*, John Wiley, 2007.
- [2] M. Aznabet, M. Navarro-Cía, S. A. Kuznetsov et al., "Polypropylene-substrate-based SRR- And CSRR-metasurfaces for submillimeter waves," *Optics Express*, vol. 16, no. 22, pp. 18312–18319, 2008.
- [3] J. D. Baena, L. Jelinek, R. Marqués, and J. Zehentner, "Electrically small isotropic three-dimensional magnetic resonators for metamaterial design," *Applied Physics Letters*, vol. 88, Article ID 134108, 2006.
- [4] R. A. Shelby, D. R. Smith, and S. Schultz, "Experimental verification of a negative index of refraction," *Science*, vol. 292, no. 5514, pp. 77–79, 2001.
- [5] F. Martín, F. Falcone, J. Bonache, R. Marqués, and M. Sorolla, "Split ring resonator-based left-handed coplanar waveguide," *Applied Physics Letters*, vol. 83, no. 22, pp. 4652–4654, 2003.
- [6] G. Zamora, S. Zuffanelli, F. Paredes, F. J. Herraiz-Martinez, F. Martín, and J. Bonache, "Fundamental-mode leaky-wave antenna (LWA) using slotline and split-ring-resonator (SRR)-based metamaterials," *IEEE Antennas and Wireless Propagation Letters*, vol. 12, pp. 1424–1427, 2013.
- [7] D. R. Smith, W. J. Padilla, D. C. Vier, S. C. Nemat-Nasser, and S. Schultz, "Composite medium with simultaneously negative permeability and permittivity," *Physical Review Letters*, vol. 84, no. 18, pp. 4184–4187, 2000.
- [8] D. Schurig, J. J. Mock, B. J. Justice et al., "Metamaterial electromagnetic cloak at microwave frequencies," *Science*, vol. 314, no. 5801, pp. 977–980, 2006.
- [9] M. Gil, C. Damm, A. Giere et al., "Electrically tunable splitting resonators at microwave frequencies based on barium-strontium-titanate thick films," *Electronics Letters*, vol. 45, no. 8, pp. 417–418, 2009.
- [10] M. Gil, C. Damm, M. Sazegar et al., "Tunable sub-wavelength resonators based on barium-strontium-titanate thick-film technology," *IET Microwaves, Antennas and Propagation*, vol. 5, no. 3, pp. 316–323, 2011.
- [11] C. Damm, M. Maasch, R. Gonzalo, and R. Jakoby, "Tunable composite right/left-handed leaky wave antenna based on a rectangular waveguide using liquid crystals," in *Proceedings of the IEEE MTT-S International Microwave Symposium (MTT '10)*, pp. 13–16, USA, May 2010.
- [12] M. Roig, M. Maasch, C. Damm, O. H. Karabey, and R. Jakoby, "Liquid crystal based tunable composite right/left-handed leaky-wave antenna for Ka-Band applications," in *Proceedings of the 43rd European Microwave Conference (EuMC '13)*, pp. 759–762, Nuremberg, Germany, October 2013.
- [13] R. Alaee, M. Farhat, C. Rockstuhl, and F. Lederer, "A perfect absorber made of a graphene micro-ribbon metamaterial," *Optics Express*, vol. 20, no. 27, pp. 28017–28024, 2012.
- [14] D. Bouyge, D. Mardivirin, J. Bonache et al., "Split ring resonators (SRRs) based on micro-electro-mechanical deflectable cantilever-type rings: application to tunable stopband filters," *IEEE Microwave and Wireless Components Letters*, vol. 21, no. 5, pp. 243–245, 2011.
- [15] D. Bouyge, A. Crunteanu, M. Durán-Sindreu et al., "Reconfigurable split rings based on MEMS switches and their application to tunable filters," *Journal of Optics (United Kingdom)*, vol. 14, no. 11, Article ID 114001, 2012.
- [16] J. B. Pendry, A. J. Holden, D. J. Robbins, and W. J. Stewart, "Magnetism from conductors and enhanced nonlinear phenomena," *IEEE Transactions on Microwave Theory and Techniques*, vol. 47, no. 11, pp. 2075–2084, 1999.
- [17] F. Falcone, T. Lopetegi, J. D. Baena, R. Marqués, F. Martín, and M. Sorolla, "Effective negative- $\epsilon$  stopband microstrip lines based on complementary split ring resonators," *IEEE Microwave and Wireless Components Letters*, vol. 14, no. 6, pp. 280–282, 2004.
- [18] R. Marqués, F. Medina, and R. Rafii-El-Idrissi, "Role of bianisotropy in negative permeability and left-handed metamaterials," *Physical Review B*, vol. 65, Article ID 144440, 2002.
- [19] D. Schurig, J. J. Mock, and D. R. Smith, "Electric-field-coupled resonators for negative permittivity metamaterials," *Applied Physics Letters*, vol. 88, no. 4, Article ID 041109, 2006.

- [20] H. Chen, L. Ran, J. Huangfu et al., "Left-handed materials composed of only S-shaped resonators," *Physical Review E*, vol. 70, Article ID 057605, 2004.
- [21] M. Makimoto and S. Yamashita, "Compact bandpass filters using stepped impedance resonators," *Proceedings of the IEEE*, vol. 67, no. 1, pp. 16–19, 1977.
- [22] F. Martín, *Artificial Transmission Lines for RF and Microwave Applications*, John Wiley, Hoboken, NJ, USA, 2015.
- [23] J. Naqui, *Symmetry Properties in Transmission Lines Loaded with Electrically Small Resonators: Circuit Modeling and Applications*, Springer Theses, 2016.
- [24] J. Naqui, M. Durán-Sindreu, and F. Martín, "Novel sensors based on the symmetry properties of split ring resonators (SRRs)," *Sensors*, vol. 11, no. 8, pp. 7545–7553, 2011.
- [25] J. Naqui, M. Durán-Sindreu, and F. Martín, "Alignment and position sensors based on split ring resonators," *Sensors*, vol. 12, no. 9, pp. 11790–11797, 2012.
- [26] A. Karami-Horestani, C. Fumeaux, S. F. Al-Sarawi, and D. Abbott, "Displacement sensor based on diamond-shaped tapered split ring resonator," *IEEE Sensors Journal*, vol. 13, no. 4, pp. 1153–1160, 2013.
- [27] A. K. Horestani, J. Naqui, D. Abbott, C. Fumeaux, and F. Martín, "Two-dimensional displacement and alignment sensor based on reflection coefficients of open microstrip lines loaded with split ring resonators," *IET Electronics Letters*, vol. 50, no. 8, pp. 620–622, 2014.
- [28] C. Mandel, B. Kubina, M. Schüßler, and R. Jakoby, "Passive chipless wireless sensor for two-dimensional displacement measurement," in *Proceedings of the 41st European Microwave Conference*, pp. 79–82, Manchester, UK, 2011.
- [29] M. Puentes, C. Weiss, M. Schussler, and R. Jakoby, "Sensor array based on split ring resonators for analysis of organic tissues," in *proceedings of the IEEE/MTT-S International Microwave Symposium (MTT '11)*, Baltimore, Md, USA, June 2011.
- [30] L. Su, J. Mata-Contreras, P. Vélez, and F. Martín, "Configurations of splitter/combiner microstrip sections loaded with stepped impedance resonators (sirs) for sensing applications," *Sensors*, vol. 16, no. 12, article 2195 pages, 2016.
- [31] J. Naqui and F. Martín, "Application of broadside-coupled split ring resonator (BC-SRR) loaded transmission lines to the design of rotary encoders for space applications," in *Proceedings of the IEEE/MTT-S International Microwave Symposium (IMS '11)*, San Francisco, Calif, USA, May 2016.
- [32] J. Naqui and F. Martín, "Transmission lines loaded with bisymmetric resonators and their application to angular displacement and velocity sensors," *IEEE Transactions on Microwave Theory and Techniques*, vol. 61, no. 12, pp. 4700–4713, 2013.
- [33] G. Urban, *Handbook of Modern Sensors: Physics, Designs, and Applications*, Springer, New York, NY, USA, 3rd edition, 2004.
- [34] J. Naqui, C. Damm, A. Wiens, R. Jakoby, L. Su, and F. Martín, "Transmission lines loaded with pairs of magnetically coupled stepped impedance resonators (SIRs): modeling and application to microwave sensors," in *Proceedings of the 2014 IEEE MTT-S International Microwave Symposium (IMS '14)*, Tampa, Fla, USA, June 2014.
- [35] J. Naqui, C. Damm, A. Wiens et al., "Transmission lines loaded with pairs of stepped impedance resonators: modeling and application to differential permittivity measurements," *IEEE Transactions on Microwave Theory and Techniques*, vol. 64, no. 11, pp. 3864–3877, 2016.
- [36] L. Su, J. Naqui, J. Mata-Contreras, and F. Martín, "Splitter/combiner microstrip sections loaded with pairs of complementary split ring resonators (CSRRs): modeling and optimization for differential sensing applications," *IEEE Transactions on Microwave Theory and Techniques*, vol. 64, no. 12, pp. 4362–4370, December 2016.
- [37] J. Naqui and F. Martín, "Angular displacement and velocity sensors based on electric-LC (ELC) loaded microstrip lines," *IEEE Sensors Journal*, vol. 14, no. 4, pp. 939–940, 2014.
- [38] J. Naqui, J. Coromina, A. Karami-Horestani, C. Fumeaux, and F. Martín, "Angular displacement and velocity sensors based on coplanar waveguides (CPWs) loaded with S-shaped split ring resonators (S-SRR)," *Sensors*, vol. 15, no. 5, pp. 9628–9650, 2015.
- [39] M. S. Boybay and O. M. Ramahi, "Material characterization using complementary split-ring resonators," *IEEE Transactions on Instrumentation and Measurement*, vol. 61, no. 11, pp. 3039–3046, 2012.
- [40] C.-S. Lee and C.-L. Yang, "Complementary split-ring resonators for measuring dielectric constants and loss tangents," *IEEE Microwave and Wireless Components Letters*, vol. 24, no. 8, pp. 563–565, 2014.
- [41] A. Ebrahimi, W. Withayachumnankul, S. Al-Sarawi, and D. Abbott, "High-sensitivity metamaterial-inspired sensor for microfluidic dielectric characterization," *IEEE Sensors Journal*, vol. 14, no. 5, pp. 1345–1351, 2014.
- [42] C.-L. Yang, C.-S. Lee, K.-W. Chen, and K.-Z. Chen, "Noncontact measurement of complex permittivity and thickness by using planar resonators," *IEEE Transactions on Microwave Theory and Techniques*, vol. 64, no. 1, pp. 247–257, 2016.
- [43] J. Bonache, M. Gil, I. Gil, J. Garcia-Garcia, and F. Martín, "On the electrical characteristics of complementary metamaterial resonators," *IEEE Microwave and Wireless Components Letters*, vol. 16, no. 10, pp. 543–545, 2006.
- [44] A. Salim and S. Lim, "Complementary Split-Ring Resonator-Loaded Microfluidic Ethanol Chemical Sensor," *Sensors*, vol. 16, no. 12, pp. 1–13, 2016.

## Research Article

# A Broadband Left-Handed Metamaterial Microstrip Antenna with Double-Fractal Layers

**Roman Kubacki, Salim Lamari, Mirosław Czyżewski, and Dariusz Laskowski**

*Faculty of Electronics, Military University of Technology, Warsaw, Poland*

Correspondence should be addressed to Roman Kubacki; [roman.kubacki@wat.edu.pl](mailto:roman.kubacki@wat.edu.pl)

Received 18 January 2017; Revised 11 March 2017; Accepted 6 April 2017; Published 7 May 2017

Academic Editor: Ariel Epstein

Copyright © 2017 Roman Kubacki et al. This is an open access article distributed under the Creative Commons Attribution License, which permits unrestricted use, distribution, and reproduction in any medium, provided the original work is properly cited.

This paper proposes a microstrip patch antenna based on the left-handed metamaterial concept, using planar periodic geometry, which results in improved characteristics. This periodic geometry is derived from fractal shapes, which have been widely used in antenna engineering. The metamaterial property was obtained as a result of the double-fractal structure on both the upper and the bottom sides of the antenna. The final structure has been optimized to enhance bandwidth, gain, and radiation characteristics of the microstrip antenna. This combination significantly improved antenna performance; our design could support an ultrawide bandwidth ranging from 4.1 to 19.4 GHz, demonstrating higher gain with an average value of 6 dBi over the frequency range and a peak of 10.9 dBi and a radiation capability directed in the horizontal plane of the antenna.

## 1. Introduction

In commercial wireless communication systems, the antenna remains a key element of the communication chain. The efficiency of a radio broadcasting system is directly related to the characteristics of its antennas. In addition, future communication systems using cognitive radio or flexible radio will need smaller wideband antennas. In this paper, we focus on one of the common antenna designs—the microstrip patch antenna. This design has many advantages; it can be easily fabricated using a lithographic technique, it has a low profile, it has a low production cost, and its structure is fairly simple. However, these advantages are offset by the narrow bandwidth of the antenna. To date, several approaches have been proposed to address this deficiency. In most cases, the proposed solution was to increase the thickness and decrease the dielectric constant of the substrate at the same time. However, these attempts did not produce significant bandwidth enhancements in redesigned antennas.

Some specialised techniques were developed for bandwidth enhancement. One of such techniques involves the inclusion of additional resonators to the main patch. This can be done by inserting parasitic patch elements in a coplanar manner near the fed patch [1], or by stacking two

or more patches [2]. Another technique is to ensure good impedance matching between the feed and the radiator and thus reduce reflection loss [3, 4]. This technique resulted in bandwidth enhancement of at most 30%, but the aforementioned solutions require more space and thus invariably increase the size of the antenna. It is possible to obtain wideband characteristics while keeping the low profile of the patch antenna. To do so, one needs to cut “U” shaped slots in the patch, or two parallel slits in one of the radiating edges, creating a shaped patch [5]. We note that these methods have the advantage of enhancing the bandwidth without augmenting the size of the microstrip antenna, but the most noticeable wideband capability, about 47%, was obtained mainly using a design with foam and air substrates, which are not appropriate for arrays and would be challenging to integrate in microwave systems.

Taking into account the above-mentioned drawback of the antennas, the important task in microstrip antenna design is to create an antenna capable of supporting wideband or even ultrawideband (UWB) frequency range. With the development of new materials called left-handed materials (LHM), or left-handed metamaterials, it is possible to achieve a significantly wider frequency range. As a result, many

antennas with LHM structures with better performance than conventional microstrip patch antennas were proposed.

At present, there is no clear classification of metamaterial-based antennas due to the fact that the problem is still not mature. Nevertheless, according to [6], two categories can be distinguished. The first category is the concept of a transmission line composed of a periodic repetition of a unit cell comprising a series capacitance and a shunt inductance [7]. This category is a direct application of the leaky-wave metamaterial antennas, which consists of a cascaded series of unit cells lying on a matched microstrip line [8, 9]. This type is preferred for beam scanning applications. In the second category are the resonant antennas, which, in opposition to the first category, are obtained by terminating the structure to the free space by a short or open circuit [9]. The metamaterial-based resonant types of antenna structures allow dual-band, multiband behaviours and can be miniaturized but do not increase the bandwidth of the antenna.

However, even these LHM antennas cannot achieve a sufficiently wide frequency range. Many attempts have been proposed to widen the bandwidth of microstrip antenna using left-handed metamaterial structures. Among these, we can find a broadband planar antenna composed of a dipole and left-handed unit cells [10]. This configuration achieved a bandwidth of 1.2 GHz. Another model realized with  $2 \times 2$  mushroom structure combined with a notch on the surface, with the entire structure on a solid ground plane, was proposed in [11]. Reflective metasurfaces placed above an ordinary patch antenna can be used to enhance the gain and reduce the size of the structure, using [12]  $4 \times 4$  unit cells of reflective metasurfaces consisting of double closed rings suspended above a microstrip patch antenna. However, even this configuration achieved only 13% of bandwidth. A LHM antenna using a meander line is proposed in [11] where a single unit cell is incorporated with an interdigitated capacitor for the series capacitance, while the shunt inductance is produced by the meandered ground plane extension connected to the antenna by a via through the substrate. Still, most of the left-handed metamaterial-based antennas presented above are not wideband and have low gain and are thus unable to cover more than one wireless communication standard or claim to integrate high data rate transmission systems.

Planar left-handed metamaterial structures were proposed a few years ago [13]. The discussed structures consist of 2D periodic arrays of unit cells. This concept was applied to LHM antennas, resulting in broadband and high gain designs. The periodic patterns which showed left-handed characteristics were applied to rectangular conventional microstrip patch antennas. These configurations allowed obtaining a frequency range several times wider than the same patch antenna without the metamaterial pattern.

A perspective approach was proposed in [14] where a left-handed metamaterial antenna can achieve a broad bandwidth. This structure is a microstrip line loaded with different patterns on the metal parts of the substrate. On the top patch, the periodic gaps are designed in the form of isolated microtriangles, while, on the bottom ground plane, periodically distributed cross-strip gaps are designed.

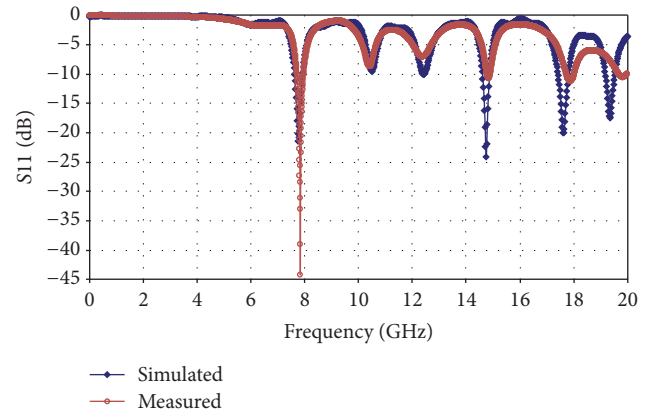


FIGURE 1: Results of the simulated and measured S11 values of the conventional microstrip antenna.

The structure achieves a significantly broader bandwidth of 3.2 GHz.

The main motivation of this work was to design an antenna with the widest possible bandwidth. This is why an ultrawideband microstrip antenna is presented. The concept of planar 2D left-handed metamaterial structure with periodic patterns is applied in order to enhance the bandwidth of a conventional microstrip patch antenna. The periodic patterns are formed by the repetition of a square unit cell along two axes. In fact, square unit cells, formed by the top and bottom layers of the dielectric substrate, consist of 2 different patterns on both layers. These patterns are inspired by fractal geometry, and their use is motivated by the benefits of fractals in antenna engineering [15–17].

Fractal based antennas are already presented in the literature, featuring patches with fractal structures. However, our proposed antenna geometry is novel due to its double-fractal layer design. Both layers of the antenna have fractal forms, but each patch includes different shapes. The upper side of the antenna follows the shape of crossbar fractals, with Minkowski fractals on the lower layer. The proposed self-similarity and ease of repetitiveness of the geometry make these designs attractive for creating a periodic structure.

The conventional microstrip patch antenna, which was used as a benchmark for comparison, produced a very limited bandwidth of 225 MHz. After introducing the planar metamaterial concept combined with double-fractal layers geometry, its bandwidth was multiplied by 68, to more than 15 GHz.

## 2. The Conventional Reference Antenna

A rectangular microstrip patch antenna was designed to serve as a reference. The patch is  $12 \times 16 \text{ mm}^2$ , and the feeding line is  $2.46 \times 8 \text{ mm}^2$ . The simulated and measured S11 values of the conventional reference antenna are presented in Figure 1.

## 3. The Double-Fractal Layers Antenna Design

The proposed metamaterial structure is in two-dimensional configuration. It is represented by a square unit cell of

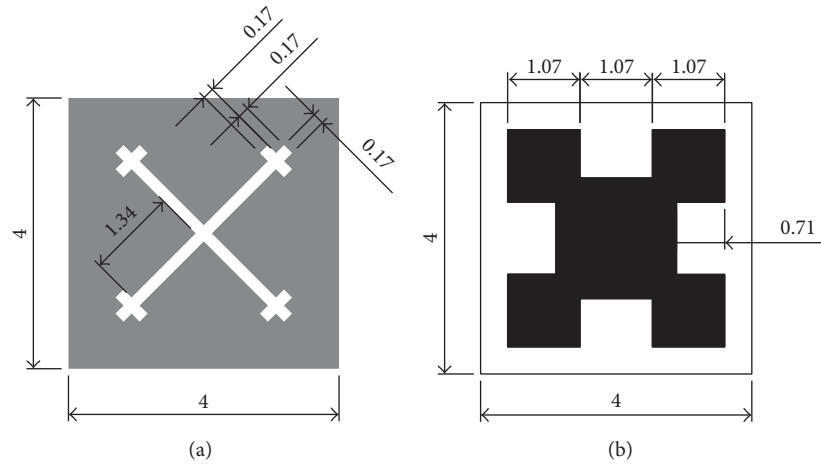


FIGURE 2: The fractal based elementary unit cells: (a) crossbar fractal for the top of the antenna, (b) Minkowski fractal for the bottom of the antenna (dimensions are in mm).

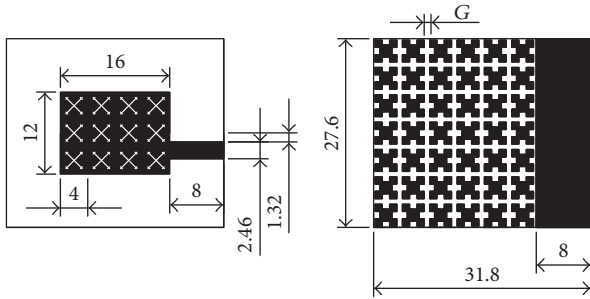


FIGURE 3: The proposed double-fractal antenna geometry.

$4 \times 4 \text{ mm}^2$ . The unit cell is composed of two planar metallic layers sandwiching a dielectric substrate. The two metallic layers were etched with two distinct fractal shapes. The crossbar fractal [18] diagonally lying on the square unit cell was etched out on the top. On the bottom, the Minkowski fractal [19, 20] in its first iteration was etched.

Constituent unit cells are depicted in Figure 2, while the view of double-fractal antenna geometry is presented in Figure 3. The entire structure of the proposed antenna measures  $27.6 \times 31.8 \text{ mm}^2$ , with the same dimension for the feeding line (Figure 3). The antenna was designed with the Rogers RT 5880 low-loss substrate ( $\tan \delta = 0.0009$  at 10 GHz) with dielectric constant of 2.2 and thickness of 0.79 mm. The upper patch consists of the  $4 \times 3$  square unit cells with the diagonal crossbar fractal shape having the edge of 4 mm in a periodic arrangement (Figures 3 and 4). On the ground plane, composed of metallic patches separated by slot gaps, the Minkowski island fractals of  $6 \times 7$  square unit cells are placed also in a periodic arrangement. This configuration improves the coupling between the patch and the ground plane by forming a capacitive-inductive (C-L) equivalent circuit which provokes the left-handed property. The view of the top and bottom sides of the antenna is presented in Figure 4.



FIGURE 4: Picture of the fabricated antenna.

#### 4. Results and Discussion

A parametric study was created to analyse the influence of the geometry on the performance of the antenna. In it, a variation in dimensions by the suitable increment, of one parameter at a time in the antenna geometry, is performed. The values of the dimensions giving the best performances of return loss (S11) will be obtained separately. These values are then combined together in order to obtain the optimal configuration of the antenna giving the best S11 performance and thus the largest bandwidth. We noticed that the width  $G$  of the gap between the cells on the ground plane (Figure 3) has a significant effect on the S11 value. Four dimensions of  $G$  were investigated from 0.2 mm to 0.5 mm, in increments of 0.1 mm, and the resulting S11 values are presented in Figure 5.

From the plot, we noticed that when the width of the gap between the cells on the ground plane is the largest, which in our case is 0.5 mm, so is the bandwidth. However, for higher values of  $G$ , the functions of S11 get rapidly worse. For further investigation,  $G = 0.5 \text{ mm}$  has been taken into account. The antenna with the optimal parameters resulting in the widest bandwidth was obtained and then fabricated, as depicted in Figure 4, to empirically measure the proposed microstrip antenna design. The measured S11 value of this antenna, in function of frequency, is presented in Figure 6. The figure shows good correlation between measured and simulated values and the very wide bandwidth of the proposed configuration.

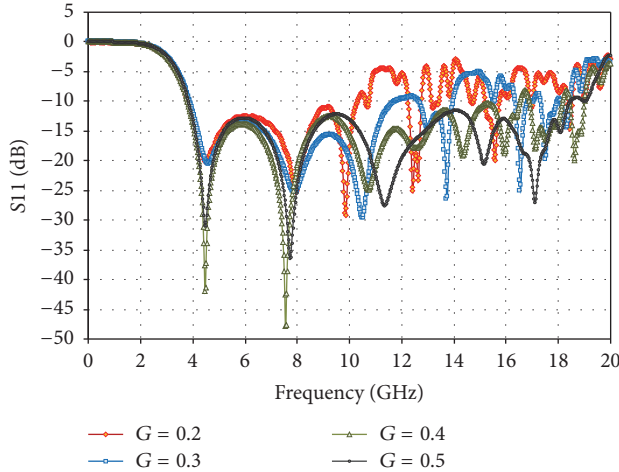


FIGURE 5: Results of simulation S11 with variation in the width of the gap between patches ( $G$  are in mm).

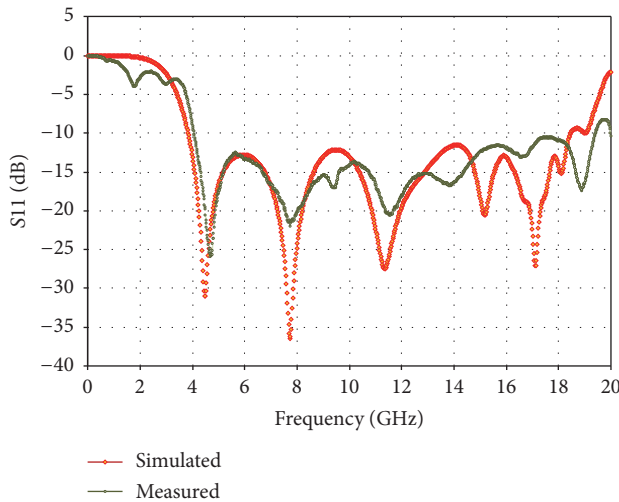


FIGURE 6: Results of measured and simulated values of S11 for the proposed antenna.

Figure 6 demonstrates the widened bandwidth of the proposed antenna, where the measured frequency range is even wider than the simulated one. It has achieved, at the level of  $-10$  dB, a bandwidth ranging from 4.1 GHz to 19.4 GHz, for a total bandwidth of 15.3 GHz, while in the conventional antenna the bandwidth was only 0.225 GHz.

## 5. Dispersion Characteristics

The possible feasibility of material characterized by simultaneously negative permittivity and permeability was discussed by Veselago [21]. Taking into account the fact that such materials do not exist in the nature, they are called metamaterials. In such materials, the wavevector is antiparallel to the Poynting vector and for this reason they are named “left-handed materials” or “backward wave media.”

In order to check that the designed antenna structure supports backward waves, the dispersion diagram was simulated

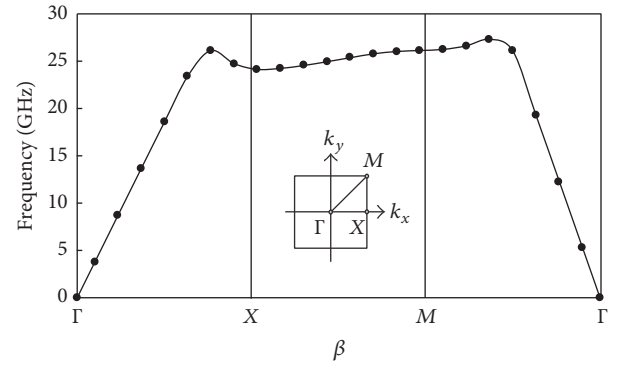


FIGURE 7: The dispersion diagram of the double-fractal based unit cells.

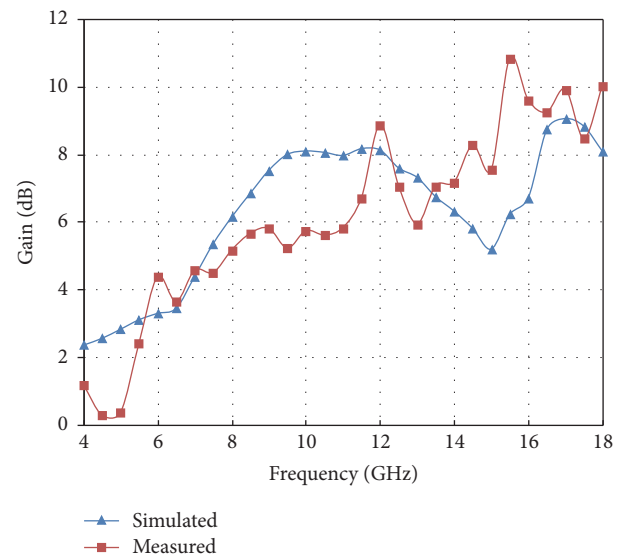


FIGURE 8: The simulated and measured gain of the proposed antenna.

by applying the periodic boundary conditions in the  $x$  and  $y$  directions of the unit cell. Figure 7 shows the dispersion characteristics of the unit cell along the paths between the high symmetry points  $\Gamma$ ,  $X$ , and  $M$  of the reduced Brillouin zone, which is plotted in the  $\omega$ - $\beta$  curve. In this curve, the slope of the straight line connecting the origin and a certain point on the  $\omega$ - $\beta$  curve represents the phase velocity  $V_p$ , and the slope of the line tangential to the curve at that point represents the group velocity  $V_G$  [21]. It can be noticed from Figure 8 that the slope representing  $V_G$  is negative, and hence the group velocity and phase velocity are in opposite directions, leading to the conclusion that the structure supports backward waves.

## 6. Antenna Gain and Characteristics

The gain of the proposed antenna was simulated and measured over the working bandwidth, from 4 GHz to 18 GHz, as illustrated in Figure 8. The fabricated antenna achieved an average gain of 6 dBi and a maximum value of 10.9 dBi. The efficiency improves with the growth of frequency. For

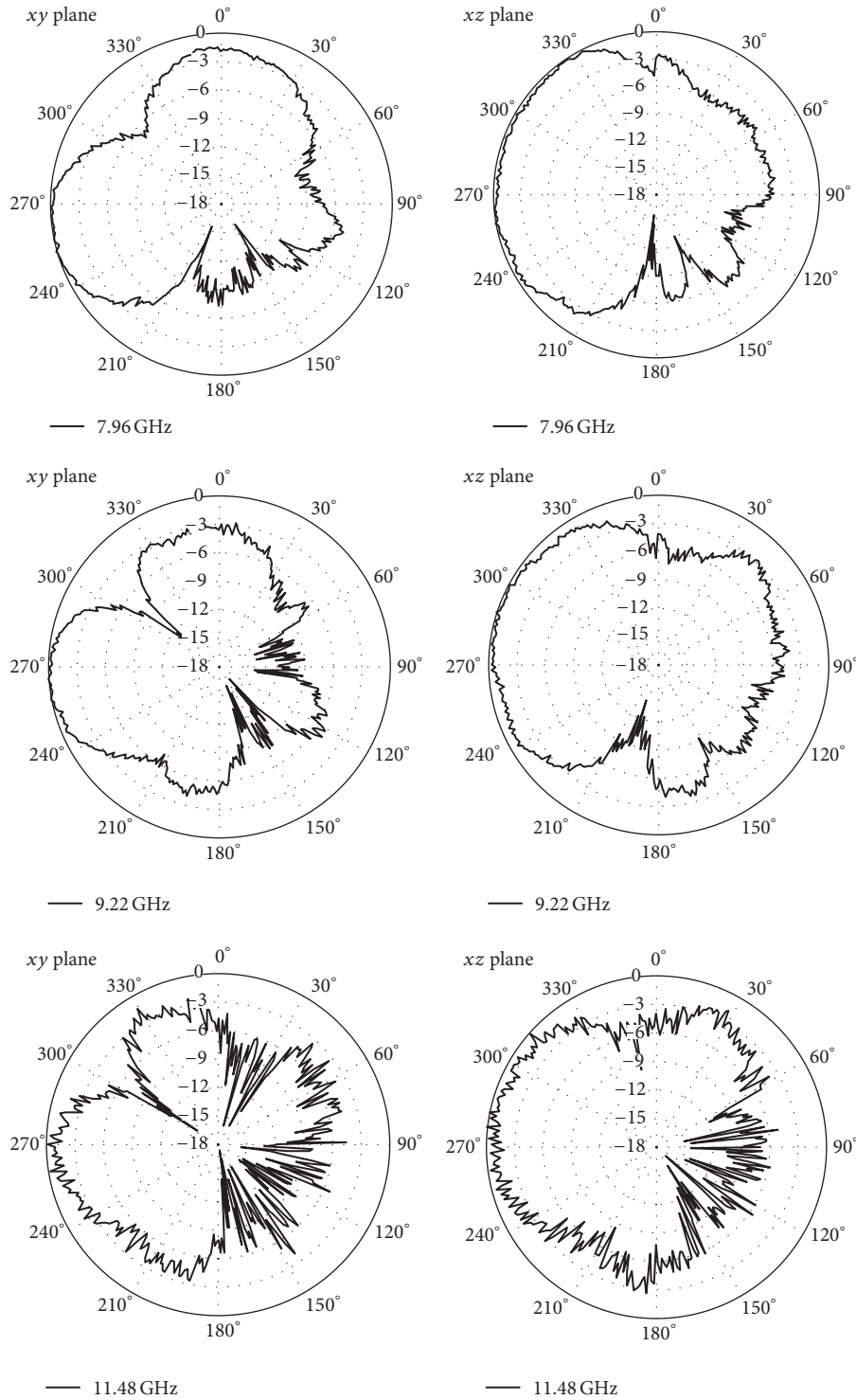


FIGURE 9: The radiation pattern of the proposed antenna at the following frequencies: 7.96 GHz, 9.22 GHz, and 11.48 GHz in the “xy” and “xz” planes.

frequencies mentioned in Figure 9, the following values of efficiency were obtained: of 86.4% at 7.96 GHz, of 88.3% at 9.22 GHz, and of 89.7% at 11.48 GHz.

The radiation characteristics for the proposed antenna are presented in Figure 9. Radiation patterns were measured in the following frequencies: 7.96 GHz, 9.22 GHz, and

11.48 GHz, in the characteristic planes “xy” and “xz.” It can be seen that left-handed properties of the antenna resulted in a radiation spread of 270°. It should also be noted that shapes of radiation characteristics change in function of frequency. A similar disadvantage was observed in cases presented in the literature describing microstrip antennas

with ultrabroadband properties. Future efforts should focus on obtaining similar shapes of radiation patterns in function of frequency to improve the efficiency of radio link.

## 7. Conclusion

In this paper, an ultrawideband antenna based on the planar periodic left-handed metamaterial concept was proposed. The metamaterial property was obtained through the use of a double-fractal structure on both the top and the bottom sides of the antenna. The proposed antenna achieved the frequency range of 4.1 GHz to 19.4 GHz, realizing a bandwidth of 15.3 GHz. Therefore, the bandwidth of the manufactured antenna is 68 times larger than the bandwidth of the conventional microstrip antenna.

The antenna radiates at a 270° angle and has an enhanced gain with an average value of almost 6 dBi and a peak of 10.9 dBi. The combination of the metamaterial planar concept and the fractal shapes seems to be a good method to enhance the characteristics of the microstrip patch antenna. This antenna can easily be used in a communication system, where such enhanced features are required.

## Conflicts of Interest

The authors declare that they have no conflicts of interest.

## Acknowledgments

This work was carried out with the financial support of the Polish National Centre for Research and Development as Project no. DOB-1-1/PS/2014.

## References

- [1] G. Kumar and K. C. Gupta, "Broadband microstrip antennas using additional resonators gap-coupled to the radiating edges," *IEEE Transactions on Antennas and Propagation*, vol. 32, no. 12, pp. 1375–1379, 1984.
- [2] U. K. Revankar and A. Kumar, "Experimental investigation of three-layer electromagnetically coupled circular microstrip antennas," *Electronics Letters*, vol. 27, no. 13, pp. 1187–1189, 1991.
- [3] H. F. Pues and A. R. van de Capelle, "Impedance-matching technique for increasing the bandwidth of microstrip antennas," *IEEE Transactions on Antennas and Propagation*, vol. 37, no. 11, pp. 1345–1354, 1989.
- [4] X.-D. Huang, X.-H. Jin, and C.-H. Cheng, "Novel impedance matching scheme for patch antennas," *Progress In Electromagnetics Research Letters*, vol. 14, pp. 155–163, 2010.
- [5] S. Weigand, G. H. Huff, K. H. Pan, and J. T. Bernhard, "Analysis and design of broad-band single-layer rectangular U-slot microstrip patch antennas," *IEEE Transactions on Antennas and Propagation*, vol. 51, no. 3, pp. 457–468, 2003.
- [6] L. Liu, C. Caloz, and T. Itoh, "Dominant mode leaky-wave antenna with backfire-to-endfire scanning capability," *Electronics Letters*, vol. 38, no. 23, pp. 1414–1416, 2002.
- [7] A. Sanada, C. Caloz, and T. Itoh, "Characteristics of the composite right/left-handed transmission lines," *IEEE Microwave and Wireless Components Letters*, vol. 14, no. 2, pp. 68–70, 2004.
- [8] A. I. Anghel and R. Căcoveanu, "Improved composite right/left-handed cell for leaky-wave antenna," *Progress In Electromagnetics Research Letters*, vol. 22, pp. 59–69, 2011.
- [9] C. Caloz, T. Itoh, and A. Rennings, "CRLH metamaterial leaky-wave and resonant antennas," *IEEE Antennas and Propagation Magazine*, vol. 50, no. 5, pp. 25–39, 2008.
- [10] M. Palandoken, A. Grede, and H. Henke, "Broadband microstrip antenna with left-handed metamaterials," *IEEE Transactions on Antennas and Propagation*, vol. 57, no. 2, pp. 331–338, 2009.
- [11] C. G. M. Ryan and G. V. Eleftheriades, "A wideband metamaterial meander-line antenna," in *Proceeding of the 6th European Conference on Antennas and Propagation (EuCAP '12)*, pp. 2329–2331, March 2012.
- [12] S. Chaimool, K. L. Chung, and P. Akkaraekthalin, "Bandwidth and gain enhancement of microstrip patch antennas using reflective metasurface," *IEICE Transactions on Communications*, vol. E93-B, no. 10, pp. 2496–2503, 2010.
- [13] N. Matsunaga, A. Sanada, and H. Kubo, "Novel two-dimensional planar negative refractive index structure," *IEICE Transactions on Electronics*, vol. 89, no. 9, pp. 1276–1282, 2006.
- [14] L.-W. Li, Y.-N. Li, T. S. Yeo, J. R. Mosig, and O. J. F. Martin, "A broadband and high-gain metamaterial microstrip antenna," *Applied Physics Letters*, vol. 96, no. 16, pp. 164101–164103, 2010.
- [15] W. J. Krzysztofik, "Fractal geometry in electromagnetics applications from antenna to metamaterials," *Microwave Review*, vol. 19, no. 2, pp. 3–14, 2013.
- [16] J. P. Gianvittorio and Y. Rahmat-Samii, "Fractal antennas: a novel antenna miniaturization technique, and applications," *IEEE Antennas and Propagation Magazine*, vol. 44, no. 1, pp. 20–36, 2002.
- [17] D. H. Werner, R. L. Haupt, and P. L. Werner, "Fractal antenna engineering: the theory and design of fractal antenna arrays," *IEEE Antennas and Propagation Magazine*, vol. 41, no. 5, pp. 37–59, 1999.
- [18] D. H. Werner and S. Ganguly, "An overview of fractal antenna engineering research," *IEEE Antennas and Propagation Magazine*, vol. 45, no. 1, pp. 38–57, 2003.
- [19] L. B. Moraes and S. E. Barbin, "A comparison between Minkowski and Koch fractal patch antennas," in *Proceeding of the SBMO/IEEE MTT-S International Microwave and Optoelectronics Conference (IMOC '11)*, pp. 17–21, November 2011.
- [20] L. Xiao Zheng, X. Xiang Ming, L. Sheng Li, and X. Zhang, "Analysis of the patch antenna based on the minkowski fractal," in *Proceeding of the 4th International Conference on Microwave and Millimeter Wave Technology (ICMMT '04)*, 2004.
- [21] V. Veselago, "The electrodynamics of substances with simultaneously negative values of  $\epsilon$  and  $\mu$ ," *Soviet Physics Uspekhi*, vol. 10, no. 4, 1968.

## Research Article

# CRLH Transmission Lines for Telecommunications: Fast and Effective Modeling

**Juanjuan Gao and Guizhen Lu**

*School of Information Engineering, Communication University of China, Beijing 100024, China*

Correspondence should be addressed to Juanjuan Gao; [gaojj\\_1989@126.com](mailto:gaojj_1989@126.com)

Received 19 August 2016; Revised 21 November 2016; Accepted 15 December 2016; Published 4 January 2017

Academic Editor: Davide Ramaccia

Copyright © 2017 J. Gao and G. Lu. This is an open access article distributed under the Creative Commons Attribution License, which permits unrestricted use, distribution, and reproduction in any medium, provided the original work is properly cited.

A different parameter extraction approach based on zero immittances for composite right/left-handed (CRLH) structure is presented. For lossless unit cell equivalent circuit model, LC parameters of series and parallel branches are extracted according to series resonance frequency and parallel resonance frequency, respectively. This approach can be applied to symmetric and unbalanced CRLH structures. The parameter extraction procedure is provided and validated by T-type unit cell model. The responses of distributed prototype and extracted equivalent LC circuit model are in good agreement. The equivalent circuit modeling can improve the degree of freedom in the CRLH TLs design. This parameter extraction method provides an effective and straightforward way in CRLH metamaterials design and applications in telecommunication systems.

## 1. Introduction

In telecommunication system, the role of the oscillator is to establish stable harmonic oscillation at a specific carrier frequency for modulation and mixing, which is shown in Figure 1(a). In the oscillator circuit, the main function of resonator is frequency selection and storage of energy. Conventional transmission line resonator is size dependent on frequency, which is not suitable for use in miniaturized integrated circuits. Composite right/left-handed transmission line (CRLH TL), introduced by Caloz and Itoh, is the transmission line (TL) approach of left-handed materials (LHMs) [1]. CRLH metamaterials with right-handed (RH) and left-handed (LH) properties have the advantages of low loss and wide bandwidth, which have been extensively studied and broad applied in guided-wave and radiated-wave devices for over decades [2–5]. Typically, the distributed CRLH TL is consisting of the series interdigital capacitor (IDC) and the shunt shorted stub inductor (SSI), which can be realized by the microstrip line and coplanar waveguide [4]. Based on CRLH TL structures zeroth-order resonator can be achieved; its size is frequency independent and can be realized, theoretically, arbitrarily small [6]. The schematic diagram of oscillator circuit using a zeroth-order resonator

is shown in Figure 1(b). Using the zeroth-order resonator can effectively reduce the size of the oscillator circuit and improve the miniaturization of communication systems.

To accurately design CRLH TL and investigate the characteristics of CRLH TL-based devices, the equivalent circuit model is used to parameterize the complicated behaviors of the practical distributed circuits [7, 8]. The characteristics of the CRLH TLs are closely related to the LC parameters. Accurate design depends on whether the parameters meet the requirements. The design can be modified by parameter extraction in order to achieve optimum performances. In [9], to calculate the extracted LC parameters, the equivalent T and  $\Pi$  networks of IDC and SSI are separately characterized by admittance and impedance matrices; however coupling effects between IDC and SSI are not taken into account in this parameter extraction procedure. Otto et al. proposed an energy based method to extract equivalent circuit parameters [10], which was further implemented in [11]. However, this method requires the use of software for electromagnetic energy calculation, cannot be extracted by experiment. Based on effective medium concept, revised Nicolson-Ross-Weir (NRW) approach was applied to extract equivalent parameters. In this method, the equivalent circuit model parameters are deduced by the effective permittivity  $\epsilon_r$  and the effective

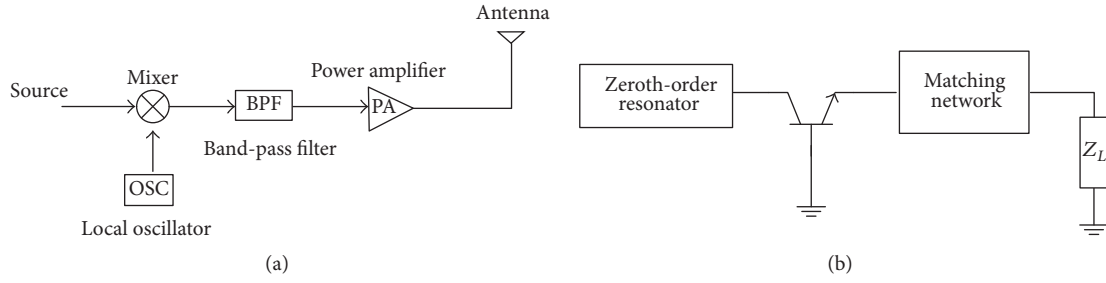


FIGURE 1: (a) The block diagram of telecommunication system. (b) The block diagram of oscillator.



FIGURE 2: CRLH TL structures. (a) Periodic CRLH TLs with series capacitors and shunt stub inductors. (b) Geometry of unit cell of CRLH TL.

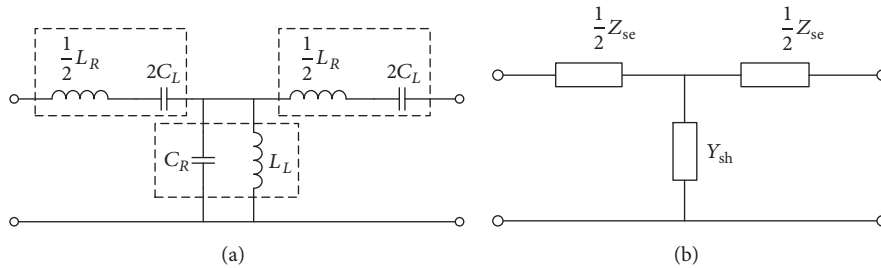


FIGURE 3: Equivalent circuit models of CRLH TL for parameters extraction. (a) T-type unit cell circuit model. (b) Equivalent network.

permeability  $\mu_r$ . However, this method suffers multisolutions problem [12–15]. The equivalent circuit extraction method proposed in [16] employs the transmission-line-reflect (TLR) calibration to deembed the effects of the transmission lines. In this method both full-wave simulation and measured S-parameters are used to obtain the  $ABCD$  transmission matrix of the CRLH unit cell.

In this paper, a different parameter extraction approach based on zero immittances has been presented. For lossless equivalent LC circuit model adopted, series resonance frequency and parallel resonance frequency are obtained from immittances characteristic, which is utilized to extract the LC parameters. In the proposed method, test transmission lines are placed in both sides of the CRLH structure. The effects of the transmission lines are eliminated by matrix calculation. The scattering parameter used can be obtained by full-wave simulations. The extraction procedure is convenient and effective and can be applied in unbalanced CRLH structures. This approach is illustrated by T-type unit cell

model. The transmission characteristics of the distributed CRLH structure and the extraction LC equivalent circuit are in comparison with each other, and in wider bandwidth the extracted equivalent LC circuit model is effective.

## 2. Equivalent Circuit Modeling and Parameter Extraction Approach

The CRLH TL considered in this paper is constituted by series interdigital capacitor and parallel shorted stub inductors, which is shown in Figure 2(a). The dimensions are the same as those in [1], which is depicted in Figure 2(b). Assuming the transmission line is lossless, interdigital capacitor is modeled with  $C_L$  series  $L_R$  and stub inductor is modeled with  $L_C$  shunt  $C_R$ . The T-type unit cell circuit model of CRLH TLs is shown in Figure 3(a) and the corresponding microwave network is displayed in Figure 3(b).

Due to the unit cell circuit model shown in Figure 3, the immittances  $Z_{se}$  and  $Y_{sh}$  characteristics are plotted in

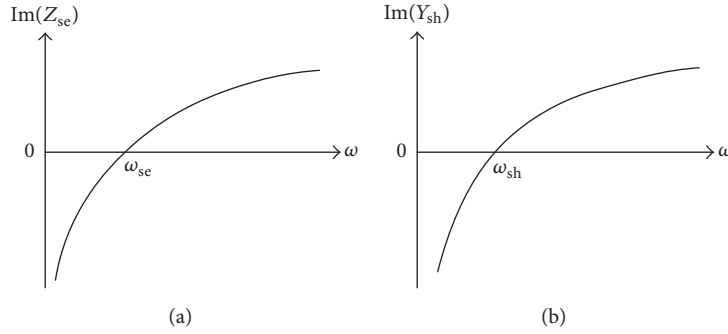


FIGURE 4: Immittances characteristics of T-type equivalent circuit model. (a) Series impedance  $Z_{se}$  characteristic curve. (b) Shunt admittance  $Y_{sh}$  characteristic curve.

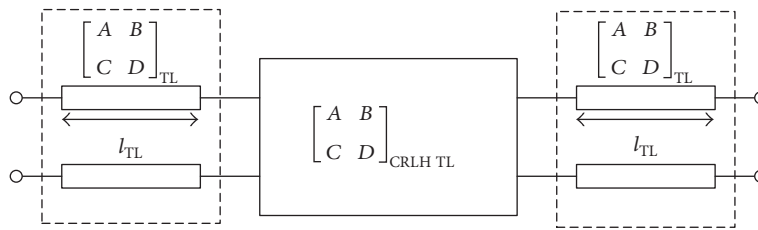


FIGURE 5: Parameter extraction circuit system model.

Figure 4. When we have zero immittances, the series resonance frequency  $\omega_{se}$  and parallel resonance frequency  $\omega_{sh}$  are obtained.

$$\omega_{se} = \omega|_{\text{Im}(Z_{se})=0} = \frac{1}{\sqrt{L_R C_L}}, \quad (1)$$

$$\omega_{sh} = \omega|_{\text{Im}(Y_{sh})=0} = \frac{1}{\sqrt{L_C C_R}}.$$

Based on the characteristics of immittances  $Z_{se}$  and  $Y_{sh}$ , we introduce an extraction approach to yield simple expressions for  $C_L$ ,  $L_R$ ,  $L_C$ , and  $C_R$ . For a two-port network, depicted in Figure 2(b),  $Z_{se}$  and  $Y_{sh}$  can be described in terms of  $ABCD$  transmission matrix. Using standard network conversion formulas, the series impedance and parallel admittance can be written in terms of the  $ABCD$  parameters, which lead to

$$Z_{se}^{\text{sym}} = \frac{2(A-1)}{C}, \quad (2)$$

$$Y_{sh}^{\text{sym}} = C.$$

With zero immittances  $Z_{se}$  and  $Y_{sh}$ , the series resonance frequency and the parallel resonance frequency are determined by

$$\text{Im}(Z_{se})|_{\omega_{se}} = 0, \quad (3)$$

$$\text{Im}(Y_{sh})|_{\omega_{sh}} = 0.$$

With  $\omega_{se}$  and  $\omega_{sh}$ , the LC parameters of series and parallel tank would be solved separately. And the corresponding extract parameters are determined by

$$L_R = \frac{1}{2} \frac{\partial}{\partial \omega} \text{Im}(Z_{se})|_{\omega_{se}},$$

$$C_L = \frac{1}{\omega_{se}^2 L_{se}}, \quad (4)$$

$$C_R = \frac{1}{2} \frac{\partial}{\partial \omega} \text{Im}(Y_{sh})|_{\omega_{sh}},$$

$$L_L = \frac{1}{\omega_{sh}^2 L_{sh}}.$$

When  $\omega_{se} = \omega_{sh}$ , called balanced case, CRLH TLs would exhibit special properties. In practice, most initial fabrics are unbalanced, and with this extraction approach we can conveniently revise the design. That is, this extraction procedure is applicable for both balanced and unbalanced cases.

### 3. Extraction Procedure and Validation

This section provides the extraction procedure based on circuit model shown in Figure 3 and verifies this method with CRLH TLs proposed by Caloz and Itoh. Usually, in order to obtain the transmission matrix of CRLH TL, a section of microstrip transmission line (TL) has to be added at each end of the component in full-wave simulation; the diagram is shown in Figure 5. However, the added microstrip TLs would change the original network characteristics such as

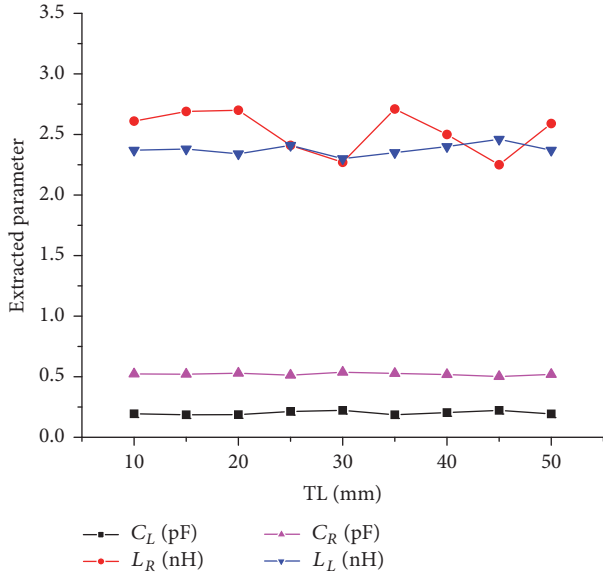


FIGURE 6: Extracted LC parameters of equivalent LC circuit model.

propagation phase. Therefore it is essential to eliminate the effect due to the test TLs.

The distributed CRLH TL and extracted equivalent circuit model are validated by comparing the scattering characteristics. The procedure is provided as follows:

- (1) Do full-wave simulation for the distributed circuit of Figure 5 and test microstrip TL to get the S-parameters of overall circuit and TLs, respectively.
- (2) Compute  $[ABCD]$  of overall circuit and  $[ABCD]$  of TL corresponding to the S-parameters obtained in (1) using standard network conversion formulas.
- (3) Compute  $[ABCD]$  of CRLH TL using

$$\begin{aligned} [ABCD]_{\text{overall}} \\ = [ABCD]_{\text{TL}} [ABCD]_{\text{CRLH TL}} [ABCD]_{\text{TL}}. \end{aligned} \quad (5)$$

- (4) Compute the  $Z_{\text{se}}$  and  $Y_{\text{sh}}$  vector using again standard network conversion formulas.
- (5) Find zero points of  $Z_{\text{se}}$  and  $Y_{\text{sh}}$  using interpolation method to determine series resonance frequency  $\omega_{\text{se}}$  and parallel resonance frequency  $\omega_{\text{sh}}$ .
- (6) Compute the  $C_L$ ,  $L_R$ ,  $L_C$ , and  $C_R$  using (4).
- (7) With extraction parameters obtained from (6), simulate the equivalent LC circuit model and compare with distributed CRLH TL.

The CRLH TLs proposed by Caloz and Itoh and shown in Figure 1 is considered here to illustrate the parameter extraction procedure with T-type unit cell circuit model. Full-wave simulation and numerical calculation are developed; the extraction results are presented in Figure 6. With different test TL lengths, the extracted LC parameters are mainly stable. It should be noted that, since the test transmission

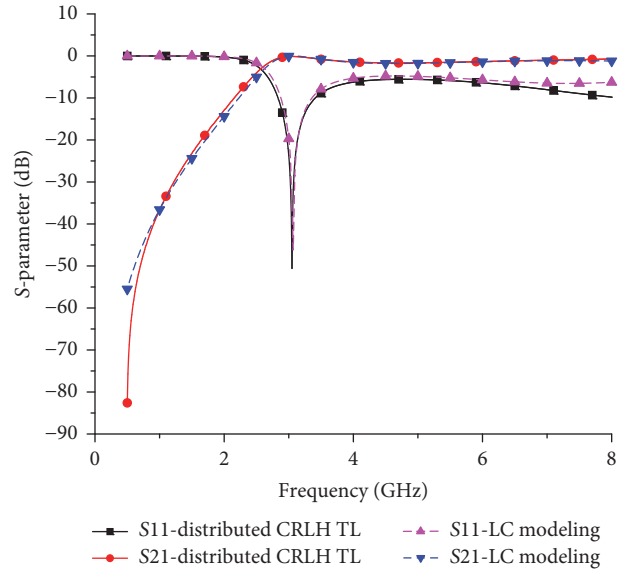


FIGURE 7: Comparison of S-parameters between distributed 1-cell CRLH TL and equivalent LC circuit model.

lines are series with the interdigital capacitor, the different transmission line length has a great influence on the  $L_R$  parameter. In the process of parameter extraction, the  $L_R$  value can be obtained by multiple extractions and averaging.

The set parameters  $L_R = 2.56$  nH,  $C_L = 0.192$  pF,  $C_R = 0.523$  pF, and  $L_L = 2.33$  nH of T-type unit cell circuit with TL = 20 mm has been selected for comparison with practical distributed structure. In Figure 7, S-parameters of distributed 1-cell CRLH TL structure and equivalent LC circuit model are presented. As shown in comparison results, within wider bandwidth, they are in good agreement with each other.

The CRLH TL is balanced when the series and shunt resonant frequencies are equal; on the contrary, the CRLH TL is unbalanced when the series and shunt resonant frequencies are different. It is noted that the series and parallel LCs are extracted from  $\omega_{\text{se}}$  and  $\omega_{\text{sh}}$ , respectively. Regardless of whether the series resonant frequency and the parallel resonant frequency are equal, this extraction method can model the CRLH TLs. This makes it convenient to apply this approach in both balanced and unbalanced CRLH structures.

## 4. Conclusion

A zero immittances based parameter extraction approach for distributed CRLH structures has been proposed, which is applicable to symmetric unit cells. According to series resonance frequency  $\omega_{\text{se}}$  and parallel resonance frequency  $\omega_{\text{sh}}$ , determined by immittances characteristics, LCs of series branch and parallel branch are extracted, respectively, and therefore this method can be used in unbalanced CRLH structures. The presented extraction procedure provides an effective and straightforward way in CRLH metamaterials design and application of telecommunication system. Finally, the authors are currently applying this approach in analysis of CRLH metamaterials-based microwave circuit.

## Competing Interests

The authors declare that there are no competing interests regarding the publication of this paper.

## References

- [1] C. Caloz and T. Itoh, "Novel microwave devices and structures based on the transmission line approach of metamaterials," in *Proceedings of the IEEE MTT-S International Microwave Symposium Digest*, vol. 1, pp. 195–198, Philadelphia, Pa, USA, June 2003.
- [2] A. Lai, C. Caloz, and T. Itoh, "Composite right/left-handed transmission line metamaterials," *IEEE Microwave Magazine*, vol. 5, no. 3, pp. 34–50, 2004.
- [3] J. Sorocki, I. Piekarczyk, K. Wincza, and S. Gruszczynski, "Right/left-handed transmission lines based on coupled transmission line sections and their application towards bandpass filters," *IEEE Transactions on Microwave Theory and Techniques*, vol. 63, no. 2, pp. 384–396, 2015.
- [4] C. Caloz, A. Sanada, and T. Itoh, "A novel composite right/left-handed coupled-line directional coupler with arbitrary coupling level and broad bandwidth," *IEEE Transactions on Microwave Theory and Techniques*, vol. 52, no. 3, pp. 980–992, 2004.
- [5] J.-G. Lee and J.-H. Lee, "Zeroth order resonance loop antenna," *IEEE Transactions on Antennas and Propagation*, vol. 55, no. 3, pp. 994–997, 2007.
- [6] A. Sanada, C. Caloz, and T. Itoh, "Zeroth-order resonance in composite right/left handed transmission line resonators," in *Proceedings of the Asia-Pacific Microwave Conference (APMC '03)*, pp. 1588–1592, Seoul, Republic of Korea, 2003.
- [7] F. Aznar, M. Gil, J. Bonache et al., "Characterization of miniaturized metamaterial resonators coupled to planar transmission lines through parameter extraction," *Journal of Applied Physics*, vol. 104, no. 11, Article ID 114501, 2008.
- [8] S.-G. Mao, S.-L. Chen, and C.-W. Huang, "Effective electromagnetic parameters of novel distributed left-handed microstrip lines," *IEEE Transactions on Microwave Theory and Techniques*, vol. 53, no. 4, pp. 1515–1521, 2005.
- [9] C. Caloz and T. Itoh, "Transmission line approach of left-handed (LH) materials and microstrip implementation of an artificial LH transmission line," *IEEE Transactions on Antennas and Propagation*, vol. 52, no. 5, pp. 1159–1166, 2004.
- [10] S. Otto, A. Rennings, T. Liebig, C. Caloz, and K. Solbach, "An energy-based circuit parameter extraction method for CRLH leaky wave antennas," in *Proceedings of the 4th European Conference on Antennas and Propagation (EuCAP '10)*, pp. 1–5, Barcelona, Spain, April 2010.
- [11] S. Otto, A. Rennings, K. Solbach, and C. Caloz, "Transmission line modeling and asymptotic formulas for periodic leaky-wave antennas scanning through broadside," *IEEE Transactions on Antennas and Propagation*, vol. 59, no. 10, pp. 3695–3709, 2011.
- [12] S.-G. Mao, M.-S. Wu, Y.-Z. Chueh, and C. H. Chen, "Modeling of symmetric composite right/left-handed coplanar waveguides with applications to compact bandpass filters," *IEEE Transactions on Microwave Theory and Techniques*, vol. 53, no. 11, pp. 3460–3466, 2005.
- [13] P. Chen, J. Ding, and X. Zheng, "Modeling of asymmetric and unbalanced composite right/left-handed transmission line," in *2011 IEEE International Conference on Signal Processing, Communications and Computing, ICSPCC 2011*, chn, September 2011.
- [14] V. Milosevic, B. Jokanovic, and R. Bojanic, "Effective electromagnetic parameters of metamaterial transmission line loaded with asymmetric unit cells," *IEEE Transactions on Microwave Theory and Techniques*, vol. 61, no. 8, pp. 2761–2772, 2013.
- [15] F. J. Hsieh and W. C. Wang, "Full extraction methods to retrieve effective refractive index and parameters of a bianisotropic metamaterial based on material dispersion models," *Journal of Applied Physics*, vol. 112, no. 6, 2012.
- [16] T. Liebig, A. Rennings, S. Held, and D. Erni, "Accurate parameter extraction of lossy composite right/left-handed (CRLH) transmission lines for planar antenna applications," in *Proceedings of the 4th International Congress on Advanced Electromagnetic Materials in Microwaves and Optics, Metamaterials*, September 2010.